

https://dspace.org/

Searching for multi-messenger counterparts to the sources in the H.E.S.S. Galactic Plane Survey

Batzofin, Rowan

2023
https://hdl.handle.net/10539/36948

Downloaded from a DSpace repository. https://dspace.org/

"Searching for multi-messenger counterparts to the sources in the H.E.S.S. Galactic Plane Survey"



WITS
UNIVERSITY

Rowan Batzofin
Supervised by Professor Nukri Komin

School of Physics
University of the Witwatersrand
Johannesburg, South Africa

A dissertation submitted to the Faculty of Science, University of the Witwatersrand, in fulfilment of the requirements for the degree of Master of Science

Johannesburg, 2022

Declaration

I declare that this dissertation is my own, unaided work. It is being submitted for the Degree of Master of Science at the University of the Witwatersrand, Johannesburg. It has not been submitted before for any degree or examination at any other University.



(signature of candidate)

27th day of June 2022 at 27A Gerard St, Observatory, Johannesburg

"Searching for multi-messenger counterparts to the sources in the H.E.S.S. Galactic Plane Survey"

Rowan Batzofin

Submitted for the degree Master of Science
2022

Abstract

The High Energy Stereoscopic System (H.E.S.S.) Galactic Plane Survey (HGPS) has detected very-high-energy (VHE) gamma-ray emission from 78 sources in the Milky Way. These sources belong to different object classes (pulsar wind nebulae, supernova remnants or binary systems) and some of these sources remain unidentified. The gamma-ray emission of these objects may be of leptonic or hadronic origin and gamma-ray observations alone cannot distinguish between these two scenarios. The detection of neutrino emission would provide evidence for a hadronic scenario and fitting a combined synchrotron and inverse Compton model would provide evidence of a leptonic scenario in these objects.

MeerKAT surveyed the 1st and 4th quadrant of the Milky Way. There are 8 unidentified H.E.S.S. sources in the regions surveyed by MeerKAT. This process of searching for radio emission coincident with the unidentified sources in the HGPS can be expanded to the whole Galactic Plane once MeerKAT has surveyed it all. One unknown and two known H.E.S.S. sources (HESS J1843-033, HESS J1826-148 and HESS J1833-105) are modelled with a combined synchrotron and inverse Compton model using the MeerKAT radio data and H.E.S.S. VHE data. HESS J1843-033 is an unidentified source, HESS J1826-148 is a binary and HESS J1833-105 is a composite SNR. That these sources could be fit by a combined synchrotron and inverse Compton model suggest that they are leptonic in nature.

Based on the observed gamma-ray spectra we predict the neutrino emission of all the sources in the HGPS under the hypothesis that the emission is solely of hadronic origin. This prediction relies entirely on observation and is independent of the source class, the distance or the ambient target material. These predictions are used to create an empirical model for the neutrino emission of the Milky Way. This model can be used to search for neutrino emission from individual gamma-ray sources as well as testing for neutrino emission from potential source populations in the Milky Way. This model was then compared to the possible neutrino sources detected by ANTARES where 56 of the possible neutrinos were associated with the predicted neutrino emission but there is no significant correlation to the ANTARES neutrino candidates and the predicted neutrino emissions.

Acknowledgements

I would like to thank my supervisor Professor Nukri Komin for all his help and guidance, I could not have completed my MSc without him. Despite the extra difficulties caused by the Covid19 pandemic he assisted me in many ways, from learning new skills to preparing for a conference and writing my dissertation.

I'd like to thank the local crew at H.E.S.S. site: Albert, Volker and Frikkie for their support while I was on shift. I had a great time and was treated like family. I'd also like to thank Ozi for his help while I was on shift and his continued assistance since then.

I'd like to thank SA-Gamma for funding my attendance at ICRC2021 and for funding my daily allowance while I was on shift at H.E.S.S. site and the support they provided in getting me home. I am also grateful to have been part of the H.E.S.S. collaboration and for the support I received from them while on shift.

I'd like to thank Professor Deena Naidoo for his concern with my being trapped in Namibia and for his assitance in getting me home.

I'd like to acknowledge all the places that collected the data that I used. The H.E.S.S. collaboration for the use of the the public data from the HGPS. The MeerKAT collaboration for the use of the MeerGAL data. The ANTARES Collaboration for the public data set of ANTARES neutrino point source candidates.

Contents

Declaration i
Abstract ii
Acknowledgements iv

1 Introduction **1**
1.1 Why study gamma rays 1
1.2 Problem under investigation 1
1.3 Aim 2
1.4 Hypotheses and questions 2
1.5 H.E.S.S. 2
1.6 H.E.S.S. Galactic Plane Survey 3
1.7 Neutrino telescopes 3
1.7.1 ANTARES 3
1.7.2 Future neutrino detectors 4
1.8 MeerKAT 5
1.9 Fermi 6
1.10 Mechanisms of gamma-ray emission 6
1.11 Modelling gamma-ray emission 7

2 Searching for the unidentified H.E.S.S. sources in the MeerKAT Galactic plane survey **9**
2.1 Unidentified Sources 9
2.2 Measuring MeerKAT Flux for H.E.S.S. Sources 10
2.3 Modelling the leptonic emission 12
2.4 HESS J1828-099 12
2.5 HESS J1832-085 15
2.6 HESS J1858+020 16
2.7 HESS J1457-593 17
2.8 HESS J1503-582 18
2.9 HESS J1702-420 19
2.10 HESS J1708-410 20
2.11 HESS J1729-345 21
2.12 HESS J1843-033 22
2.13 HESS J1844-030 24
2.14 Combined synchrotron and inverse Compton model for other sources 27
2.15 Discussion 29

3 Neutrino prediction **32**
3.1 Introduction 32
3.2 Method 32
3.2.1 Neutrino flux 32
3.2.2 Creating the map 34
3.3 ANTARES neutrino point sources 45
3.4 Discussion 51
3.5 Conclusion 51

4 Conclusion **54**

Appendices **60**

A Sampler fits **61**

B Kelner model python code **95**

List of Figures

2.1 MeerKAT image of the region of HESS J1828-099 with overlaid H.E.S.S. position contours (68% and 95%) and positions of X-ray and 2MASS sources. 13
2.2 Optical image (DSS) of the region of HESS J1828-099 with overlaid H.E.S.S. position contours (68% and 95%) and positions of X-ray and 2MASS sources. The red circle is the postion of the bright radio point source. 14
2.3 MeerKAT image of the region of HESS J1832-085 with overlaid H.E.S.S. position contours (68% and 95%) and overlaid SNR G23.11+0.18 15
2.4 MeerKAT image of the region of HESS J1858+020 with overlaid with SNR G35.6-0.4 and nearby Fermi sources. 16
2.5 MeerKAT image of the region of HESS J1457-593 with overlaid H.E.S.S. source and overlaid SNR G318.2+0.1 and nearby Fermi sources 17
2.6 MeerKAT image of the region of HESS J1503-582 with overlaid H.E.S.S. source and possible associations. 18
2.7 MeerKAT image of the region of HESS J1702-420 with overlaid H.E.S.S. source and possible associations. 19
2.8 MeerKAT image of the region of HESS J1702-420 with overlaid H.E.S.S. significance contours (5, 7 and 9 sigma). 20
2.9 MeerKAT image of the region of HESS J1708-410 with overlaid H.E.S.S. source. 21
2.10 MeerKAT image of the region of HESS J1729-345 and HESS J1731-347 with overlaid H.E.S.S. sources. 22
2.11 MeerKAT image of the region of HESS J1843-033 and HESS J1844-030 with overlaid H.E.S.S. source and possible associations. 23
2.12 The combined synchrotron and inverse Compton model for HESS J1843-033. The red line shows the synchrotron part of the model and the green line shows the inverse Compton part of the model. 24
2.13 MeerKAT image of the region of HESSJ1844-030 with overlaid H.E.S.S. position contours (68% and 95%) and size upper limit. 26
2.14 MeerKAT image of the region around HESS J1833-105. The pink circle is the region used for measuring the radio flux. . . 28

2.15 The combined synchrotron and inverse Compton model for HESS J1833-105. The brown line shows the synchrotron part of the model and the purple line shows the inverse Compton part of the model. The MeerKAT, XMM-Newton and HESS data is plotted. Only the the XMM-Newton data point with the largest energy bin is used in the fitting. 29
2.16 MeerKAT image of the region around HESS J1826-148. The pink circle is the region used for measuring the radio flux. . . 30
2.17 The combined synchrotron and inverse Compton model for HESS J1826-148. The brown line shows the synchrotron part of the model and the purple line shows the inverse Compton part of the model. The MeerKAT, XMM-Newton and HESS data is plotted. Only the the XMM-Newton data point with the largest energy bin is used in the fitting. 31

3.1 Samplers fit for HESS J1640-465. The blue points are for the Fermi source 4FGL J1640.6-4632 and the green points for HESS J1640-465. The dark black line is for the parameters with the maximum log likelihood value of the samplers. The χ^2 p-value is 0.34. 33
3.2 Gamma-ray emission and Neutrino emission plotted together for HESS J1640-465. The blue points are for the Fermi source 4FGL J1640.6-4632 and the green points for HESS J1640-465. The blue line is for the the gamma-ray emission and the orange line is for the neutrino emission. 34
3.3 A plot of the samplers fit for HESS J1713-397. The blue points are for the Fermi source 4FGL J1713.5-3945e and the green points for HESS J1713-397. The dark black line is for the parameters with the maximum log likelihood value of the samplers. The χ^2 p-value is 4.2×10^{-8}. 35
3.4 Gamma-ray emission and Neutrino emission plotted together for HESS J1713-397. The blue points are for the Fermi source 4FGL J1713.5-3945e and the green points for HESS J1713-397. The blue line is for the the gamma-ray emission and the orange line is for the neutrino emission. 36
3.5 Predicted neutrino flux of the Milky Way per energy bin from galactic longitude 75° to 31°. 37
3.6 Predicted neutrino flux of the Milky Way per energy bin from galactic longitude 75° to 31°. 38
3.7 Predicted neutrino flux of the Milky Way per energy bin from galactic longitude 31° to 347°. 39

3.8 Predicted neutrino flux of the Milky Way per energy bin from galactic longitude 31° to 347°. 40
3.9 Predicted neutrino flux of the Milky Way per energy bin from galactic longitude 347° to 303°. 41
3.10 Predicted neutrino flux of the Milky Way per energy bin from galactic longitude 347° to 303°. 42
3.11 Predicted neutrino flux of the Milky Way per energy bin from galactic longitude 303° to 259°. 43
3.12 Predicted neutrino flux of the Milky Way per energy bin from galactic longitude 303° to 259°. 44
3.13 Histogram of the number of associations for the randomised neutrino data. 46
3.14 Predicted Neutrino map from galactic longitude 75° to 347° overlaid with the neutrinos from the 2007-2017 ANTARES search for cosmic neutrino point sources. 47
3.15 Predicted Neutrino map from galactic longitude 347° to 259° overlaid with the neutrinos from the 2007-2017 ANTARES search for cosmic neutrino point sources. 48
3.16 Predicted Neutrino map from galactic longitude 75° to 347° overlaid with the neutrinos from the 2007-2017 ANTARES search for cosmic neutrino point sources that overlap with the regions of the predicted neutrino emission. 49
3.17 Predicted Neutrino map from galactic longitude 347° to 259° overlaid with the neutrinos from the 2007-2017 ANTARES search for cosmic neutrino point sources that overlap with the regions of the predicted neutrino emission. 50

List of Tables

2.1 List of H.E.S.S. unidentfied sources without association in the 1st and 4th quadrant of the Milky Way. The size is the $1\,\sigma$ radius of a two-dimensional Gaussian fit to the data. Pointlike sources have no size. 10
2.2 Measured flux of MeerKAT radio emission in the region of H.E.S.S. sources. 11
2.3 Parameters of electron population that describes the combined synchrotron and inverse compton model for HESS J1843-033, HESS J1833-105 and HESS J1826-148. The electron energy is the total energy in electrons and B is the magnetic field. . . . 28

3.1 Table of fitted parameters for the proton spectra. The Neutrino flux in the energy range 1 TeV to 100 TeV. The reference energy for normalisation is 1 TeV. 52

Abbreviations

H.E.S.S. - High Energy Stereoscopic System

HGPS - H.E.S.S. Galactic Plane Survey

SNR - Supernova Remnant

PSR - Pulsar

PWN - Pulsar Wind Nebula

SKA - Square Kilometer Array

KM3NeT - Cubic Kilometer Neutrino Telescope

LAT - Large Area Telescope

3FGL - Fermi LAT 4-year Point Source Catalog

4FGL - Fermi LAT 10-year Point Source Catalog

HE - High Energy

VHE - Very High Energy

MCMC - Markov Chain Monte Carlo

2FHL - Second Fermi-LAT Catalog of High-Energy Sources

XMM - X-ray Multi-Mirror Mission

XGPS - XMM-Newton Galactic Plane Survey

2MASS - Two Micron All-Sky Survey

PMN - Parkes-MIT-NRAO

IC - Inverse Compton

CMB - Cosmic Microwave Background

1: Introduction

1.1 Why study gamma rays

Most astronomy is concerned with the study of sources of photons, this covers the electromagnetic spectrum from radio waves (low energy photons) to very-high-energy gamma rays. VHE gamma rays are photons which are >100 GeV. There are many sources of gamma rays both in our Galaxy and beyond it, these include: neutron stars, black holes, supernova remnants, pulsars, gamma-ray bursts, active galactic nuclei and more. It is hoped that by studying gamma rays, the answer to the origin and acceleration of cosmic rays can be found. Cosmic rays are charged particles, usually high-energy protons and nuclei. They have a spectrum ranging from 10^9 eV to over 10^{20} eV. They were discovered by Victor Hess in 1912[1]. Cosmic rays are bent by magnetic fields which makes it difficult to determine their origin, this is not a problem for gamma rays since they have no charge. By identifying sources that can accelerate particles to the PeV energy range we can start to answer the question of the origin of cosmic rays. The identification of these sources relies mostly on photons that propagate in a straight line. The more energetic gamma rays produced by cosmic-ray interactions give a direct insight into the accelerators and the target of observation[2]. By detecting sources in multiple wavelengths, the entire spectrum of the photons coming from the source can be detected and tell us more about the mechanism emitting these photons and the object itself.

1.2 Problem under investigation

The High Energy Stereoscopic System (H.E.S.S.) Galactic plane survey (HGPS) is a very high energy gamma ray survey of the Galactic plane in the Galactic longitude range from 250° to 64° and with Galactic latitude $\leq 3°$ [3]. This survey identified 78 sources, 47 of these have no identified counterparts and are unknown sources. The project is going to have two main parts: the first is to determine some of the unidentified sources in the HGPS using the radio counterparts observed by MeerKAT and the second is to determine the expected neutrino emissions from the sources in the HGPS.

The first part uses the recently acquired data from the MeerKAT[4] array a precursor to the SKA project. The data from the MeerKAT Galactic plane survey[5] will be used to find radio counterparts to the H.E.S.S. sources. These will be used to identify the nature of the source if possible. The goal

is to find out if the source is driven by a pulsar and thus is likely leptonic emission.

In the second part the goal is to predict the neutrino emission for the sources with likely hadronic emission, this will be done using the model in Kelner et al. [6]. The predicted neutrino emission will then be compared to the possible neutrino point sources detected by ANTARES[7].

1.3 Aim

To identify the unidentified sources in the survey by looking at their radio counterparts detected by MeerKAT and to determine the expected neutrino emission from the H.E.S.S. Galactic Plane Survey sources.

1.4 Hypotheses and questions

Gamma ray emission can be produced by relativistic electrons or relativistc protons. Relativistic electrons can produce synchrotron radiation in the radio to X-ray range and inverse Compton emission in the gamma-ray range, this is the leptonic scenario. Relativistic protons collide with interstellar material, from these inelastic collisions pions are produced. The decay of pions leads to the production of gamma rays and neutrinos, this is the hadronic scenario. The main question is about the H.E.S.S. unidentified sources. Is it leptonic or hadronic emission?

1.5 H.E.S.S.

The H.E.S.S. telescopes use the Cherenkov technique to detect very high energy gamma rays [8]. A very high energy gamma ray enters the Earth's atmosphere and generates an air shower of secondary particles, these secondary particles (electrons and positrons) are created through pair production. The number of shower particles reaches a maximum at around 10km above sea level. The shower of these secondary particles moves at a speed exceeding the speed of light in the atmosphere and emits Cherenkov light. The Cherenkov light illuminates an area of about 250m in diameter. If a telescope is inside this area it will detect the Cherenkov light and produce an image of the track of the air shower. From this the direction of the initial gamma ray can be determined as well as its energy. The intensity of the image is related to

the energy of the incident gamma ray. The arrival direction of the primary photon can be reconstructed with an accuracy of 0.08° and the energy of the primary proton can be reconstructed with an accuracy of 15%. The H.E.S.S. telescopes allow for stereoscopic reconstruction of the air shower and the direction of the incoming gamma ray. This means that more telescopes allow for better reconstruction of the air shower and better measurements of the direction of the incoming gamma ray. H.E.S.S. is made up of 5 telescopes. Initially four smaller telescopes, 12m in diameter, were built and arranged in a square with a side length of 120m. Later a 5th telescope, 28m in diameter, was added to the middle of the square. All the telescopes can rotate and the smaller telescopes can tilt from pointing at the ground to pointing to the vertical, while the large telescope can tilt from -125 degrees to 90 degrees from vertical. When the large telescope is in its parked position it is at 45 degrees below the horizon (this is the -125 degrees). The 90 degrees from vertical is for inverted pointing but is not currently used. The motions of the five telescopes allow them to point to any position in the sky.

1.6 H.E.S.S. Galactic Plane Survey

The HGPS mapped the galactic plane from $l = 250°$ to $l = 65°$ in Galactic longitude and $|b| \leq 3°$ in Galactic latitude in the very-high-energy gamma-ray range (0.1 TeV to 100 TeV) [3]. This survey has detected 78 very-high-energy gamma-ray sources. This survey only uses the phase 1 telescopes (the four smaller ones), with an energy threshold of 0.2 TeV. Of the 78 sources observed, 31 were firmly identified, a further 36 had an association with a known source and 11 have no associations. 12 of the known sources are pulsar wind nebulae (PWN), 8 are supernova remnants (SNR), 8 are composite supernova remnants and 3 are gamma-ray binaries.

1.7 Neutrino telescopes

1.7.1 ANTARES

ANTARES (**A**stronomy with a **N**eutrino **T**elescope and **A**byss environmental **Res**earch project) is a neutrino telescope located in the Mediterranean Sea and is the precursor to KM3NeT. It's primary goal is to search for TeV to PeV astrophysical neutrinos and it also offeres facilities for marine and Earth sciences[9]. It's location, 40 km offshore from Toulon (France) and at a depth of 2475 m, gives it a clear visibility of the Galactic Plane. It also

has a very good angular resolution of 0.3° at energies above 10 TeV which makes it an excellent tool for searching for point sources. The telescope is optimised for detecting high energy neutrinos travelling through the Earth in an upward trajectory. It detects neutrinos by observing the Cherenkov light produced in the water from secondary charged leptons. These leptons are created due to the interaction of a neurino with the matter surrounding the instrument. Neutrinos interacting with matter up to 10 km away from the detector can be detected. The neutrino detector is made up of a matrix of light detectors. These light detectors are photomultipliers contained in glass spheres and attached to flexible lines anchored to the seabed. To detect the neutrino the muon path is reconstructed by measuring the arrival times of the Cherenkov photons at the light detectors.

In Illuminati et al. [7][10] 11 years of ANTARES data is presented from 29 January 2007 to 31 December 2017, a total livetime of 3125.4 days. Three different search methods were used to search for astrophysical neutrinos: a scan over the sky visible to ANTARES, a survey of 112 astrophysical candidates and an investigation of 75 IceCube tracks. Over the 11 years no significant evidence of cosmic neutrinos was found. For the ANTARES data the median angular resolution is 0.4° for track like events and 3° for shower like events. In this data set there are 8754 tracks and 195 showers. This is a public data set and is used later in section 3.3 to test the predicted neutrino emission map.

1.7.2 Future neutrino detectors

IceCube is a detector built into the ice in Antarctica. It is designed to detect neutrinos. Neutrinos are extremely difficult to detect. IceCube has 5160 optical sensors viewing 1 cubic kilometer of ice [11]. IceCube is designed to detect neutrinos with an energy greater than 100 GeV. At low energies IceCube is able to differentiate between muon neutrinos and the rest (electron neutrinos, tau neutrinos and all flavour neutral current neutrinos) based on the tracks the Cherenkov light produces in the ice. At high energies (PeV) muon tracks can be up to 10 km long. IceCube is able to detect neutrinos from anywhere because high energy neutrinos are able to pass through the Earth, however it has better sensitivity for resolving sources that are in the Northern hemisphere where the charged particle backgrounds are completely removed by absorption in the Earth. To observe neutrino emission in the Southern hemisphere IceCube is able to select only high energy events which allows it to detect high energy sources. Good energy estimates of the atmospheric neutrinos are required to reject the atmospheric neutrino events

when selecting cosmic events in the Southern hemisphere.

The KM3NeT or Cubic Kilometer Neutrino Telescope is a neutrino detector that is being built in the Mediterranean sea. The detection of neutrinos in KM3NeT is similar to that of IceCube in that it detects the secondary particles created by neutrino interaction. It also looks at the two different patterns created by the Cherenkov light but in KM3NeT it is in water rather than ice. The KM3NeT is not just one detector but rather three detectors all built in the same "flexible design" but with different sizes and all using the same technology [12]. Each detector has 115 detection units. Equally spaced along the detection units are 18 digital optical modules. Each of the digital optical modules has 31 photomultiplier tubes. Each detector is a 3 dimensional array of photo sensors. Two of the detectors will be placed at a depth of 3500m and occupy 0.5 Gton of sea water. The third will be placed at a depth of 2500m and occupy 8 Mton of sea water.

KM3NeT is built in the Northern hemisphere and thus is better suited to detecting neutrinos in the Southern hemisphere, the Galactic centre is visible about 75% of the time [13]. The detector is in the optimal location for viewing the Galactic centre. The easiest way to identify neutrino induced muons is to select only the tracks that go upwards.

1.8 MeerKAT

MeerKAT is the precursor to the Square Kilometer Array (SKA), it is made up of 64 interlinked receptors. Each receptor has three main components: 1. The antenna (a steerable dish on a pedestal) 2. A set of radio receivers 3. A set of associated digitisers [4]. The receptors are able to observe at an elevation between 15° and 88°. The receptors are able to point with an accuracy within 5″ with low wind conditions at night and with an accuracy of 25″ during normal operations. MeerKAT detects signals when an electromagnetic wave in the radio range bounces off the main reflector into the sub-reflector and focused into the feed horn which is part of the receiver. MeerKAT can detect frequencies from 0.58 GHz to 2.5 GHz. The sensitivity of the MeerKat is 60 μJy/beam[5]. MeerKAT performed a survey of the galactic plane as part of its commissioning phase which is not publicly available. This survey covers the Galactic plane from 280° to 350° in Galactic longitude and from $-1°$ to 1° in Galactic latitude.

1.9 Fermi

The Fermi spacecraft carries two instruments on board: The Large Area Telescope (LAT) and the Gamma-ray Burst Monitor (GBM). The LAT has the following properties: an energy range of 20 MeV to 1 TeV, an effective area at normal incidence of 9500 cm^2, an energy resolution of 6% to 18%, an angular resolution of 0.15° to 3.5°, a field of view of 2.4 steradians, a timing accuracy of 10 microseconds and an event readout time of 26.5 microseconds [14]. The Fermi LAT is a pair-conversion telescope which means it detects gamma rays by converting the gamma ray into a pair of an electron and a positron, from this pair the direction and energy of the initial photon can be determined. The LAT is made up of four instruments: a precision converter-tracker, a calorimeter, a segmented anticoincidence detector and a programmable trigger and data acquisition system.

The 4FGL catalog, which is publicly available, is made from data collected over 8 years, starting in 2008. This catalog contains gamma rays from 50 MeV to 1 TeV [15]. The 4FGL catalog has 5064 sources in it. The 4FGL made firm identifications for 358 of the sources and made associations for another 3370 sources while 1336 are unassociated. In the catalog there are: 239 Pulsars, 17 pulsar wind nebulae, 40 supernova remnants, 78 that are either supernova remnants or pulsar wind nebulae, 30 globular clusters, 3 star forming regions, 11 binaries, 1 nova, 3137 blazars, 42 radio galaxies, 11 non-blazar active galactic nuclei, 2 steep spectrum radio quasars, 5 compact steep spectrum radio sources, 9 narrow-line Seyfert 1, 1 Seyfert galaxy, 7 starburst galaxies and 3 normal galaxies.

1.10 Mechanisms of gamma-ray emission

There are two main categories of cosmic gamma ray production, leptonic and hadronic[2]. High energy electrons and positrons interact with magnetic fields and produce synchrotron photons. Synchrotron photons are produced when relativistic charged particles (positrons and electrons) are accelerated perpendicularly to their velocity. The energy of synchrotron photons reaches up to X-rays and at most low-energy gamma rays. The energy of the synchrotron photons and the intensity of the synchrotron emission are dependent on the magnetic field. These charged particles can also interact with the ambient low-energy photons which can boost them to the gamma-ray and VHE gamma-ray energies because the photon is scattered by the charged particle

which transfers some of its energy to the photon. This is known as the Inverse Compton effect. The energy spectrum of the scattered photons depends strongly on the energy of the target photon[16]. In many cases the the dominant contribution of the inverse scattering comes from photons belonging to blackbody radiation, this is the case for the Cosmic Microwace Background (CMB). This is the leptonic mechanism of gamma-ray production.

The hadronic production of gamma rays involves high-energy protons and nuclei interacting with matter through nuclear interactions. These interactions happen in denser regions of the interstellar medium. When the proton scatters off the matter it produces a neutral meson, this is inelastic proton-proton scattering. The neutral mesons then decays into gamma rays, $\pi^0 \rightarrow 2\gamma$. These gamma rays are able to reach energies >100 TeV but the energy spectrum of the gamma ray reaches a maximum at approximately 68 MeV (half the energy of the neutral pion) and decreases slowly according to a power law whose spectral index is similar to that of the incident particle[2]. The charged pions decay into neutrinos, $\pi \rightarrow \mu + \nu_\mu$. The intensity of the outgoing gamma rays and the neutrino flux are proportional to the ambient density.

1.11 Modelling gamma-ray emission

Parametrisations for the energy spectra of secondary particles (π mesons, gamma rays, electrons and neutrinos) produced in proton-proton collisions are presented by Kelner et al. [6]. These parametrisations can be used for energy distributions of secondary particles in the energy range > 100 GeV and have an accuracy better than 10%. These parametrisations can be used to model the gamma-ray and neutrino emission from proton-proton collisions. This was used to create our model (which can be seen in appendix B) from which the gamma-ray data is fitted and then the prediciton of neutrino emission is made.

Naima is a python package that computes the non-thermal radiation from relativistic particle populations, it also has tools for performing MCMC (Markov Chain Monte Carlo) fitting of radiative models to observed spectra [17]. The models available are: synchrotron, inverse Compton, Bremsstrahlung and neutral pion decay processes.

For modelling hadronic emission, Naima has a Pion decay model. This model is based on analytic parametrisations to the energy spectra and pro-

duction rates of gamma rays from proton-proton interactions developed in [18]. This is only able to model the gamma ray emission and not the neutrino emission. The accuracy of this model is better than 20%. This model can be used for energies > 2 GeV.

For modelling leptonic emission, Naima has an inverse Compton model. This model is based on the analytical approximations developed in [16]. The model provides an accuracy as good as 1%. This model is used to model the gamma-ray emission from leptonic interactions. Naima also has a synchrotron model based on the work done by Aharonian et al. [19]. This parametrisation is accurate to 0.2% over the entire energy range of emission. Synchrotron emission is present in the emitted spectrum of leptonic sources when there is a magnetic field.

2: Searching for the unidentified H.E.S.S. sources in the MeerKAT Galactic plane survey

2.1 Unidentified Sources

MeerKAT's Galactic plane survey covers the 1st and 4th quadrant of the Milky Way, from 2° to 40° and 268° to 358° respectively. In this region H.E.S.S. detected 38 VHE sources that are flagged as unidentified in the catalogue. H.E.S.S. Collaboration[3] identify possible associations of these sources with objects seen in other wavelengths. 29 of the sources have plausible associations, like pulsar wind nebulae or supernova remnants. The remaining 9 sources have no association or are only associated with a high-energy (HE) source seen by *Fermi*/LAT(3FGL and 2FHL catalogues). These objects are listed in Table 2.1. A search for radio counterparts to these 9 sources was performed in the existing data taken with MeerKAT. 8 of the 9 sources in the first and fourth quadrant of the Milky Way were inside the region for which we have MeerKAT data. HESS J1626-490 was just outside of the region for the MeerKAT data.

The MeerKAT data was collected over 4 sessions[1], from 21 July 2018 to 26 July 2018. The first session on 01 July had 7 target pointings for 70.9 minutes per pointing. The second session on 22 July had 7 target pointings for 73.5 minutes per pointing. The third session on 23 July had 7 target pointings for 97.1 minutes per pointing. The fourth session on 26 July had 9 target pointings for 53.3 minutes per pointing. The data is primary beam corrected and is in the form of 3×3 degrees cubes with 14 frequencies.

The MeerKAT galactic plane survey provides two types of images plates: Moment0 plates are integrated over the frequency range. Thay have an effective frequency of 1.29 GHz and a bandwidth of 0.67 GHz. The spatial information is binned into pixels of 1.5" x 1.5". These images are used to search for radio emission correlated with the gamma-ray emission. Additionally, the data is provided with the same spatial binning and an additional binning into 14 frequency channels from 908.412 MHz to 1656.724 MHz. These frequency cubes are used to extract the radio spectrum.

[1]This is information is provided with the data products.

Table 2.1: List of H.E.S.S. unidentfied sources without association in the 1st and 4th quadrant of the Milky Way. The size is the $1\,\sigma$ radius of a two-dimensional Gaussian fit to the data. Pointlike sources have no size.

Name	GLON $^\circ$	GLAT $^\circ$	size $^\circ$
HESS J1828-099	21.491	0.378	-
HESS J1832-085	23.207	0.293	-
HESS J1858+020	35.545	-0.581	0.08
HESS J1457-593	318.354	-0.423	0.33
HESS J1503-582	319.567	0.286	0.28
HESS J1626-490	334.816	-0.124	0.20
HESS J1702-420	344.233	-0.186	0.20
HESS J1708-410	345.671	-0.436	0.06
HESS J1729-345	353.385	-0.016	0.19

2.2 Measuring MeerKAT Flux for H.E.S.S. Sources

The MeerKAT data has 14 frequency channels from 908.412 MHz to 1656.724 MHz but two of the channels don't have data since there is inteference in their frequency range. To measure the flux all the pixels were added up inside area corresponding to the 1 sigma extension of the H.E.S.S. source. For point-like H.E.S.S. sources the pixels were added up inside the closest point-like source in the MeerKAT image, examples of this can be seen in Figs. 2.14 and 2.16. For some of the sources there were problems with other frequencies and no measurements were made for those frequencies. The error was estimated by taking the mean flux of background emission in a 0.1 degree circle. This was done for 8 sources and the results can be seen in Table 2.2.

Table 2.2: Measured flux of MeerKAT radio emission in the region of H.E.S.S. sources.

Frequency (MHz)	Flux(Jy)			
	HESS J1708-410	HESS J1718-374	HESS J1729-345	HESS J1731-347
908.142	$1.2463 \pm 2.4 \times 10^{-4}$	$20.3777 \pm 5.8 \times 10^{-3}$		
952.446	$1.0198 \pm 1.7 \times 10^{-4}$	$19.6332 \pm 5.8 \times 10^{-3}$		$0.8922 \pm 1.4 \times 10^{-4}$
996.751	$0.9540 \pm 9.6 \times 10^{-5}$	$19.0677 \pm 6.4 \times 10^{-3}$	$13.5529 \pm 1.9 \times 10^{-3}$	$0.7479 \pm 1.2 \times 10^{-4}$
1043.563	$0.6319 \pm 4.9 \times 10^{-5}$	$18.6285 \pm 5.4 \times 10^{-3}$	$11.1447 \pm 1.6 \times 10^{-3}$	
1092.884	$0.3712 \pm 2.3 \times 10^{-5}$	$17.9084 \pm 4.9 \times 10^{-3}$	$11.6190 \pm 1.4 \times 10^{-3}$	$0.4136 \pm 8.1 \times 10^{-5}$
1144.712	$0.2465 \pm 1.5 \times 10^{-5}$	$17.4138 \pm 3.8 \times 10^{-3}$	$11.1578 \pm 1.1 \times 10^{-3}$	$0.8283 \pm 1.2 \times 10^{-4}$
1317.751		$15.6672 \pm 3.7 \times 10^{-3}$	$6.7058 \pm 2.4 \times 10^{-4}$	$2.1503 \pm 1.1 \times 10^{-4}$
1381.7		$15.3791 \pm 3.1 \times 10^{-3}$	$6.2849 \pm 2.0 \times 10^{-4}$	$2.1911 \pm 8.8 \times 10^{-5}$
1448.157		$15.0163 \pm 2.7 \times 10^{-3}$	$5.5520 \pm 1.6 \times 10^{-4}$	$1.9704 \pm 9.3 \times 10^{-5}$
1520.048		$14.6491 \pm 2.1 \times 10^{-3}$	$5.1592 \pm 1.9 \times 10^{-4}$	
1594.446		$14.3996 \pm 2.0 \times 10^{-3}$		

Frequency (MHz)	Flux(Jy)			
	HESS J1813-178	HESS J1826-148	HESS J1833-105	HESS J1843-033
908.142	$3.0947 \pm 4.8 \times 10^{-4}$	$0.0351 \pm 1.6 \times 10^{-5}$		
952.446	$2.5958 \pm 3.5 \times 10^{-4}$	$0.0355 \pm 1.3 \times 10^{-5}$		$3.0898 \pm 2.1 \times 10^{-3}$
996.751	$2.4516 \pm 3.2 \times 10^{-4}$	$0.0358 \pm 1.0 \times 10^{-5}$	$7.0655 \pm 1.3 \times 10^{-3}$	$4.2457 \pm 2.7 \times 10^{-3}$
1043.563	$2.0009 \pm 1.8 \times 10^{-4}$	$0.0358 \pm 6.0 \times 10^{-6}$	$7.0324 \pm 9.6 \times 10^{-4}$	$4.7128 \pm 2.4 \times 10^{-3}$
1092.884	$1.5265 \pm 1.2 \times 10^{-4}$	$0.0369 \pm 3.6 \times 10^{-6}$	$7.0185 \pm 6.0 \times 10^{-4}$	$4.3347 \pm 2.1 \times 10^{-3}$
1144.712	$1.1234 \pm 9.5 \times 10^{-5}$	$0.0364 \pm 2.7 \times 10^{-6}$	$7.0119 \pm 5.6 \times 10^{-4}$	$3.5775 \pm 1.9 \times 10^{-3}$
1317.751	$0.8389 \pm 4.8 \times 10^{-5}$		$6.7676 \pm 4.0 \times 10^{-4}$	$3.5039 \pm 2.2 \times 10^{-3}$
1381.7	$0.9067 \pm 4.8 \times 10^{-5}$		$6.7851 \pm 3.9 \times 10^{-4}$	$3.5541 \pm 2.1 \times 10^{-3}$
1448.157	$0.8859 \pm 5.3 \times 10^{-5}$		$6.8243 \pm 3.8 \times 10^{-4}$	$3.7798 \pm 2.1 \times 10^{-3}$
1520.048	$0.9014 \pm 6.3 \times 10^{-5}$		$6.9027 \pm 4.5 \times 10^{-4}$	
1594.446				

2.3 Modelling the leptonic emission

The naima[17] python package was used to create a combined synchrotron and inverse Compton model. The combined model parametrises the electron population for the source, it takes the following parameters: normalisation, spectral index, cutoff energy and magnetic field. The normalisation is taken at the reference energy of 1 GeV. The minimum electron energy for the electron distribution is set to 511 keV. The synchrotron part of the model is based on the work by Aharonian et al. [19] and depends on all the parameters. The inverse Compton part of the model is based on the work by Khangulyan et al. [16]. The photon field is seeded only with the cosmic microwave background. The inverse Compton emission does not depend on the magnetic field. The synchrotron emission and inverse Compton emission are added to get the total emission. The electron spectrum is described by the following equation:

$$\mathrm{f}(E) = A \left(\frac{E}{E_0}\right)^{-\alpha} \exp\left(-\frac{E}{E_{\mathrm{cutoff}}}\right)^{\beta} \tag{2.1}$$

Where A is the normalisation, E_0 is the reference energy which is set to 1 GeV, α is the spectral index, E_{cutoff} is the cutoff energy and β is the cutoff exponent which is set to 1.

This combined model is used to fit the MeerKAT, H.E.S.S. and where possible Fermi data together. If it is possible to fit the data to this model it could be an indication that the source is leptonic since the model is . In total this model was used for three sources, one unidentified source HESS J1843-033 and two known sources HESS J1833-105 and HESS J1826-148. These were the only objects where the radio emission could be fitted reasonably well alongside the gamma-ray emission.

2.4 HESS J1828-099

HESS J1828-099 is a point-like source in TeV gamma rays. This makes it a good candidate for a gamma-ray binary. There are no counterparts seen in Fermi data. In the radio image (Fig. 2.1) there is one bright radio point source consistent with the position of HESS J1828-099. The radio source is unidentified. There are also 3 X-ray sources in the XMM catalog[20] consistent with the position of HESS J1828-099, they are XGPS-I J182858-095921, XGPS-I J182858-100002 and XGPS-I J182859-100043. The X-ray sources and the radio point source can be seen overlaid on a DSS optical

image in Fig 2.2. The three X-ray sources and the radio point source are all potential counterparts if the gamma-ray source is a binary but further invetigation is needed.

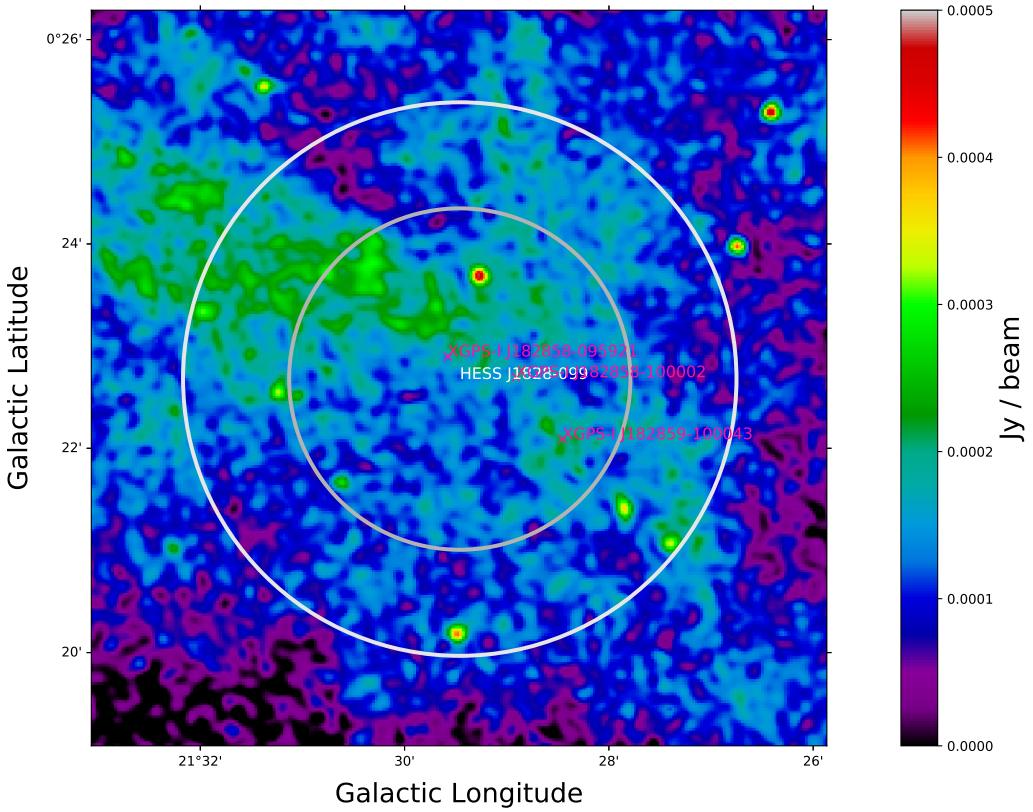

Figure 2.1: MeerKAT image of the region of HESS J1828-099 with overlaid H.E.S.S. position contours (68% and 95%) and positions of X-ray and 2MASS sources.

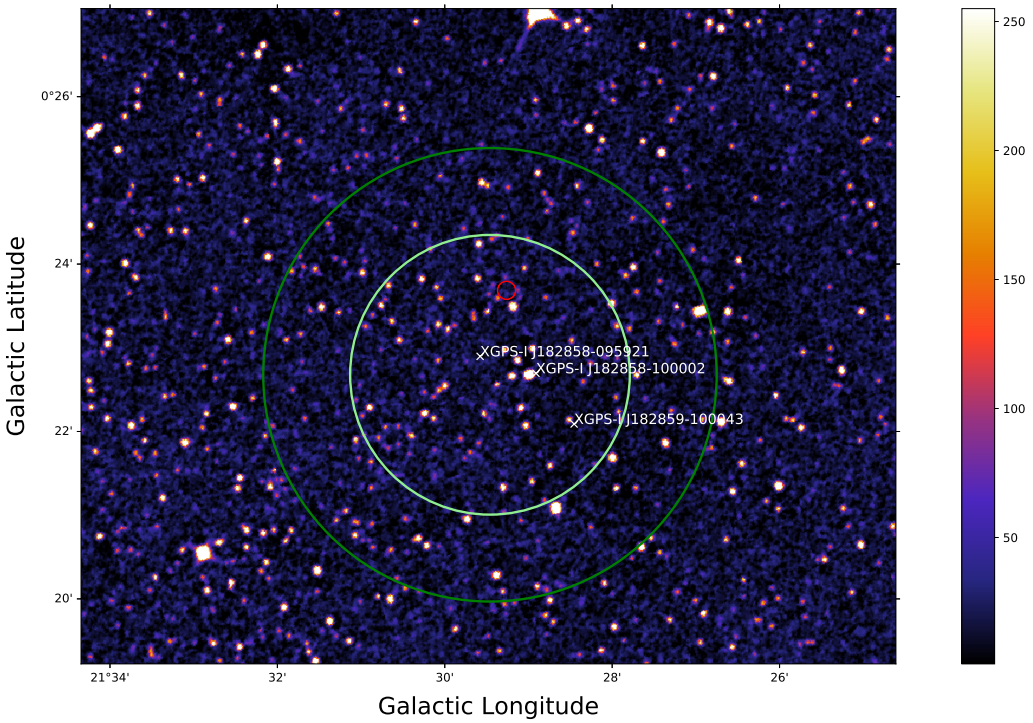

Figure 2.2: Optical image (DSS) of the region of HESS J1828-099 with overlaid H.E.S.S. position contours (68% and 95%) and positions of X-ray and 2MASS sources. The red circle is the postion of the bright radio point source.

2.5 HESS J1832-085

HESS J1832-085 is point-like in TeV gamma-rays. Maxted et al. [21] suggest that this source is a counterpart of SNR G23.11+0.18. They suggest that the TeV emission can be explained by a lingering population of cosmic ray protons that diffuse into nearby molecular gas. In Fig 2.3 you can see the radio image overlaid with the position of the source and the supernova remnant. The H.E.S.S. source is inside the region of SNR G23.11+0.18. There is radio emission detected by MeerKAT inside the 95% confidence region of the H.E.S.S. source position.

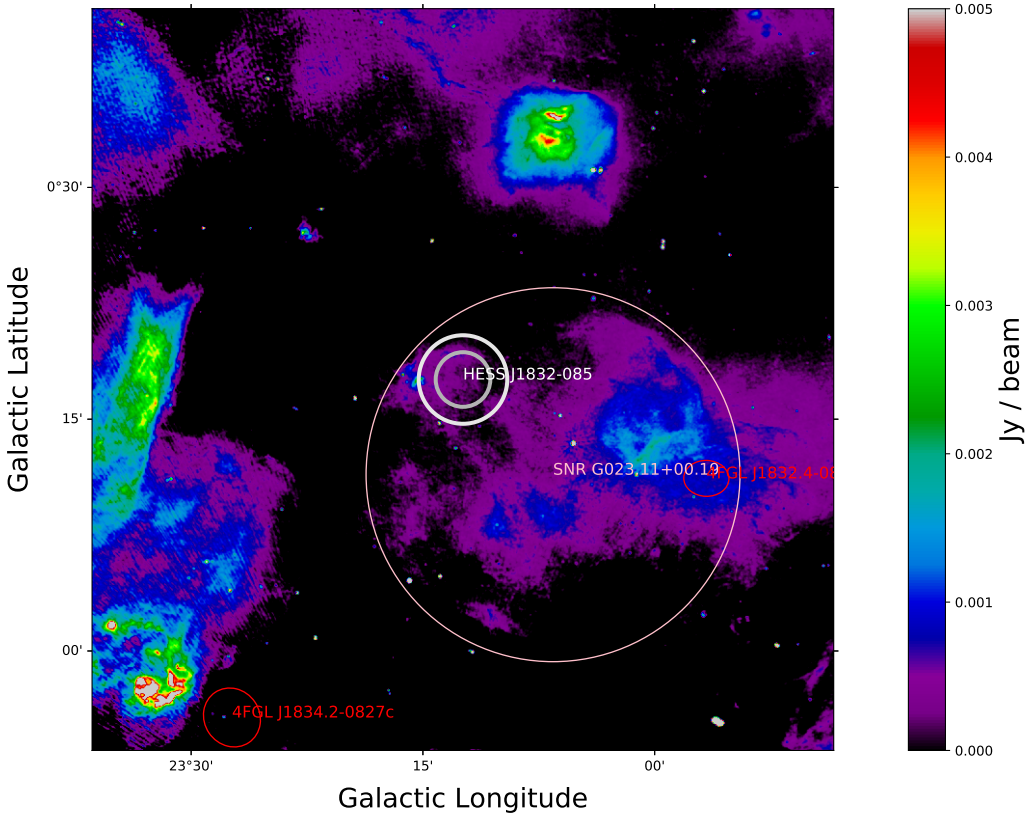

Figure 2.3: MeerKAT image of the region of HESS J1832-085 with overlaid H.E.S.S. position contours (68% and 95%) and overlaid SNR G23.11+0.18

2.6 HESS J1858+020

As can be seen in Fig 2.4 there is nearby radio emission as well as a nearby Fermi source 4FGL J1858.3+0209. The bulk of the radio emission is coincident with SNR G35.6-0.4. There is strong radio emission from the SNR and only faint radio emission from the position of the HESS source. Cui, Y. et al. [22] propose that this source is a counterpart of SNR G35.6-0.4. They show that cosmic rays from SNR G35.6-0.4 interacting with the moleculer cloud coincident with HESS J1858+020 can be used to explain the emission in the GeV to TeV range as seen by H.E.S.S. and Fermi.

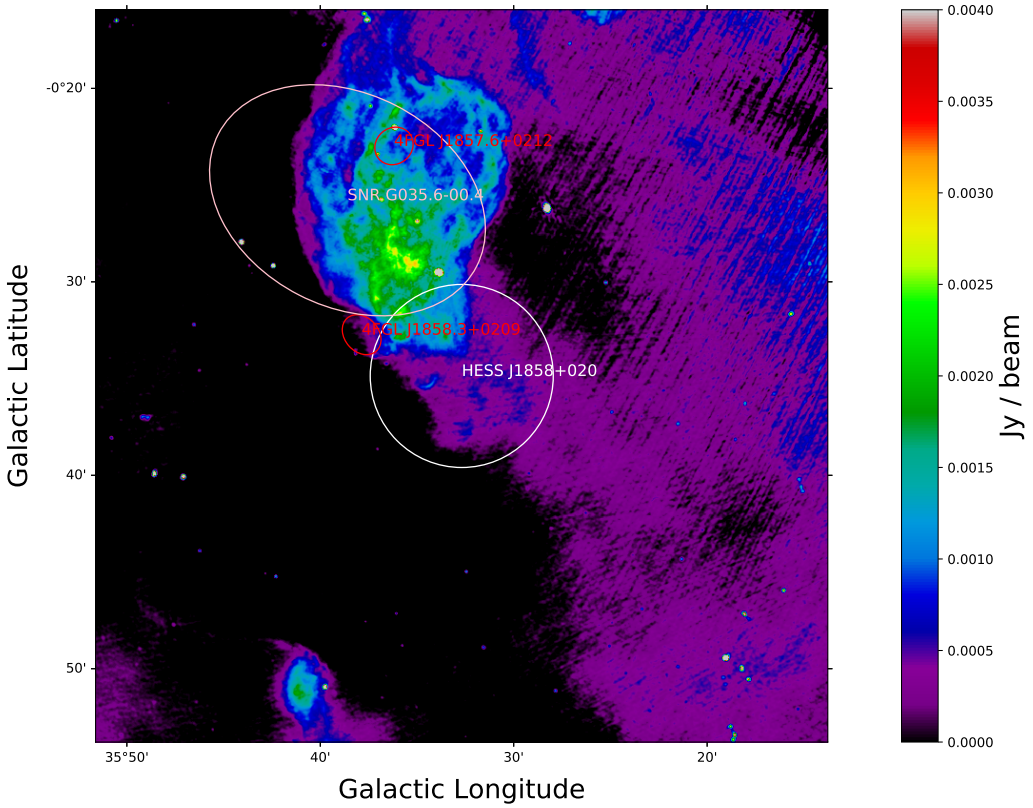

Figure 2.4: MeerKAT image of the region of HESS J1858+020 with overlaid with SNR G35.6-0.4 and nearby Fermi sources.

2.7 HESS J1457-593

This source has some nearby radio emission in the MeerKAT image. In Fig. 2.5 SNR G318.2+0.1 can be seen above the H.E.S.S. source with a small overlap however there is also radio emission towards the lower right of the H.E.S.S. source which looks more spatially coincident. Hofverberg et al. [23] suggest that the TeV emission could be a counterpart to the SNR G318.2+0.1, they claim that the H.E.S.S. emission could be as a result of interactions between SNR G318.2+0.1 and a giant molecular cloud.

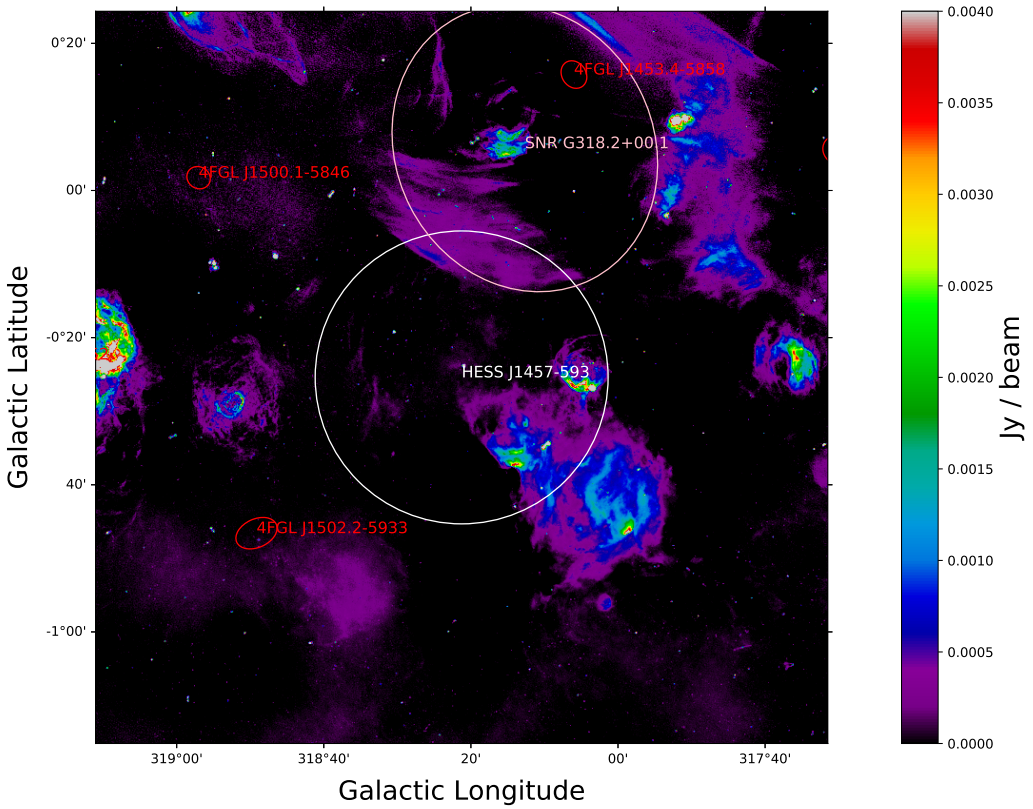

Figure 2.5: MeerKAT image of the region of HESS J1457-593 with overlaid H.E.S.S. source and overlaid SNR G318.2+0.1 and nearby Fermi sources

2.8 HESS J1503-582

There is no compelling association for this source with known objects. There are two Fermi sources in the region of the source. These are 2FHL J1505.1-5808 and 4FGL J1503.7-5801, both of which are unidentified. There is not much radio emission observed by MeerKAT in the region of this source which can be seen in Fig. 2.6. There is quite a lot of radio emission just to the lower right of the source.

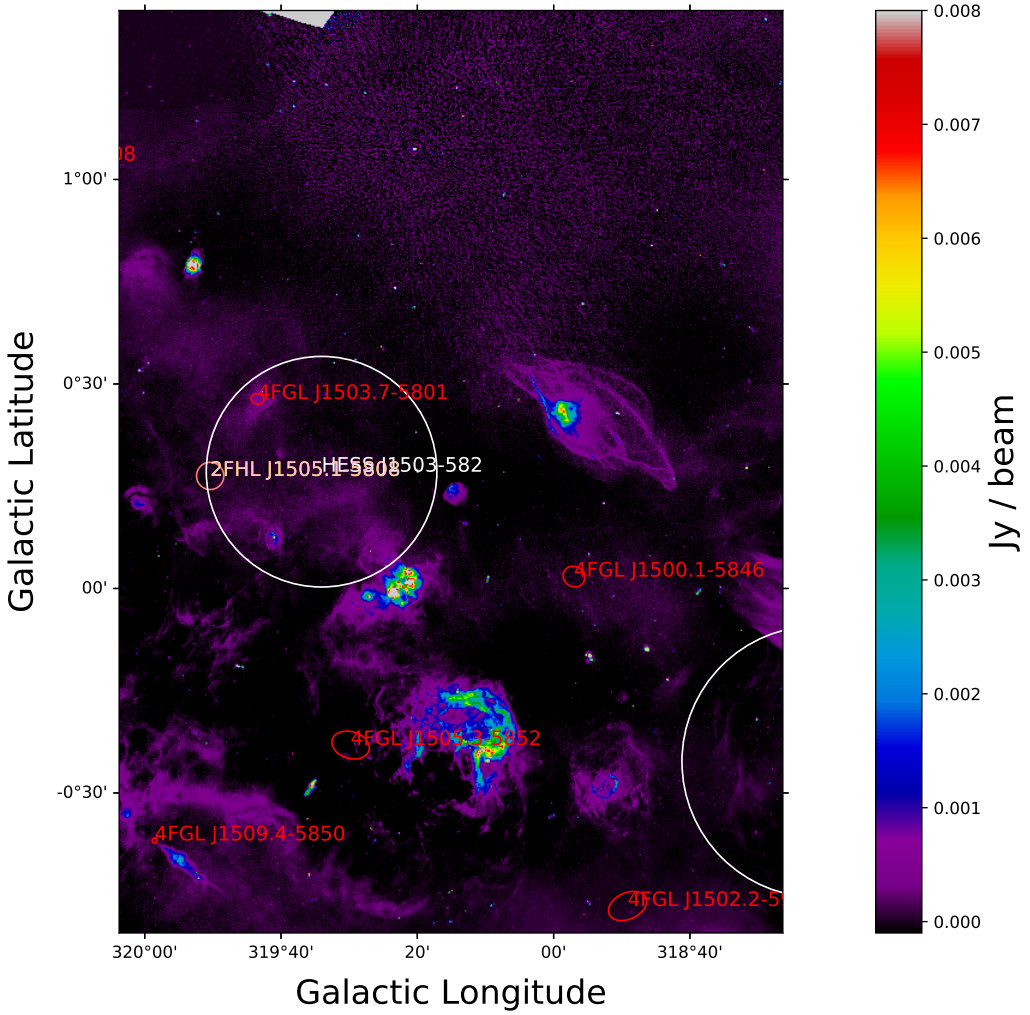

Figure 2.6: MeerKAT image of the region of HESS J1503-582 with overlaid H.E.S.S. source and possible associations.

2.9 HESS J1702-420

As seen in Fig. 2.7 to the left of the HESS J1702-420 lies SNR G344.7-0.1 and it is clearly seen in the MeerKAT data as well. There is also radio emission inside the region of HESS J1702-420. In Fig. 2.8 the significance contours of the H.E.S.S. source can be seen, these show that the source is quite extended. Eagle et al. [24] proposes that the H.E.S.S. emsission could come from SNR G344.7-0.1 cosmic rays accelerated by the forward shock that diffused into the inter stellar medium and interacted with a nearby molecular cloud.

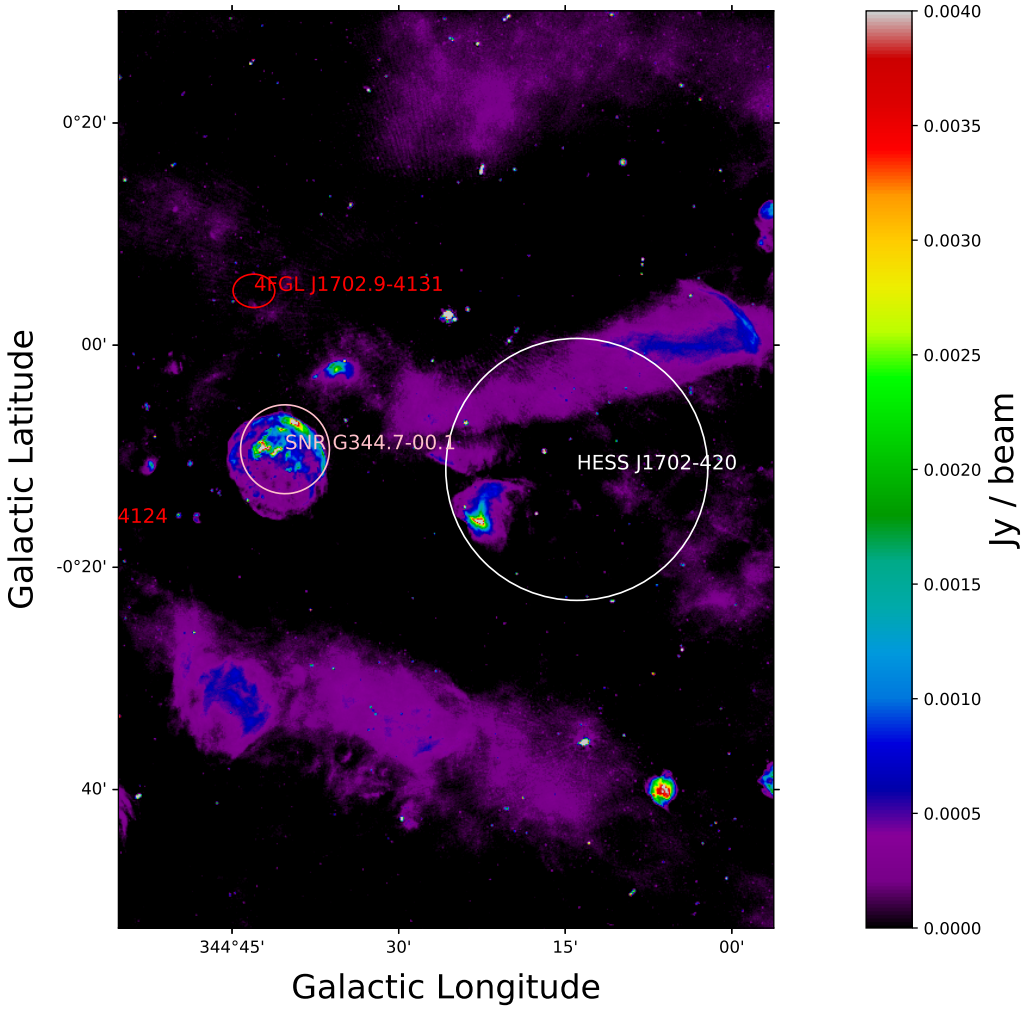

Figure 2.7: MeerKAT image of the region of HESS J1702-420 with overlaid H.E.S.S. source and possible associations.

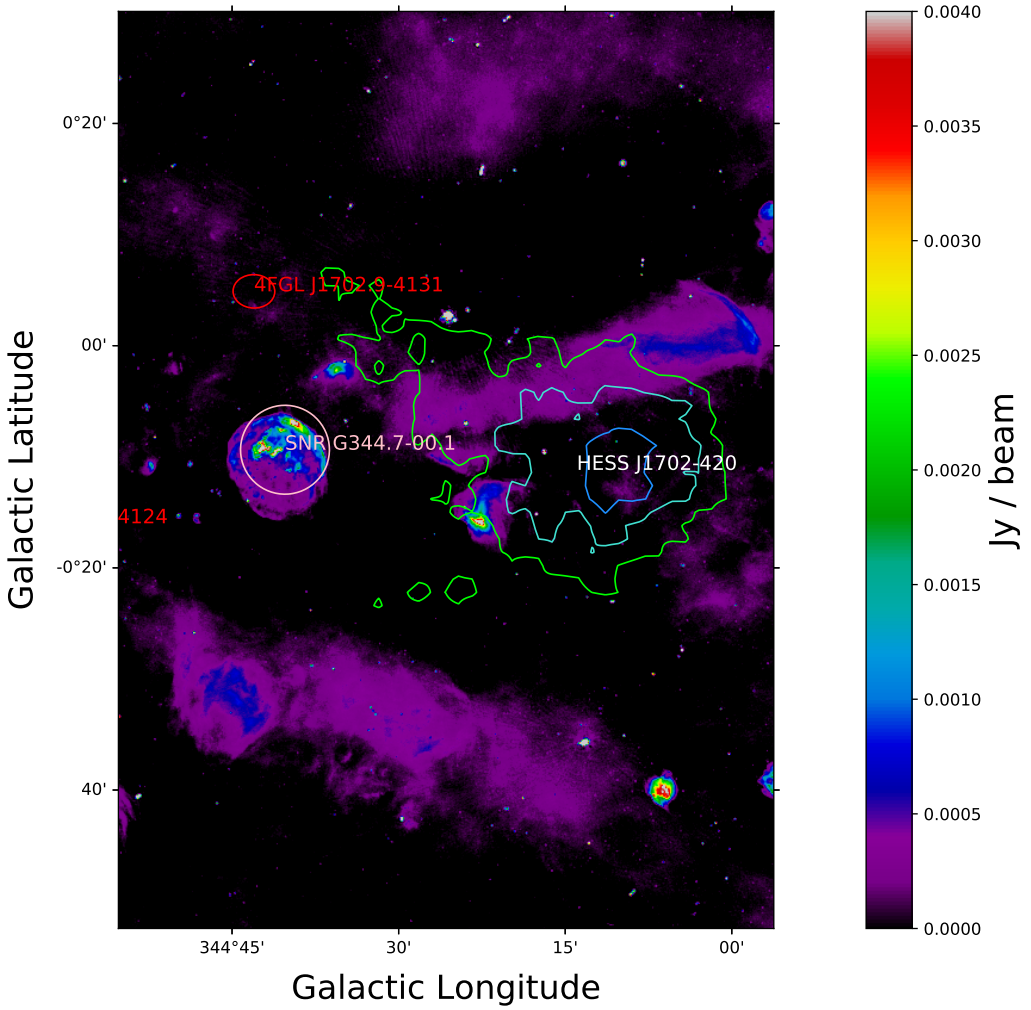

Figure 2.8: MeerKAT image of the region of HESS J1702-420 with overlaid H.E.S.S. significance contours (5, 7 and 9 sigma).

2.10 HESS J1708-410

There are no associations for this source and while there is some radio emission seen in the MeerKAT image there is nothing that is an obvious radio counterpart to the H.E.S.S. source, which can be seen in Figs. 2.9.

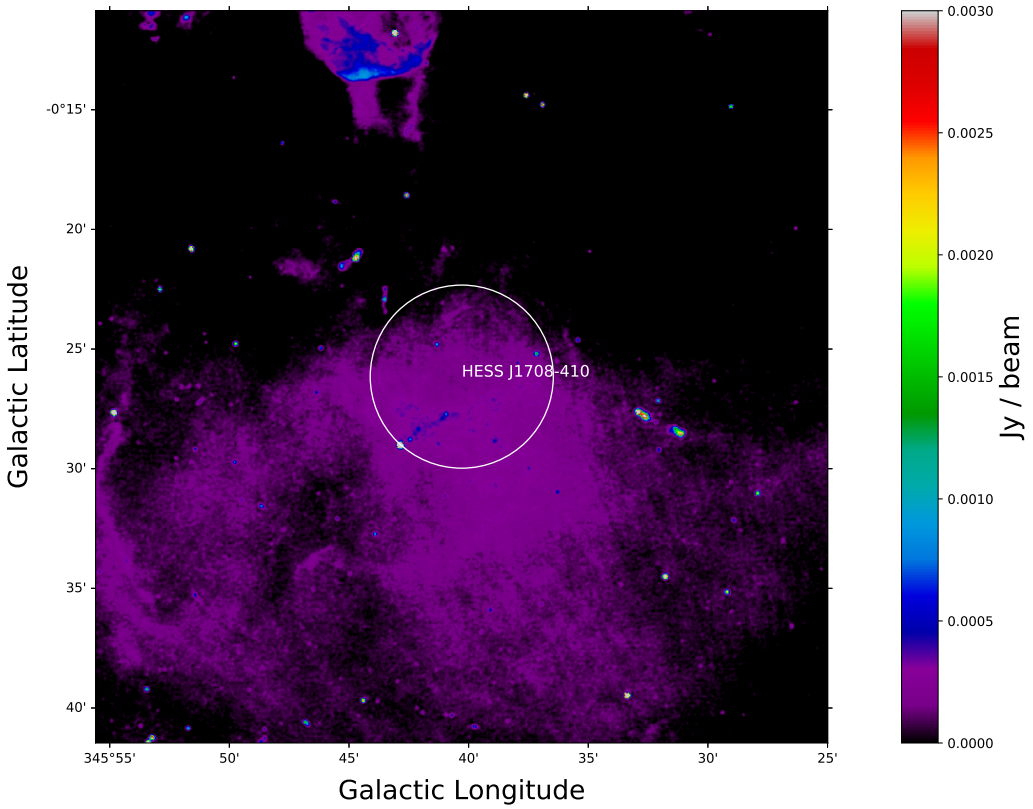

Figure 2.9: MeerKAT image of the region of HESS J1708-410 with overlaid H.E.S.S. source.

2.11 HESS J1729-345

A nearby TeV source HESS J1731-347 is a known source which is SNR G353.6-00.7. Also in the region of HESS J1729-345 is Fermi source 4FGL J1730.1-3422. In Fig. 2.10 there is a lot of radio emission in the region of HESS J1729-345. Capasso et al. [25] suggest that the emission from HESS J1729-345 can be explained by cosmic rays escaping from SNR G353.6-00.7 and interacting with molecular clouds.

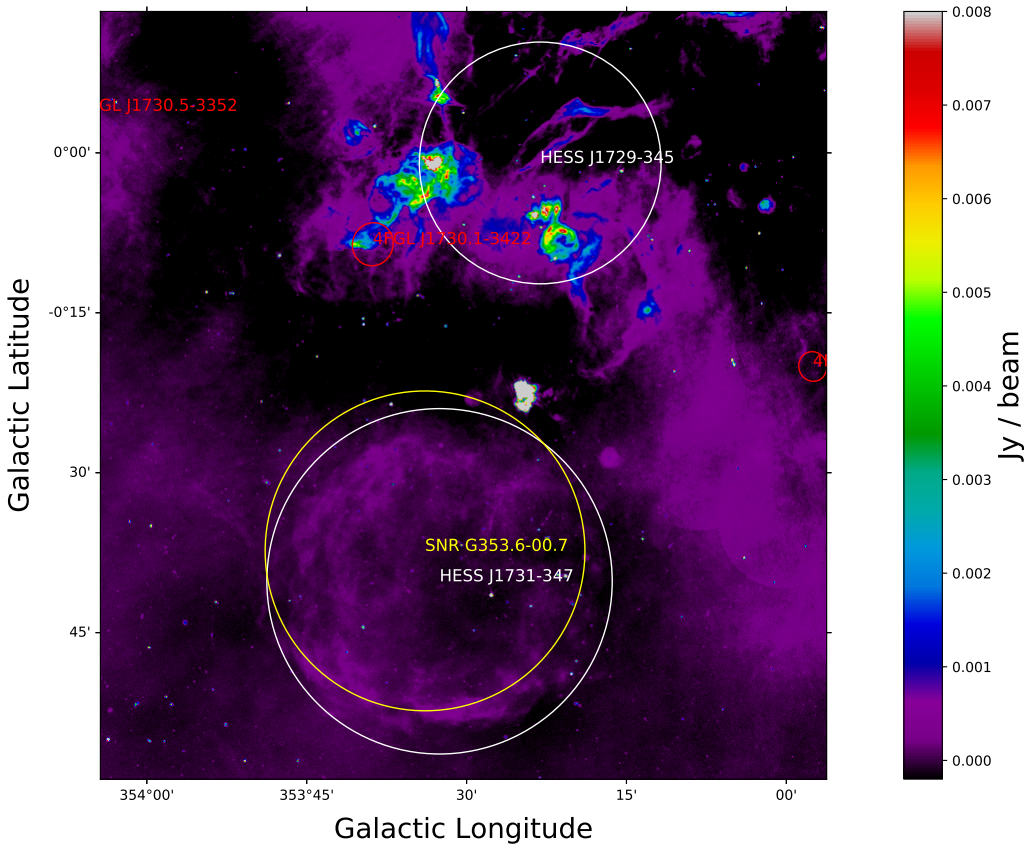

Figure 2.10: MeerKAT image of the region of HESS J1729-345 and HESS J1731-347 with overlaid H.E.S.S. sources.

2.12 HESS J1843-033

HESS J1843-033 has no associations with known sources. In Fig. 2.11 there are a number of nearby sources, the closest being 4FGL J1843.7-0326. There is also SNR G028.6-00.1 nearby to the source which is right at the edge of the VHE emission. There is a lot of radio emission observed by MeerKAT in the region around the source. The flux of the radio emission inside the H.E.S.S. region was measured, this is dicsussed in section 2.2. Table 2.2 shows the measured MeerKAT flux in the region of HESS J1843-033. The MeerKAT and H.E.S.S. measurements are then used to create a combined synchrotron and inverse Compton model using a single electron population. This model can be seen in Fig. **??**, the H.E.S.S. data is well described by the inverse Compton part of the model, the MeerKAT data is not as well described by the synchrotron part of the model but it is still able to make a reasonable

fit. The combined synchrotron and inverse Compton model describes the MeerKAT and H.E.S.S. data well and has a χ^2 p-value of 0.98. The parameters describing the electron population that produces this emission can be seen in Table 2.3. It's possible then that this source is leptonic but as seen in Fig. 2.12 there is a large flux in the X-ray energies predicted but only faint X-ray emission has been detected[3], so the emission from this source is probably produced by another mechanism.

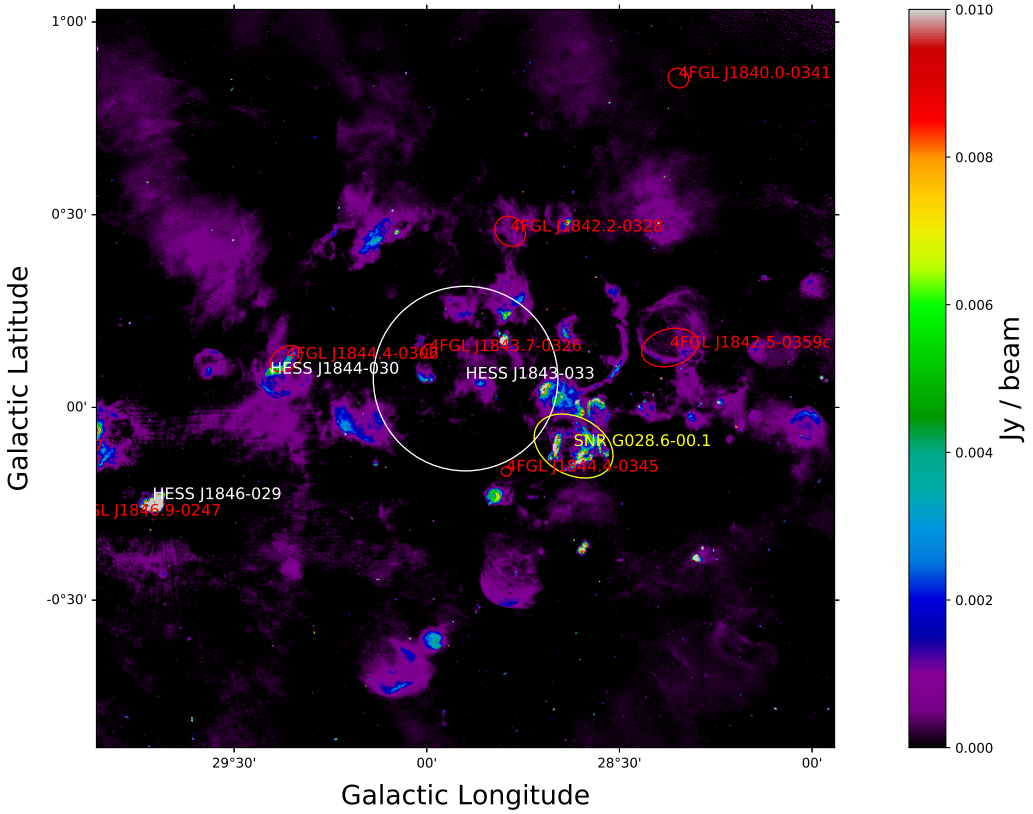

Figure 2.11: MeerKAT image of the region of HESS J1843-033 and HESS J1844-030 with overlaid H.E.S.S. source and possible associations.

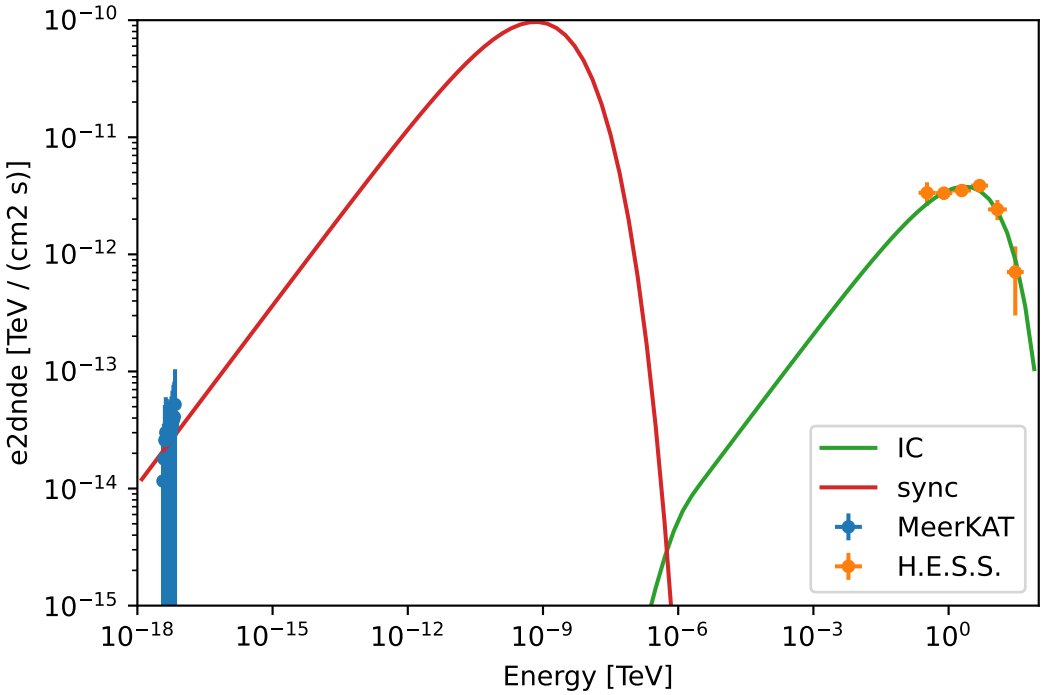

Figure 2.12: The combined synchrotron and inverse Compton model for HESS J1843-033. The red line shows the synchrotron part of the model and the green line shows the inverse Compton part of the model.

2.13 HESS J1844-030

HESS J1844-030 is a point-like source in TeV range, there is a radio galaxy PMN J1844-030 as well as a source in the *Fermi*/LAT catalog 4FGL J1844.4-0306 close to the H.E.S.S. source position (see Fig. 2.13). A bright jet-like feature and a faint shell are also seen in the radio emission. This jet-like feature is likely a radio galaxy and the shell is probably a SNR. The upper limit of the H.E.S.S. source is smaller than the radio shell but the emission could come from inside the SNR like a pulsar or PWN. The *Fermi*/LAT source is also in the region of the radio galaxy but on the opposite end to the H.E.S.S. source. The H.E.S.S. source is near the lower left lobe while the *Fermi*/LAT source is near the upper right lobe, as seen in Fig. 2.13. We would expect the *Fermi*/LAT source and the H.E.S.S. source to encompass the whole radio galaxy or at least be on the same side of the radio galaxy if they both originate from the radio galaxy.

Castelletti et al. [26] concludes that the brightest radio emission from G29.37+0.1 is probably a radio galaxy. There is X-ray emission coincident with the lower left part of the radio emission, this X-ray emission is likely a PWN. It was proposed that the faint radio halo represents a composite SNR with a pulsar powered component. The gamma-ray emission probably originates from the radio galaxy G29.37+0.1. It could not be determined if the gamma rays were from the core or the lobes of the radio galaxy.

Petriella [27] proposes that the emission from HESS J1844-030 has two probable origins: extra-galactic or galactic. In the extra-galactic case the gamma rays would originate from the lobes of the radio galaxy G29.37+0.1. In the galactic case HESS J1844-0330 would be the very high energy counterpart of the PWN G29.4+0.1. An investigation was carried out to determine if the gamma rays could have galactic origin and concluded that it is possible but not confirmed. A third suggestion for the origin of the gamma rays is that HESS J1844-030 could be a gamma-ray binary. This possibility could not be rejected but in order to confirm it variability needs to be detected in the gamma-ray emission.

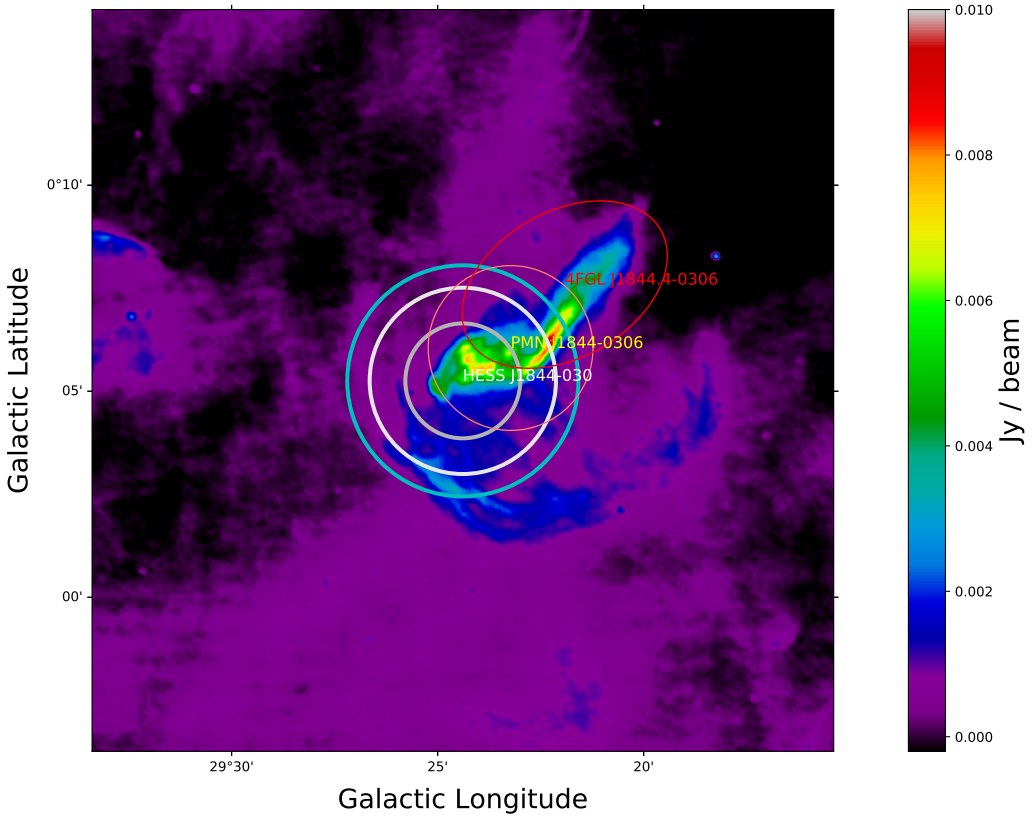

Figure 2.13: MeerKAT image of the region of HESSJ1844-030 with overlaid H.E.S.S. position contours (68% and 95%) and size upper limit.

2.14 Combined synchrotron and inverse Compton model for other sources

Since only one of our unknown sources had radio emission detected by MeerKAT that could be used to describe the source by a combined synchrotron and inverse Compton model some of the known sources were looked at. These sources and their radio fluxes can be seen in Table 2.2. Of these only HESS J1826-148 and HESS J1833-105 were nicely described by the combined syncrotron and inverse Compton model. The parameters for each of the sources can be seen in Table 2.3.

Since there is a large energy gap between the radio data and the gamma-ray data, it is useful to look at X-ray data. X-rays probe the synchrotron energy of the high energy electrons. There is X-ray data for HESS J1826-148 and HESS J1833-105 but not for HESS J1843-033. The X-ray data is taken from the XMM-Newton pipeline[28][2]. The pipeline has been run on 12210 XMM-Newton observations from 2000 until 2020. There are 602543 unique X-ray sources in the catalog. For the purpose of making the fit of the combined model only the X-ray data point with the largest energy bin is used.

HESS J1833-105 has been observered in X-rays by Safi-Harb et al. [29] and Bocchino et al. [30]. HESS J1833-105 has X-ray emission mostly from the pwn but an X-ray halo is also seen which is not seen in radio. The radio emission is only from the pwn. The X-ray data from the XMM-Newton pipeline is from the pwn and not the halo. This source has been firmly identified as the composite SNR G21.5-0.9, which contains a Crab-like PWN[3]. The combined fit for HESS J1833-105 is shown in Fig. 2.15 and the parameters of the fit are shown in Table 2.3. The radio and gamma-ray data are well fitted, the X-ray point with the largest energy bin is also well matched but the spectral index of the X-ray data is completely different to the model.

[2]The XMM-Newton data from the XMM-Newton source catalog can be found here: `http://xmm-catalog.irap.omp.eu/`

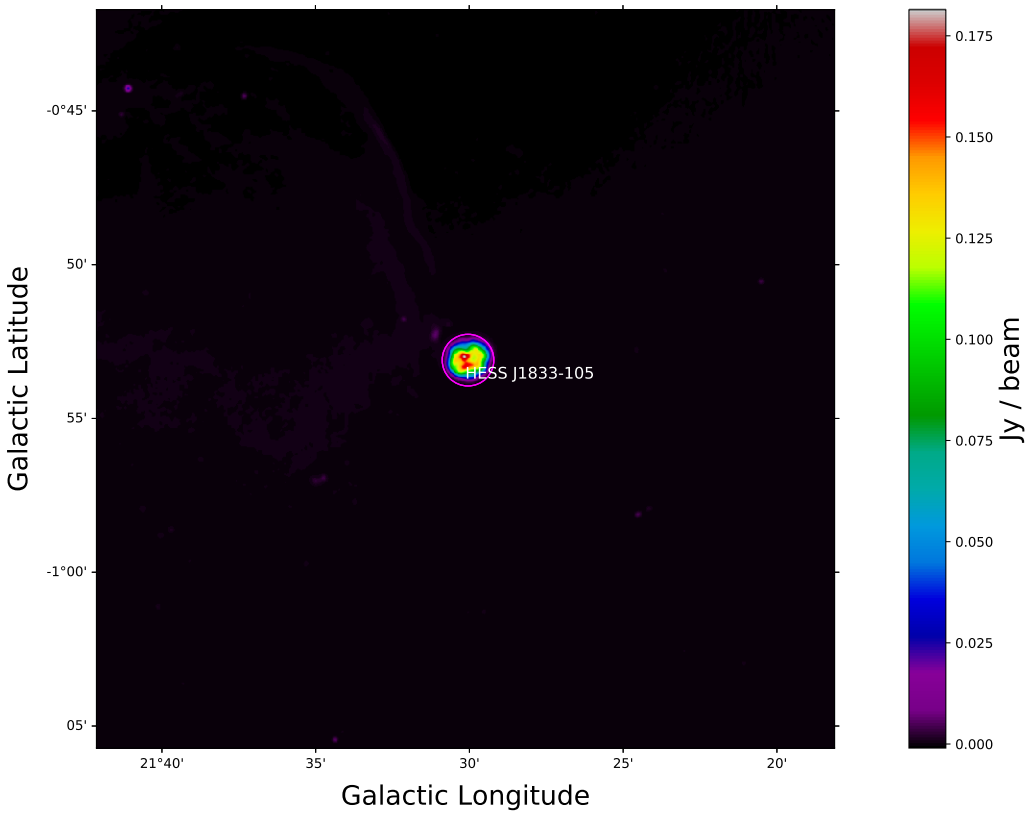

Figure 2.14: MeerKAT image of the region around HESS J1833-105. The pink circle is the region used for measuring the radio flux.

Table 2.3: Parameters of electron population that describes the combined synchrotron and inverse compton model for HESS J1843-033, HESS J1833-105 and HESS J1826-148. The electron energy is the total energy in electrons and B is the magnetic field.

Source	Normalisation $eV^{-1}\,s^{-1}\,cm^{-2}$	Spectral Index	B μG	Cutoff Energy TeV	electron energy $\left(\frac{d}{1\text{kpc}}\right)^2$ erg
HESS J1843-033	4.03×10^{33}	1.98	3.6	3.2	2.48×10^{46}
HESS J1833-105	2.09×10^{31}	2.1	23.6	9.5	6.3×10^{45}
HESS J1826-148	1.03×10^{33}	1.58	5.6	12.8	6.95×10^{45}

HESS J1826-148 has been seen in X-rays by XMM-Newton and Chandra[31]. The X-ray data in this work is again taken from the XMM-Newton pipeline. The X-ray emission and radio emission are consistent spatially. Again only the X-ray data with the largest energy bin is used for the fit of the radio,

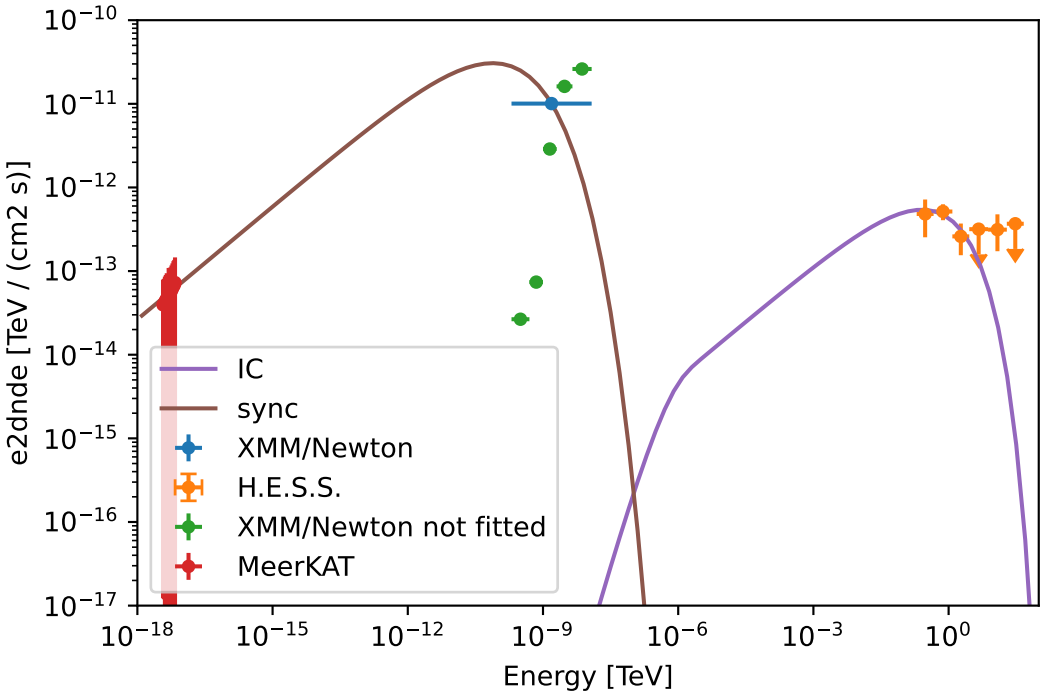

Figure 2.15: The combined synchrotron and inverse Compton model for HESS J1833-105. The brown line shows the synchrotron part of the model and the purple line shows the inverse Compton part of the model. The MeerKAT, XMM-Newton and HESS data is plotted. Only the the XMM-Newton data point with the largest energy bin is used in the fitting.

X-ray and gamma-ray data for HESS J1833-105. The parameters of the fit can be seen in Table 2.3. Fig. 2.17 shows the fit alongside the data points. The radio and gamma-ray data and the X-ray point with the largest energy bin are well fitted by the model, however the spectral index for the X-ray data is completely different to the combined model. This source is firmly identified as the binary LS 5039[3].

2.15 Discussion

Many of the unidentified H.E.S.S. sources looked at here have possible counterparts that could explain their emission, although none of them have been confirmed yet. There are three unidentified H.E.S.S. sources in the region of the MeerKAT survey which do not have any known sources nearby: HESS J1828-099, HESS J1503-582 and HESS J1708-410. For one source, HESS J1843-033, a combined synchrotron and inverse Compton fit was done which

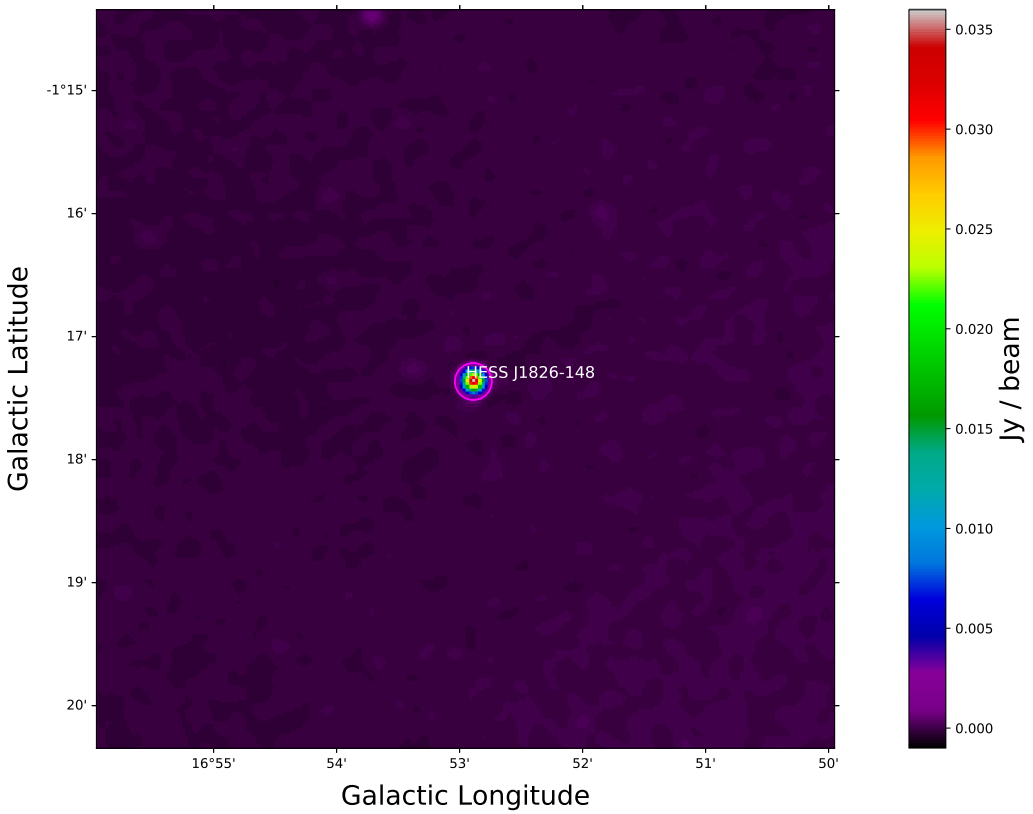

Figure 2.16: MeerKAT image of the region around HESS J1826-148. The pink circle is the region used for measuring the radio flux.

suggests that this source is leptonic in nature. More work in identifying what produces the radio emission needs to be done to see if any of it could also produce the TeV emission. There is some promising radio emission observed by MeerKAT which after further investigation may point to the nature of these unidentified sources. If MeerKAT surveys the rest of the galactic plane this could be done for more of the unidentified H.E.S.S. sources and hopefully some of them can be identified. For the two known sources, HESS J1833-105 and HESS J1826-148, the combined fit was able to model most of the data well however the spectral index for the X-ray data is different to the rest of the combined model for both sources. More investigations will be necessary to determine the reason for this. It is possible that a more complicated model for the electron spectrum could work, such as the two-zone model which would take two distinct electron populations.

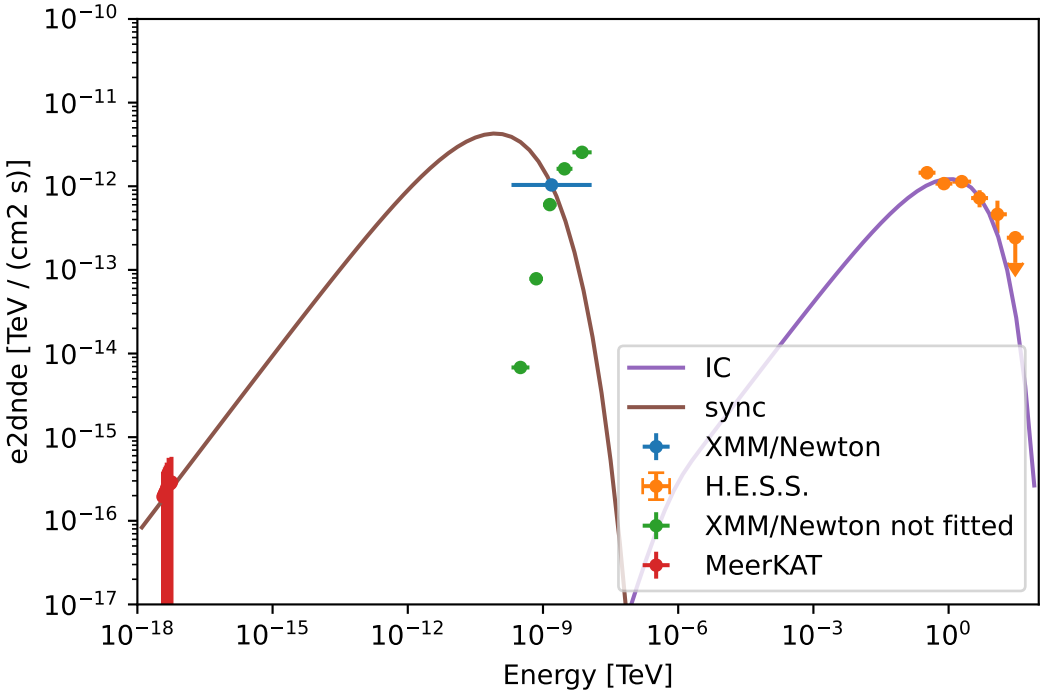

Figure 2.17: The combined synchrotron and inverse Compton model for HESS J1826-148. The brown line shows the synchrotron part of the model and the purple line shows the inverse Compton part of the model. The MeerKAT, XMM-Newton and HESS data is plotted. Only the the XMM-Newton data point with the largest energy bin is used in the fitting.

3: Neutrino prediction

3.1 Introduction

The HGPS has detected VHE emission from 78 sources of different object classes, some of which are unknown. It is not possible to determine the mechanism of gamma ray production (hadronic or leptonic) from the gamma-ray emission alone. The detection of neutrino emission would provide evidence for a hadronic scenario. In this section the neutrino output of these sources is predicted assuming all the gamma rays are of hadronic origin. This prediction is then turned into a map which is then compared to ANTARES neutrino data. The model presented here could be used to search for neutrino emission from individual gamma-ray sources as well as testing for neutrino emission from potential source populations in the Milky Way.

3.2 Method

3.2.1 Neutrino flux

The first step was to make a model for each of the sources in the H.E.S.S. Galactic Plane Survey. For sources that had already been identified as Pulsar Wind Nebula (PWN) no neutrino prediction was made as the emission is supposed to be leptonic. For all other sources the emission was assumed to be hadronic. In total 66 of the 78 H.E.S.S. sources were used. A parametrisation of the proton spectrum for each source is made using naima [17] and the model of Kelner et al [6] based on the gamma-ray radiation. This proton spectrum is then used to get a prediction of the neutrino flux. The naima Kelner model only does gamma-ray emission and is only used to fit the gamma-ray spectrum to determine the parametrisation of the proton spectrum. A new model was created to get the neutrino emission from the proton spectrum, this can be seen in Appendix B. If there is a Fermi [15] source nearby to the H.E.S.S. source, the combined H.E.S.S. and Fermi gamma-ray emission is used to make the fit unless the fit was significantly better by excluding the Fermi source and therefore highly unlikely that the Fermi source is a counterpart to the H.E.S.S. source. The fitting done with naima uses an affine-invariant ensemble sampler for Markov Chain Monte Carlo. Three parameters are used to define the proton spectrum: normalisation, spectral index and exponential cutoff energy. The equation for the proton distribution is:

$$\mathrm{J}_p(E_p) = A \left(\frac{E_p}{E_0}\right)^{-\alpha} \exp\left(-\frac{E_p}{E_{\mathrm{Cutoff}}}\right)^{\beta} \tag{3.1}$$

Where A is the normalisation, E_{Cutoff} is the cutoff energy, α is the spectral index, E_0 is the reference energy which is set to 1 TeV and β is the cutoff exponent which is set to 1.

Fig. 3.1 and Fig. 3.3 shows the gamma-ray emission of HESS J1640-465 and HESS J1713-397 respectively and gives examples of what happens in the fitting. The thick black line shows the line with the maximum log likelihood while the gray lines are the other samples. In this fit all the samples are quite close together and fit the data reasonably well. In Fig. 3.2 and Fig. 3.4 the predicted neutrino emission is plotted with the gamma-ray emission.

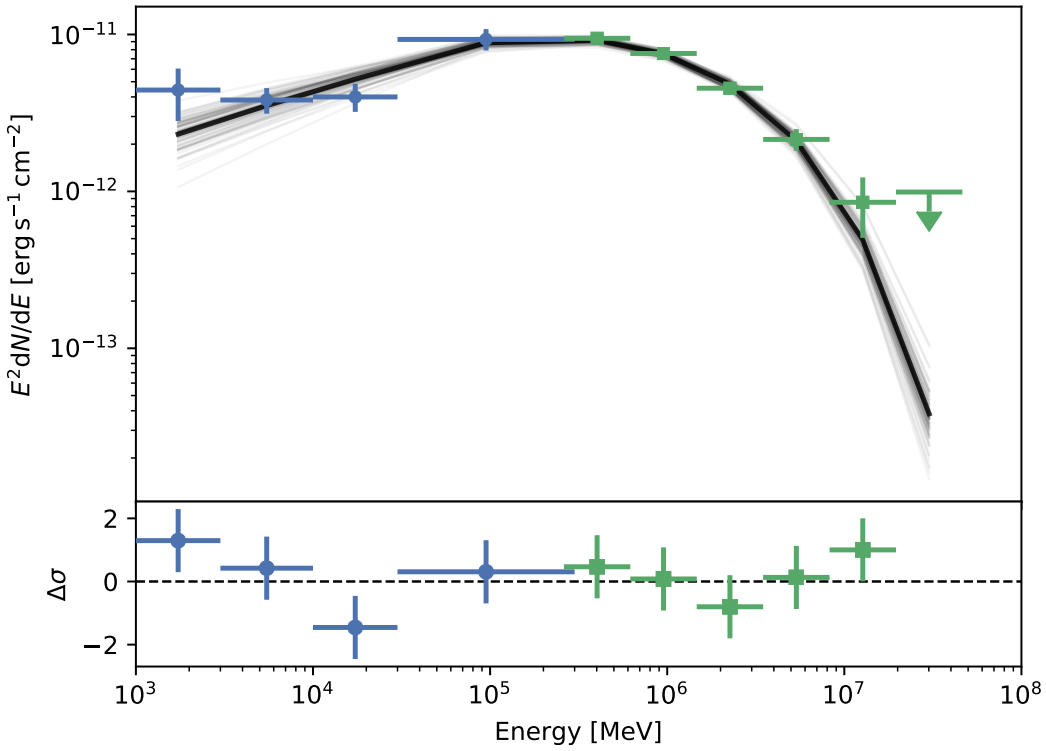

Figure 3.1: Samplers fit for HESS J1640-465. The blue points are for the Fermi source 4FGL J1640.6-4632 and the green points for HESS J1640-465. The dark black line is for the parameters with the maximum log likelihood value of the samplers. The χ^2 p-value is 0.34.

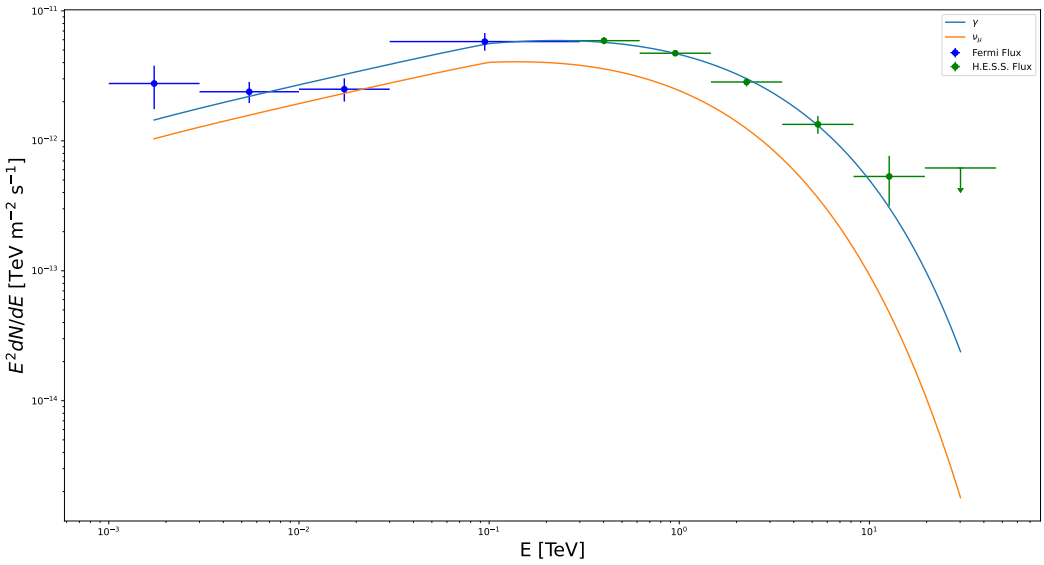

Figure 3.2: Gamma-ray emission and Neutrino emission plotted together for HESS J1640-465. The blue points are for the Fermi source 4FGL J1640.6-4632 and the green points for HESS J1640-465. The blue line is for the the gamma-ray emission and the orange line is for the neutrino emission.

3.2.2 Creating the map

To create the neutrino map, gammapy,[1] a community-developed core Python package for TeV gamma-ray astronomy [32, 33] is used. A blank map is made with the same dimensions as the H.E.S.S. Galactic Plane map with an added energy dimension, the energy axis ranges from 1 TeV to 100 TeV with 4 bins: 1 TeV to 3.2 TeV, 3.2 TeV to 10 TeV, 10 TeV to 31.6 TeV and 31.6 TeV to 100 TeV. A Sky Model is then created for each source, this has spatial and spectral parts. The spectral model is the muon neutrino part of our model based on [6]. The spatial model is created using the information from the HGPS results, each source is spatially modelled as either a point source, a shell model, a Gaussian or x-Gaussian (where the source is made up of multiple gaussian components). The map is then populated by taking the integral of the muon neutrino flux over each energy bin.

[1] https://www.gammapy.org

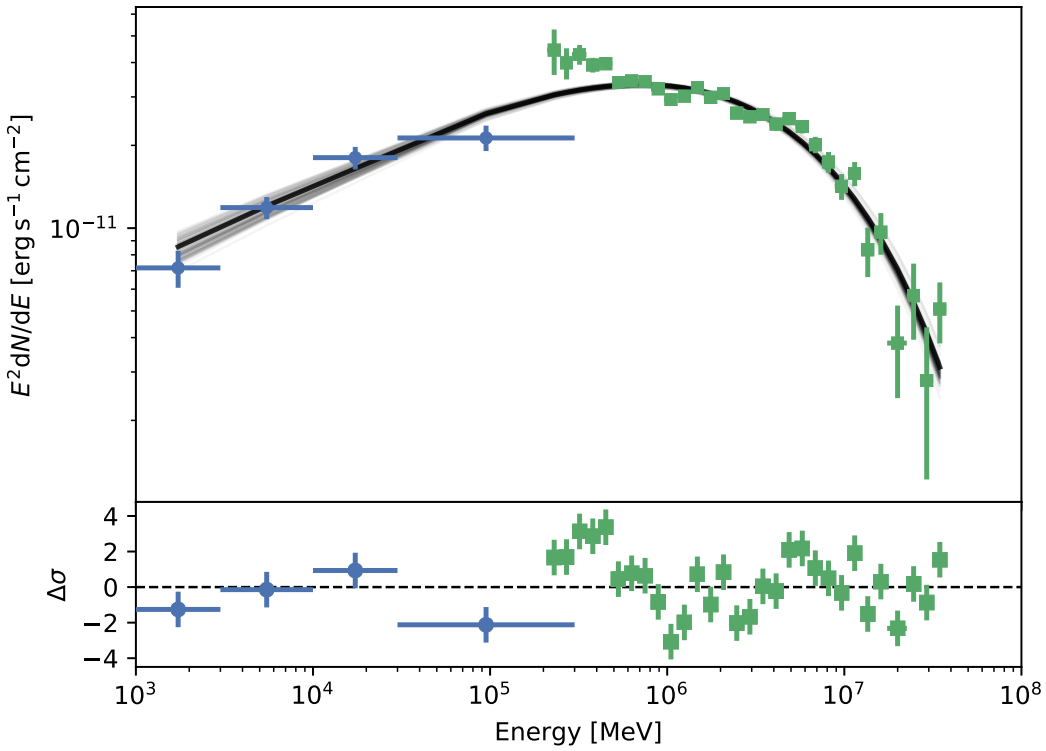

Figure 3.3: A plot of the samplers fit for HESS J1713-397. The blue points are for the Fermi source 4FGL J1713.5-3945e and the green points for HESS J1713-397. The dark black line is for the parameters with the maximum log likelihood value of the samplers. The χ^2 p-value is 4.2×10^{-8}.

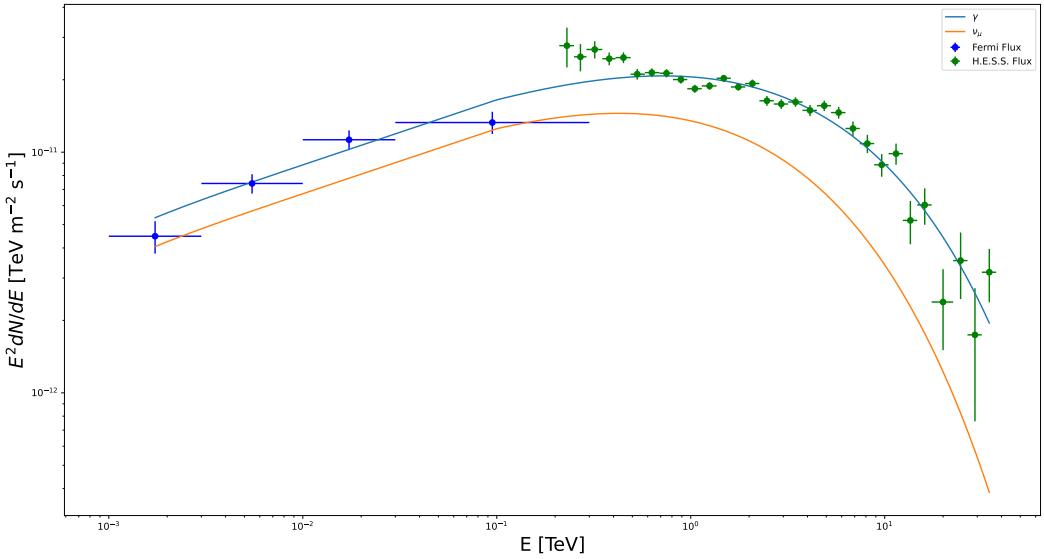

Figure 3.4: Gamma-ray emission and Neutrino emission plotted together for HESS J1713-397. The blue points are for the Fermi source 4FGL J1713.5-3945e and the green points for HESS J1713-397. The blue line is for the the gamma-ray emission and the orange line is for the neutrino emission.

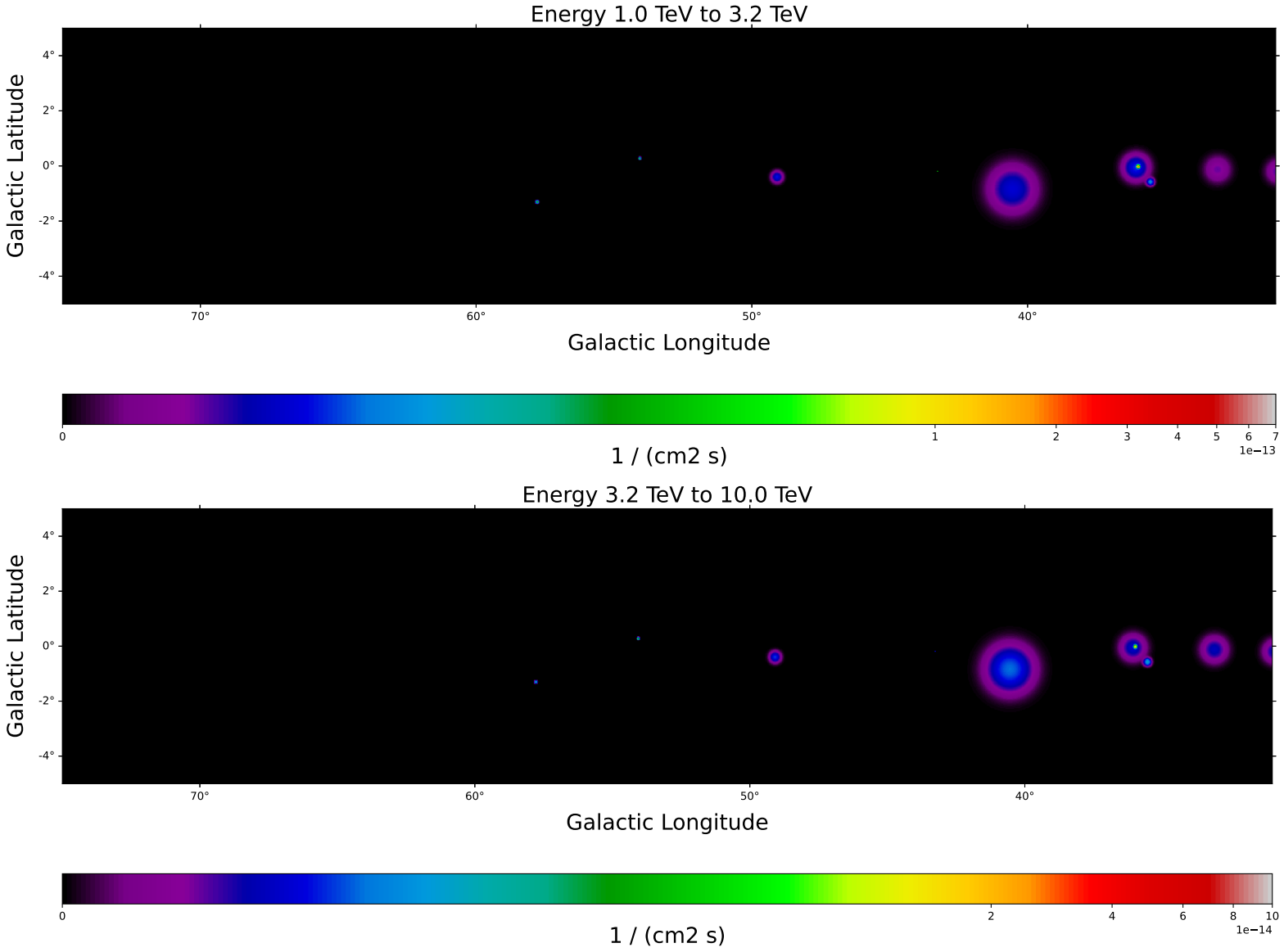

Figure 3.5: Predicted neutrino flux of the Milky Way per energy bin from galactic longitude 75° to 31°.

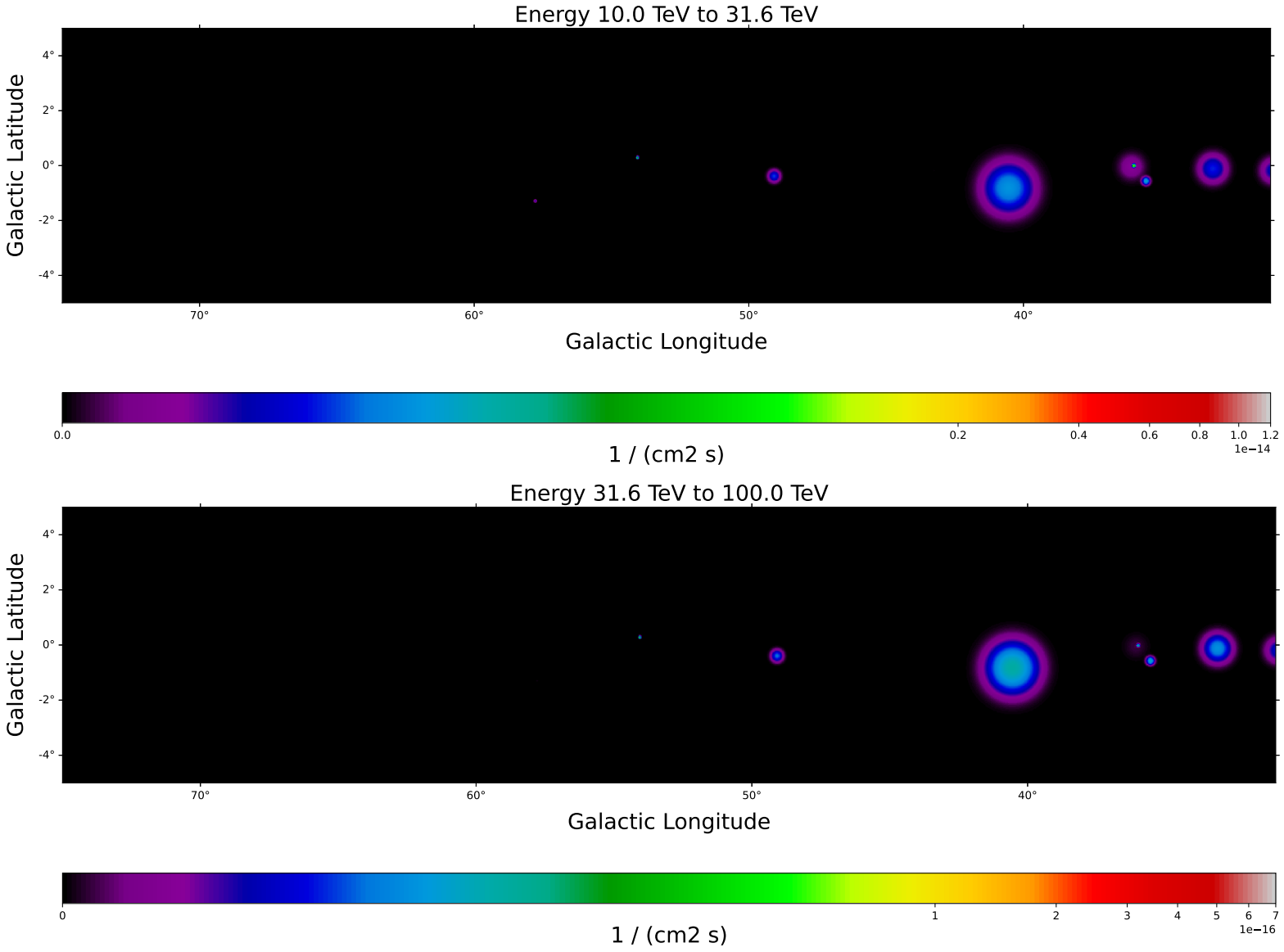

Figure 3.6: Predicted neutrino flux of the Milky Way per energy bin from galactic longitude 75° to 31°.

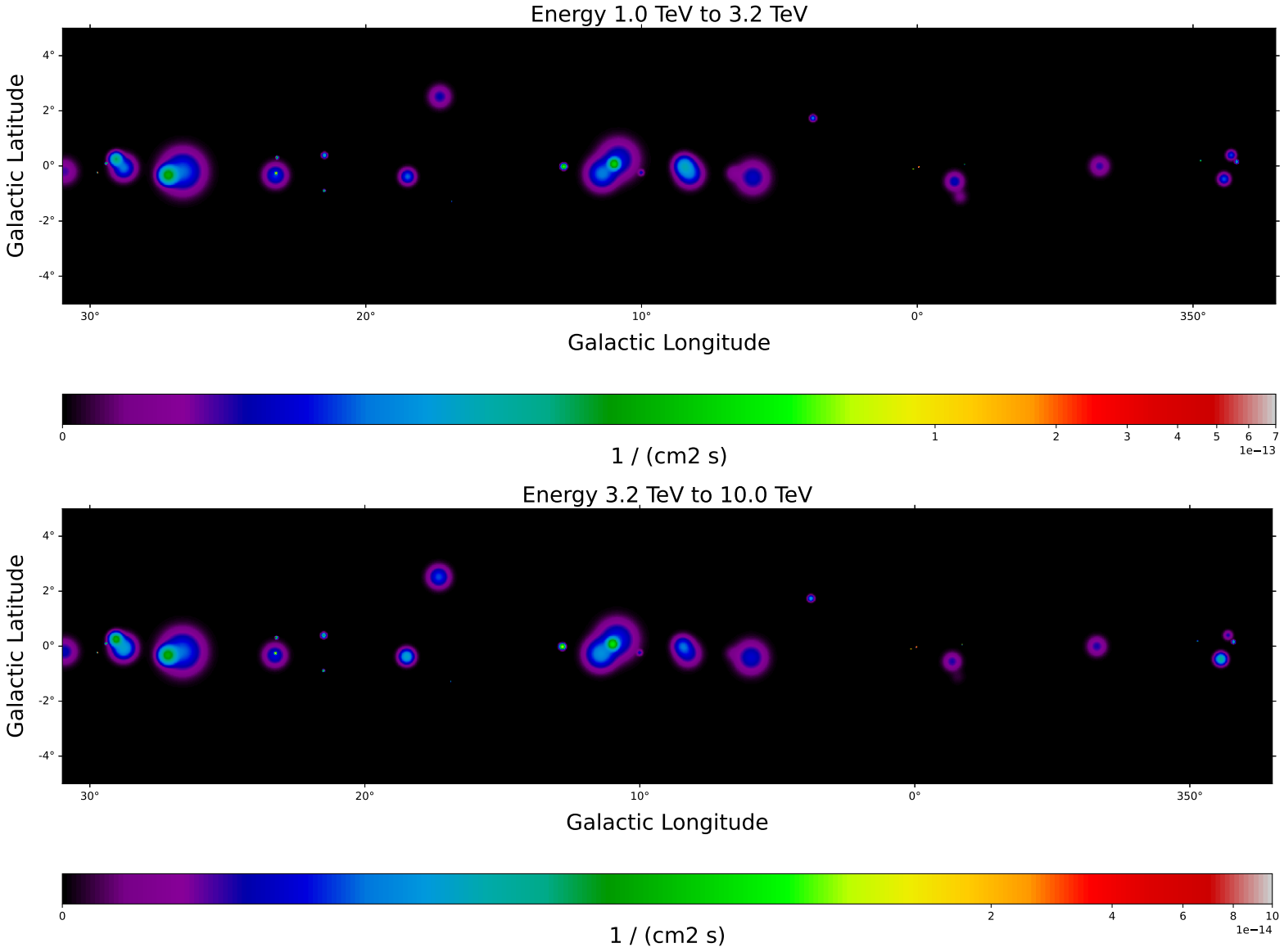

Figure 3.7: Predicted neutrino flux of the Milky Way per energy bin from galactic longitude 31° to 347°.

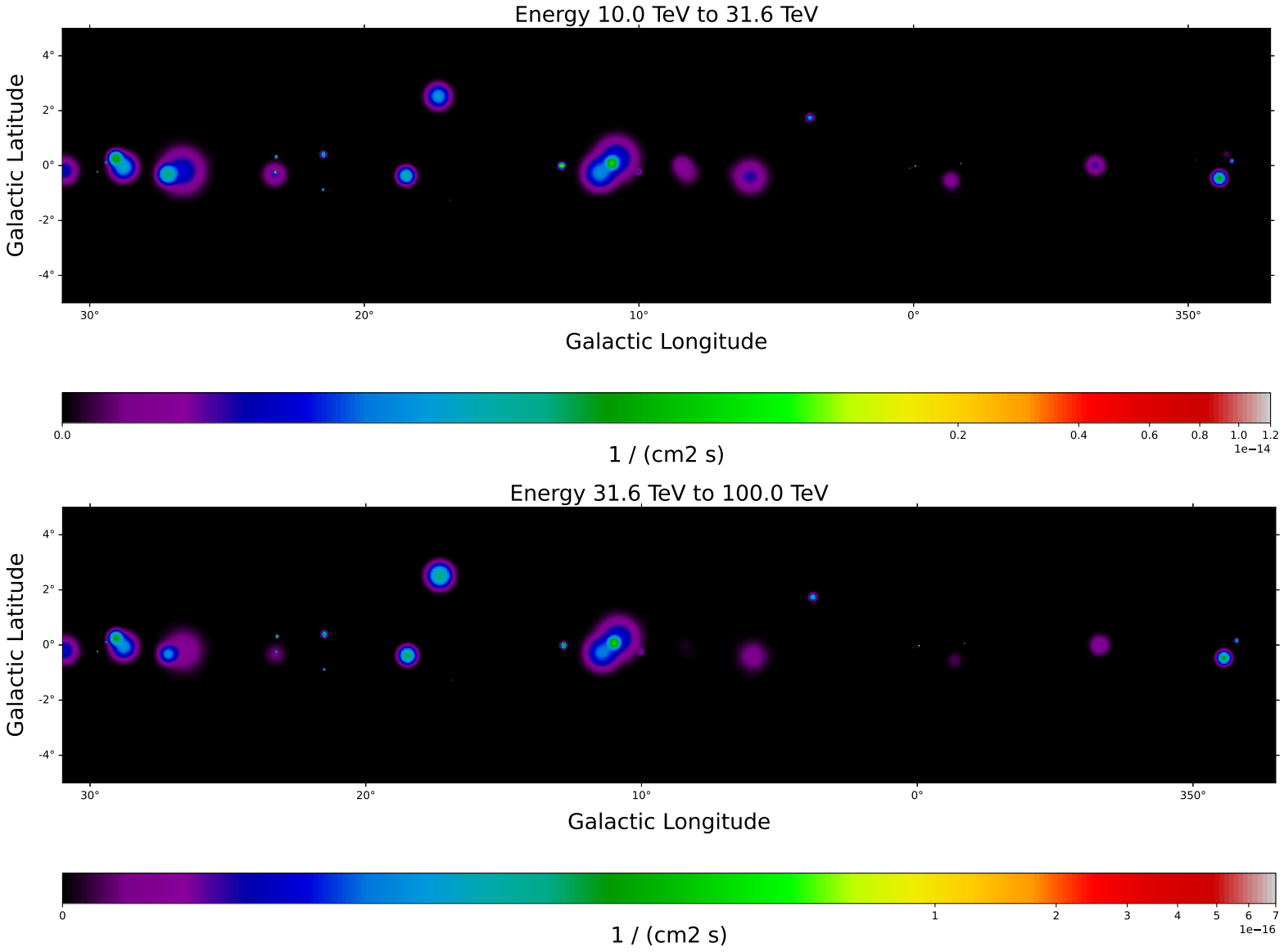

Figure 3.8: Predicted neutrino flux of the Milky Way per energy bin from galactic longitude 31° to 347°.

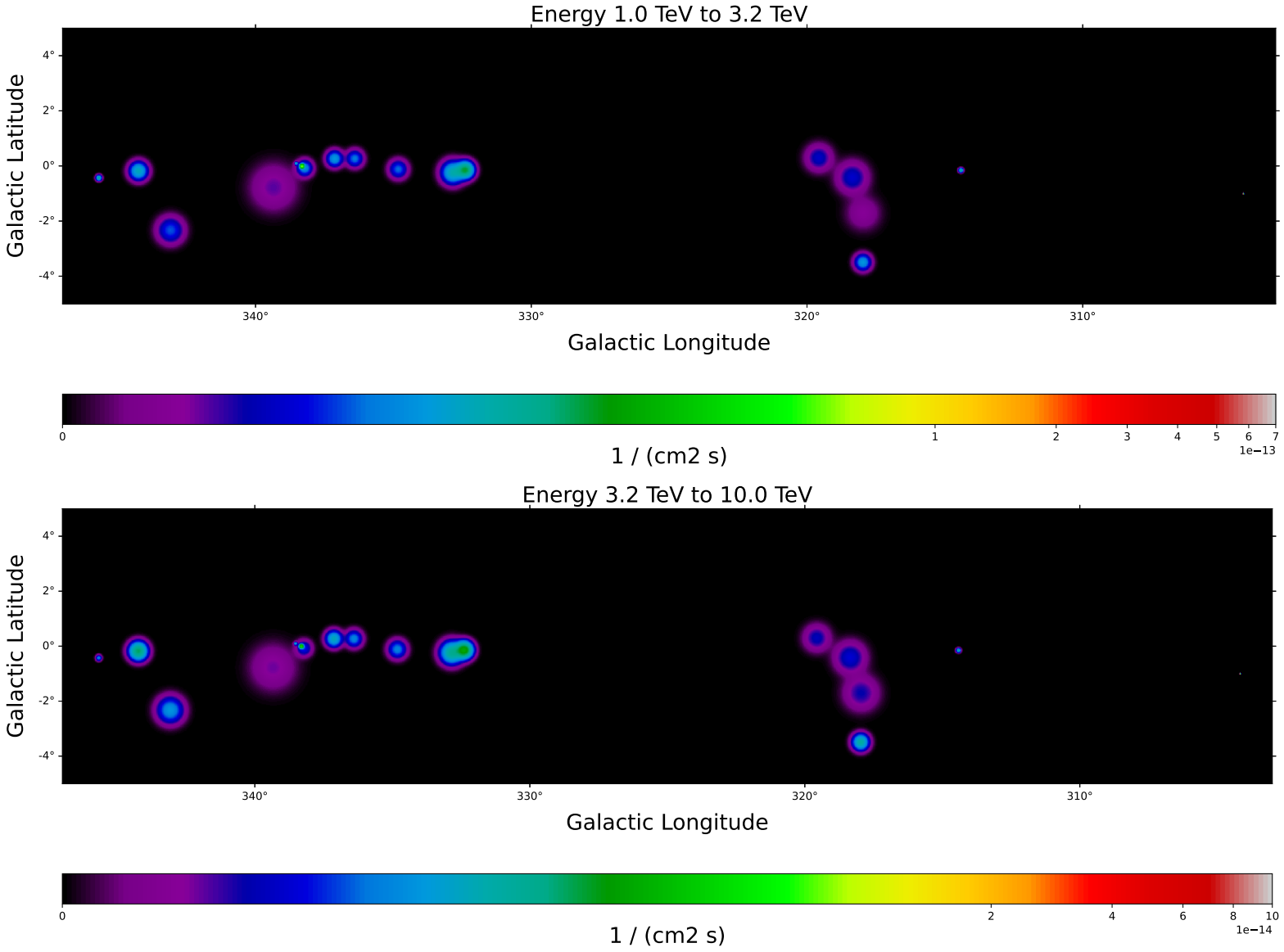

Figure 3.9: Predicted neutrino flux of the Milky Way per energy bin from galactic longitude 347° to 303°.

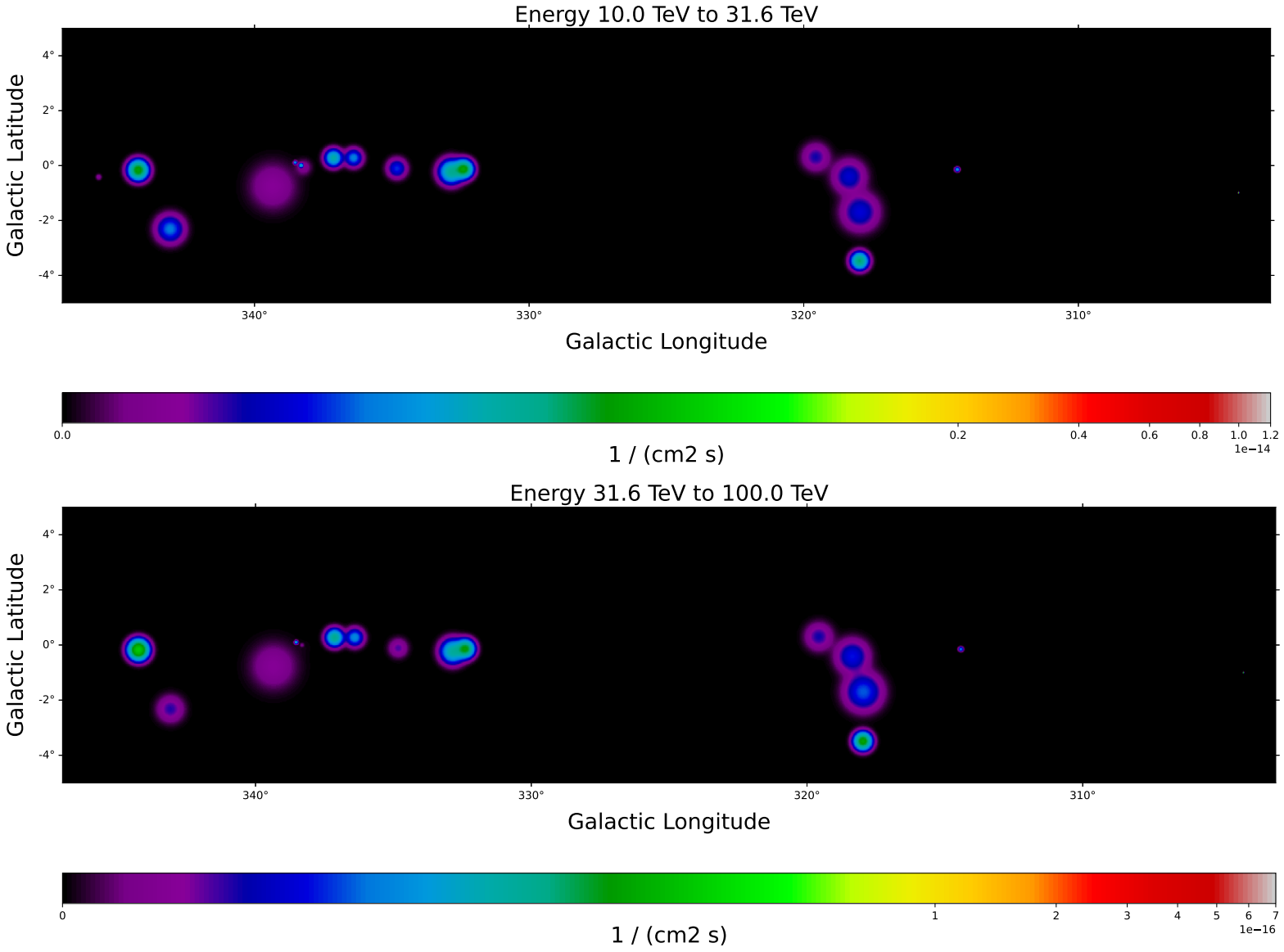

Figure 3.10: Predicted neutrino flux of the Milky Way per energy bin from galactic longitude 347° to 303°.

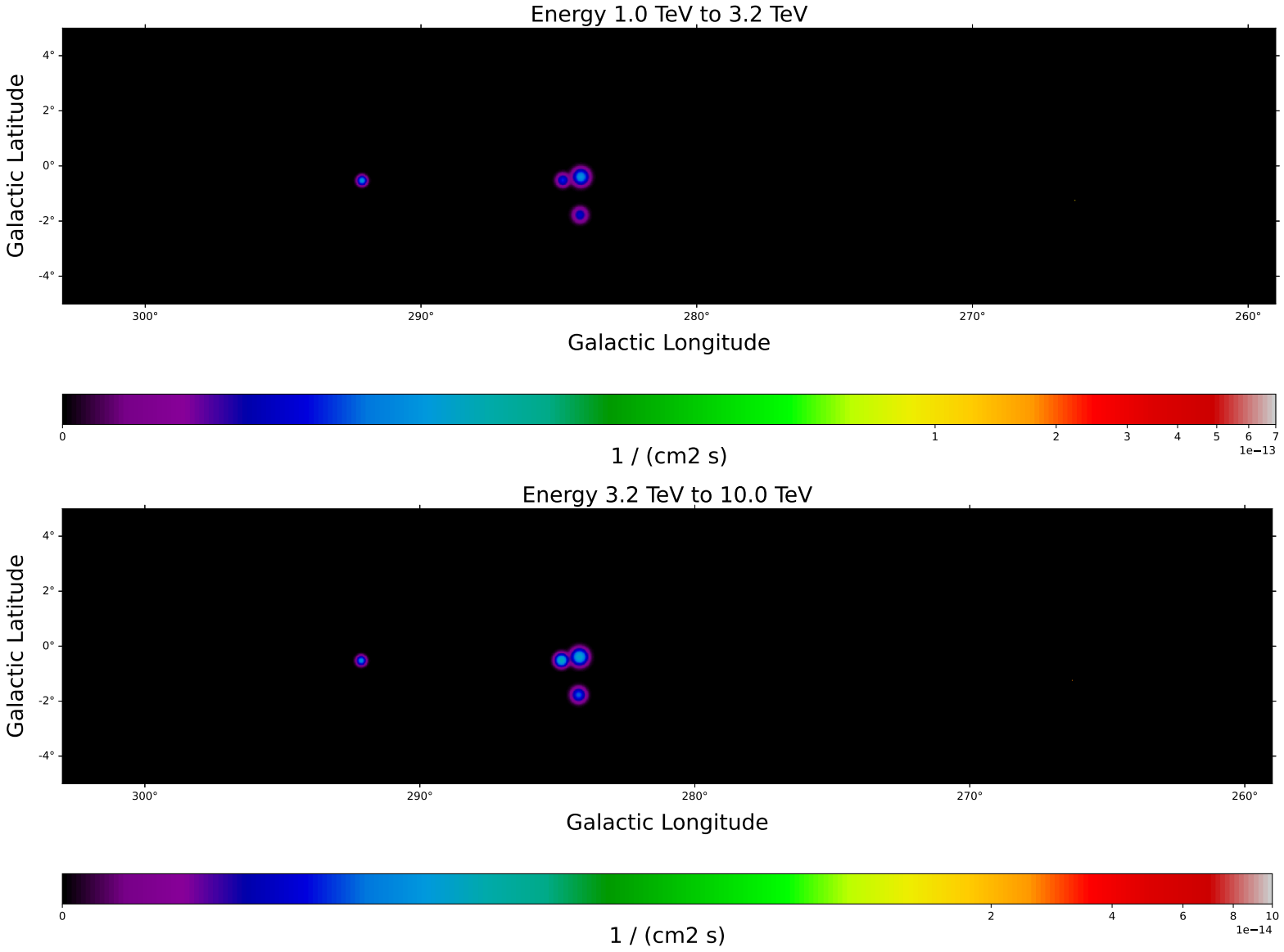

Figure 3.11: Predicted neutrino flux of the Milky Way per energy bin from galactic longitude 303° to 259°.

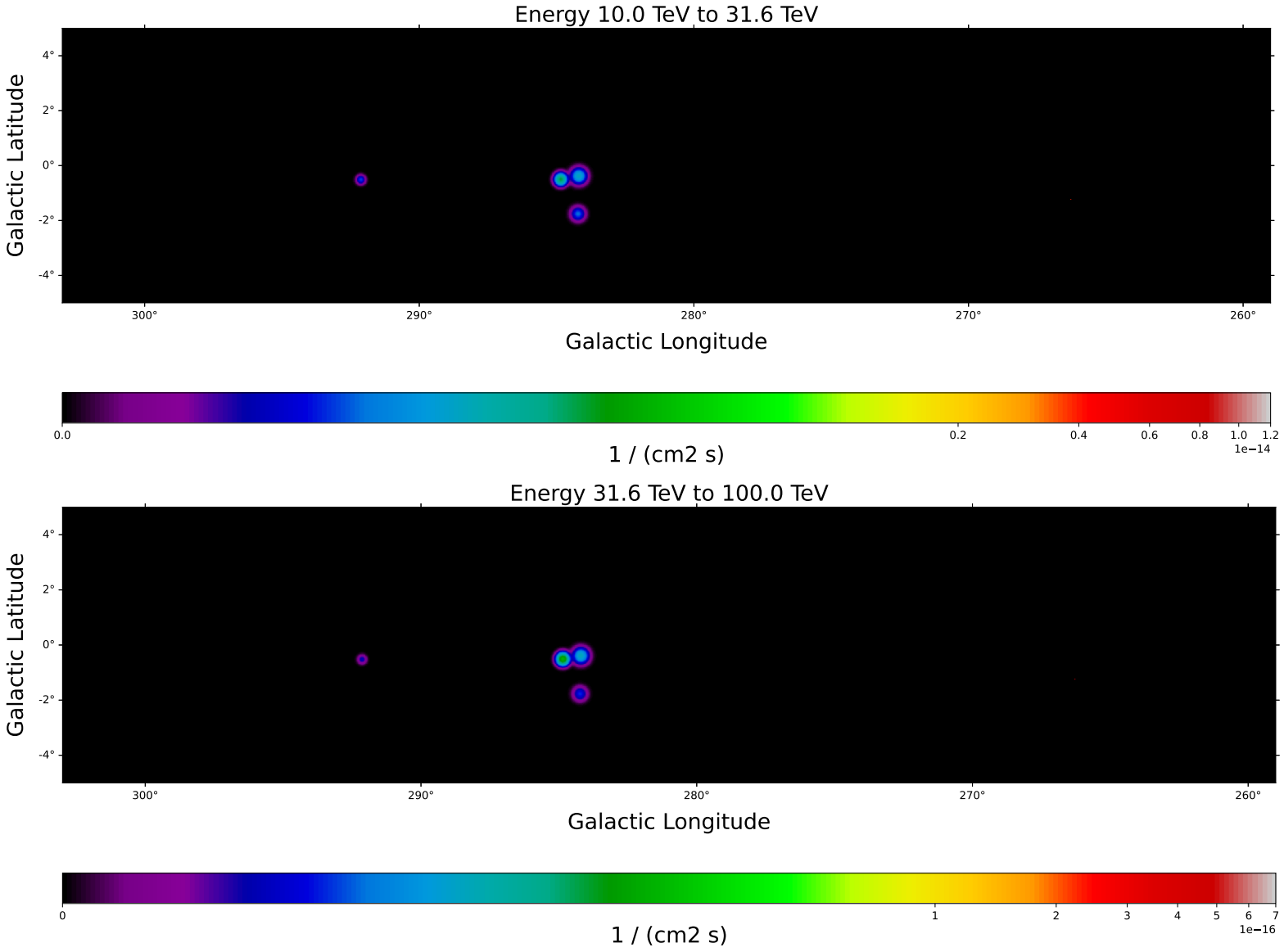

Figure 3.12: Predicted neutrino flux of the Milky Way per energy bin from galactic longitude 303° to 259°.

3.3 ANTARES neutrino point sources

ANTARES searched for muon neutrino point sources between 2007 and 2017[7, 10]. In the region of the predicted neutrino map there are 570 muon neutrino candidates detected by ANTARES. In Figures 3.14 and 3.15 all 570 neutrino candidates are plotted on the first energy bin of the predicted neutrino map. The neutrino candidate is considered to overlap with the neutrino emission if any part of the neutrino's position region has a predicted neutrino flux of at least 10^{-17} cm^{-2} s^{-1}. 56 of the ANTARES neutrino candidates overlap with the predicted neutrino emission. In Figures 3.16 and 3.17 only the 56 muon neutrino candidates that overlap with the predicted neutrino emission have been plotted over the predicted neutrino emission. Most of the predicted neutrino emission from the H.E.S.S. sources do not have counterparts detected by ANTARES.

To test the significance of these 56 positional associations a null model was created where the positions of the 570 neutrino candidates were randomised to any location in the predicted map region. This was done by re-drawing the possible neutrino event to a randomised right ascension and a randomised declination, the size of the estimated angular resolution of the neutrino events was kept the same. 1000 such re-positioning of the events was done. A search for associations with the predicted neutrino emission with each set of re-positioned events was done. The mean number of associations from the re-positioned events is 47.355 and the median number of associations from the re-positioned events is 47. The most common number of associations from the re-positioned events was 48 which occured 61 times. There were 115 sets of re-positioned events with 56 or more associations. A histogram of the associations of re-positioned events can be seen in Figs. 3.13. Based on this the 56 associations would occur randomly 11.5% of the time, therefore there is an 88.5% chance that this is not a random coincidence. Therefore there is no significant correlation between the ANTARES neutrino candidates and the predicted neutrino emissions.

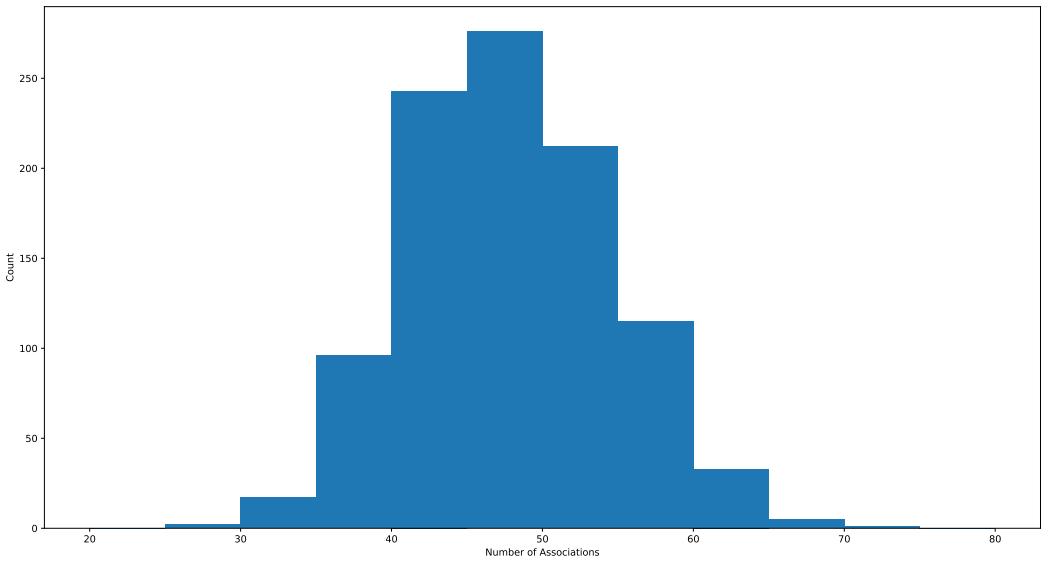

Figure 3.13: Histogram of the number of associations for the randomised neutrino data.

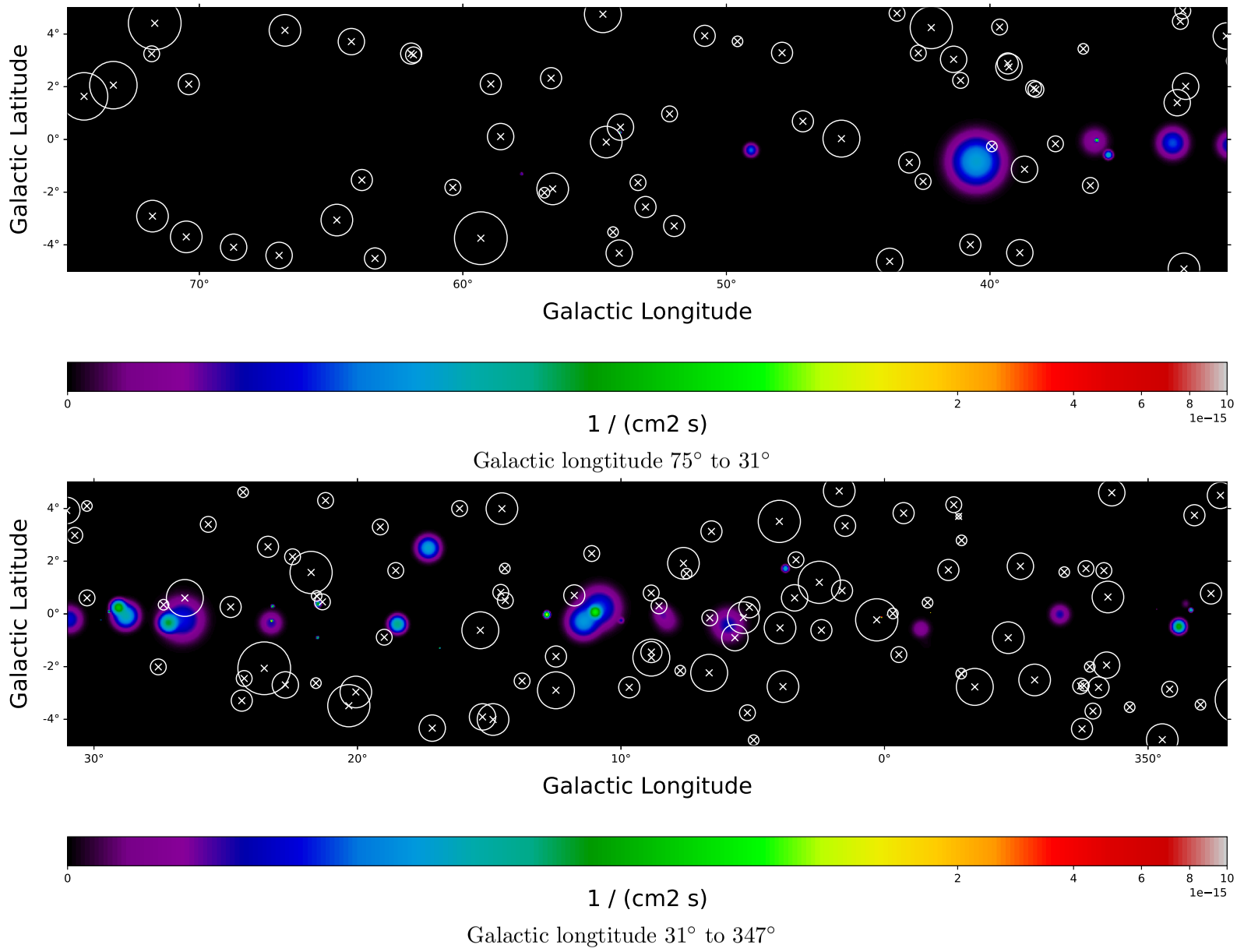

Figure 3.14: Predicted Neutrino map from galactic longitude 75° to 347° overlaid with the neutrinos from the 2007-2017 ANTARES search for cosmic neutrino point sources.

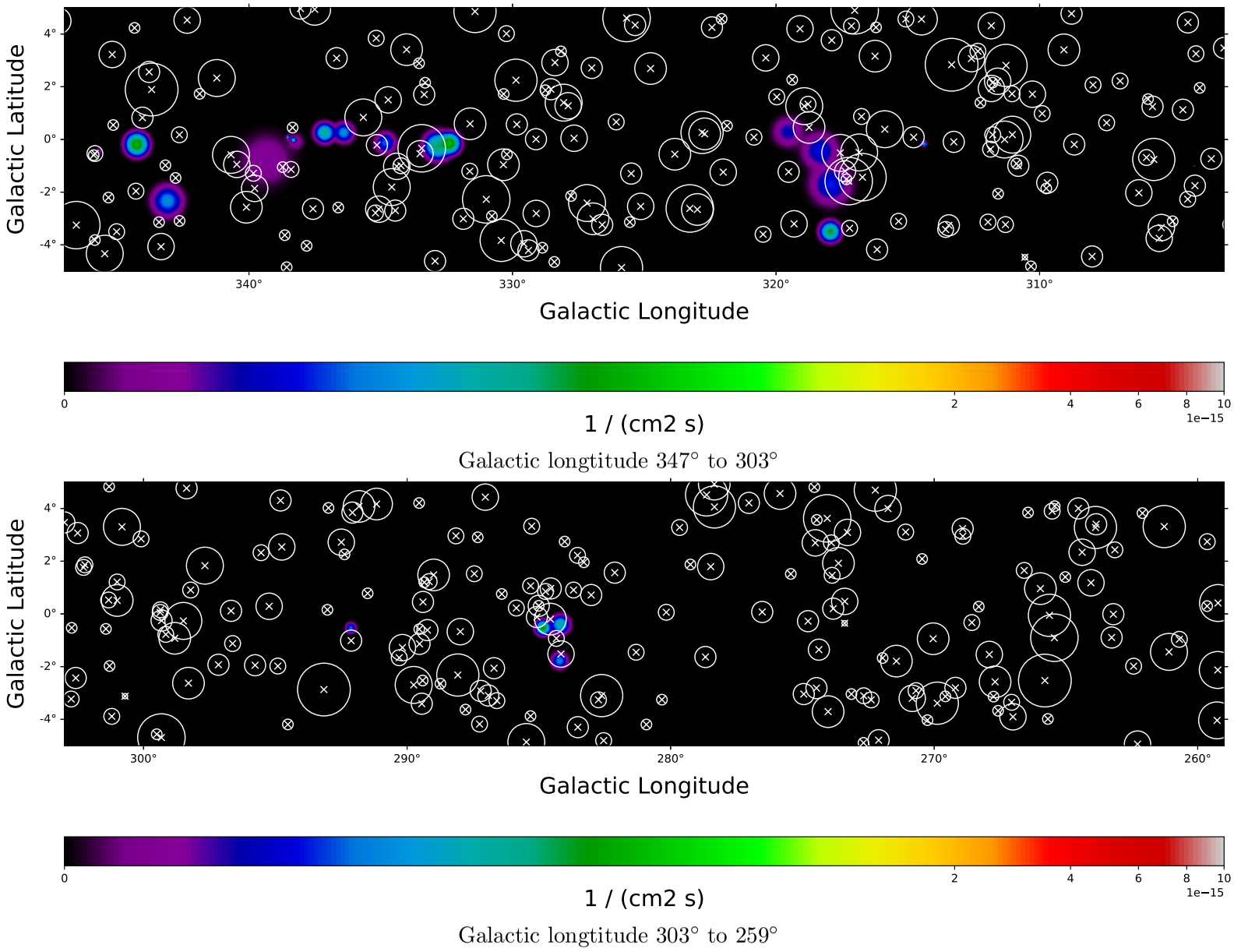

Figure 3.15: Predicted Neutrino map from galactic longitude 347° to 259° overlaid with the neutrinos from the 2007-2017 ANTARES search for cosmic neutrino point sources.

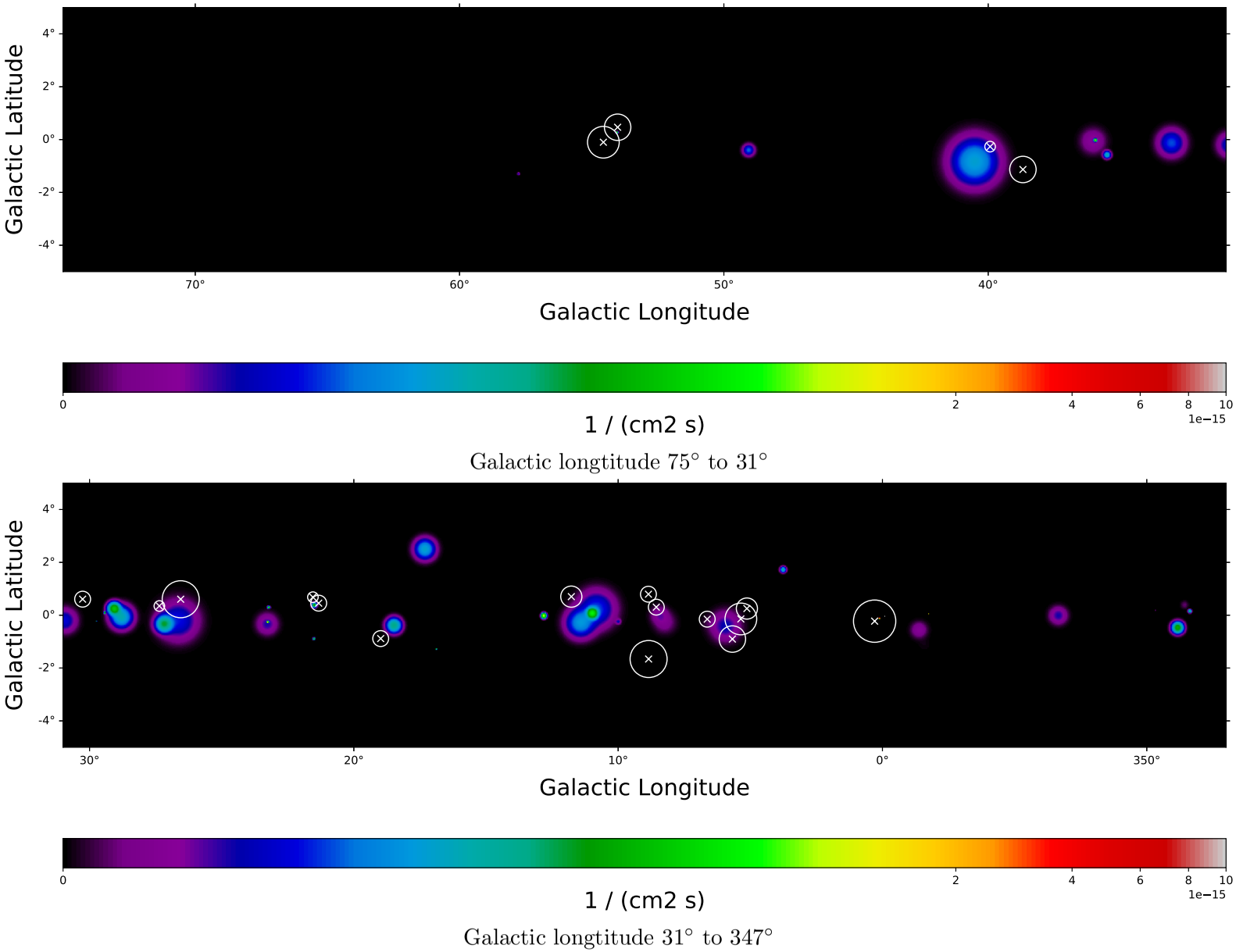

Figure 3.16: Predicted Neutrino map from galactic longitude 75° to 347° overlaid with the neutrinos from the 2007-2017 ANTARES search for cosmic neutrino point sources that overlap with the regions of the predicted neutrino emission.

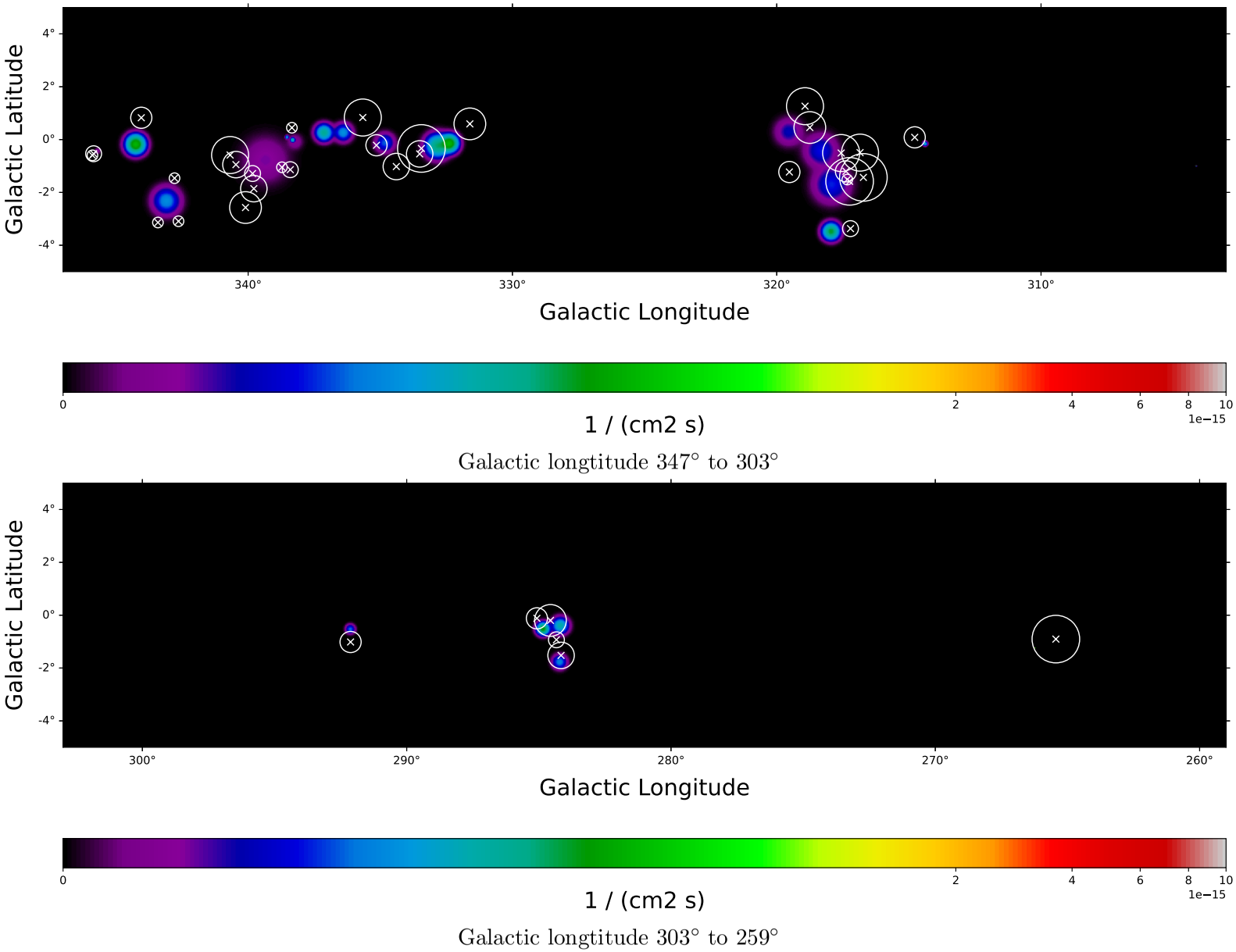

Figure 3.17: Predicted Neutrino map from galactic longitude 347° to 259° overlaid with the neutrinos from the 2007-2017 ANTARES search for cosmic neutrino point sources that overlap with the regions of the predicted neutrino emission.

3.4 Discussion

Table 3.1 lists the best-fit parameters for the proton spectra, the predicted muon neutrino flux and the χ^2 p-value of the fit for each source. The maximum neutrino flux over the energy range 1 TeV to 100 TeV is 2.98×10^{-11} TeV s^{-1} cm^{-2} for HESS J0852-463. The χ^2 p-values are calculated using the log likelihood values determined during the fitting with naima, the log likelihood is related to χ^2 by χ^2 = -2 ln$\mathcal{L}$. The worst χ^2 p-value is 4.2×10^{-8} for HESS J1713-397, the mean is 0.342 and the maximum is 0.962 for source HESS J1841-055. Fig. 3.3 shows the plot of the samplers for HESS J1713-397. It has a low χ^2 p-value because very few of the data points lie on the best fit line but instead lie just above or just below. Fitting only HESS J1713-397 does improve the fit but it would still be the worst fit of our sources with a χ^2 p-value of 1.3×10^{-5}. The other sampler fits can be seen in Appendix A.

The predicted neutrino emission map of the Milky Way can be seen in Figs. 3.5 - 3.12. The map is split into the four energy bins: 1 TeV to 3.2 TeV, 3.2 TeV to 10 TeV, 10 TeV to 31.6 TeV and 31.6 TeV to 100 TeV. In total 66 sources are plotted but 9 cannot be seen because their integrated neutrino fluxes are too small to fit into the scale of the map shown here. The map is produced using only observations and does not make use of the source class, distance to the source or the ambient target material.

Comparing the ANTARES neutrino point sources to the predicted neutrino map showed that the prediction is not significant with regards to the ANTARES neutrinos. This could be improved if some of the H.E.S.S. sources are found to be leptonic and then removed from the predicted neutrino map. To further test the map data from KM3Net could be tested against the predicted neutrino emission both in direction and energy.

3.5 Conclusion

The proton population was parametrised and a prediction of the neutrino flux for 66 sources in the H.E.S.S. Galactic Plane survey was made. Of the 66 sources we fitted, 19 included data from a 4FGL[15] source. The neutrino emission at higher energies strongly depends on the cutoff of the proton spectrum. The cutoff is constrained by the gamma-ray spectrum for some but not all of the sources. The neutrino emission of the sources without

constrained cutoff is certainly overestimated. This model can be used as a template to fit to neutrino observational data and to test for neutrino emission from known gamma-ray sources. Neutrino emission from the Milky Way can also arise from interactions of the sea of Cosmic Rays with the interstellar material. Diffuse gamma-ray emission detected by H.E.S.S. [34] and the Tibet Air Shower Array [35] can be used to predict diffuse neutrino emission but is not considered in this work.

Table 3.1: Table of fitted parameters for the proton spectra. The Neutrino flux in the energy range 1 TeV to 100 TeV. The reference energy for normalisation is 1 TeV.

Source Name	**normalisation** $\mathrm{TeV}^{-1}\,\mathrm{s}^{-1}\,\mathrm{cm}^{-2}$	**Spectral Index**	**Cutoff** TeV	**Neutrino flux** $\mathrm{s}^{-1}\,\mathrm{cm}^{-2}$	χ^2 **p-value**
HESS J0852-463	$(2.40\pm0.7)\times10^{48}$	0.897±0.12	21.11±2.6	$(2.98\pm1.7)\times10^{-11}$	0.887
HESS J1018-589 A	$(5.67\pm5.5)\times10^{46}$	1.623±0.23	118.27±29.2	$(4.22\pm6.3)\times10^{-13}$	0.276
HESS J1018-589 B	$(8.31\pm8.3)\times10^{46}$	1.298±0.32	68.89±20.3	$(1.37\pm2.7)\times10^{-12}$	0.922
HESS J1023-575	$(2.65\pm0.3)\times10^{48}$	2.083±0.03	156.41±20.4	$(3.64\pm0.6)\times10^{-12}$	0.023
HESS J1026-582	$(6.64\pm8.8)\times10^{44}$	0.207±0.28	85.92±47.4	$(2.24\pm5.6)\times10^{-12}$	0.078
HESS J1119-614	$(2.84\pm1.1)\times10^{48}$	2.376±0.17	93.46±34.5	$(1.02\pm0.8)\times10^{-12}$	0.142
HESS J1302-638	$(2.34\pm1.3)\times10^{48}$	2.740±0.19	473.77±130.1	$(3.81\pm3.6)\times10^{-13}$	0.003
HESS J1427-608	$(2.64\pm55.7)\times10^{48}$	2.617±0.97	151.29±60.3	$(5.09\pm0.02)\times10^{-13}$	0.720
HESS J1442-624	$(1.53\pm0.2)\times10^{48}$	1.554±0.06	22.66±2.4	$(2.40\pm0.7)\times10^{-12}$	0.068
HESS J1457-593	$(1.55\pm1.0)\times10^{49}$	2.519±0.25	305.38±62.8	$(5.15\pm1.1)\times10^{-12}$	0.232
HESS J1458-608	$(2.47\pm55.7)\times10^{47}$	1.521±1.01	159.98±90.0	$(3.75\pm306.1)\times10^{-12}$	0.034
HESS J1503-582	$(1.75\pm26.2)\times10^{49}$	2.680±0.37	274.15±74.5	$(3.19\pm59.2)\times10^{-12}$	0.072
HESS J1507-622	$(1.37\pm0.1)\times10^{48}$	1.876±0.03	218.01±43.0	$(5.40\pm1.1)\times10^{-12}$	0.905
HESS J1534-571	$(8.94\pm4.0)\times10^{47}$	1.633±0.22	53.57±21.8	$(2.99\pm3.4)\times10^{-12}$	0.146
HESS J1614-518	$(5.43\pm0.4)\times10^{48}$	1.843±0.02	48.75±11.8	$(7.78\pm1.8)\times10^{-12}$	0.158
HESS J1616-508	$(7.84\pm1.9)\times10^{48}$	2.030±0.08	126.53±5.2	$(1.17\pm0.5)\times10^{-11}$	0.037
HESS J1626-490	$(4.60\pm36.1)\times10^{48}$	2.330±0.46	358.46±122.8	$(3.34\pm0.5)\times10^{-12}$	0.495
HESS J1632-478	$(6.80\pm0.3)\times10^{48}$	2.416±0.01	230.45±19.2	$(3.06\pm0.2)\times10^{-12}$	0.166
HESS J1634-472	$(4.77\pm1.0)\times10^{48}$	2.277±0.08	477.42±113.3	$(4.69\pm1.8)\times10^{-12}$	0.043
HESS J1640-465	$(3.89\pm0.3)\times10^{48}$	1.696±0.04	15.69±1.1	$(2.37\pm0.4)\times10^{-12}$	0.430
HESS J1641-463	$(7.49\pm0.6)\times10^{47}$	2.569±0.02	321.17±34.3	$(2.1\pm0.2)\times10^{-13}$	0.036
HESS J1646-458	$(2.74\pm38.2)\times10^{49}$	2.643±0.40	239.32±43.3	$(5.50\pm1.0)\times10^{-12}$	0.368
HESS J1702-420	$(2.35\pm10.1)\times10^{48}$	1.916±0.5	336.01±89.0	$(9.82\pm0.7)\times10^{-12}$	0.074
HESS J1708-410	$(4.43\pm2.2)\times10^{47}$	1.131±0.27	9.85±2.7	$(6.12\pm6.9))\times10^{-13}$	0.641
HESS J1708-443	$(3.67\pm2.0)\times10^{46}$	0.301±0.13	27.28±7.2	$(6.93\pm6.6)\times10^{-12}$	0.129
HESS J1713-381	$(1.61\pm0.2)\times10^{48}$	1.956±0.0.05	14.51±1.8	$(4.22\pm1.0)\times10^{-13}$	0.407
HESS J1713-397	$(9.49\pm0.3)\times10^{48}$	1.768±0.02	63.74±3.2	$(2.28\pm0.2)\times10^{-11}$	4.2×10^{-8}
HESS J1714-385	$(6.37\pm2.1)\times10^{47}$	2.452±0.11	352.44±91.4	$(2.84\pm1.6)\times10^{-13}$	0.340
HESS J1718-374	$(1.17\pm0.2)\times10^{48}$	2.440±0.03	10.92±41.0	$(6.26\pm11.4)\times10^{-14}$	0.053
HESS J1718-385	$(1.07\pm3.4)\times10^{37}$	-4.596±0.75	20.53±3.7	$(2.15\pm27.7)\times10^{-12}$	0.281
HESS J1729-345	$(1.88\pm34.1)\times10^{48}$	2.314±1.71	142.51±53.7	$(1.02\pm337.7)\times10^{-12}$	0.312
HESS J1731-347	$(2.14\pm0.5)\times10^{48}$	1.963±0.10	44.24±10.2	$(1.86\pm0.8)\times10^{-12}$	0.894
HESS J1741-302	$(2.50\pm3.8)\times10^{47}$	2.250±0.52	440.43±88.6	$(2.68\pm13.6)\times10^{-13}$	0.581
HESS J1745-290	$(2.54\pm0.1)\times10^{48}$	2.159±0.03	109.91±5.7	$(2.14\pm0.2)\times10^{-12}$	0.376
HESS J1745-303	$(3.87\pm0.2)\times10^{48}$	2.371±0.01	56.57±7.6	$(1.06\pm0.1)\times10^{-12}$	0.025
HESS J1746-285	$(4.12\pm12.2)\times10^{46}$	1.702±0.76	287.30±68.0	$(4.26\pm60.6)\times10^{-13}$	0.312
HESS J1746-308	$(7.89\pm2.0)\times10^{48}$	3.373±0.33	84.35±24.6	$(1.42\pm1.4)\times10^{-13}$	0.413
HESS J1747-248	$(4.15\pm83.8)\times10^{47}$	2.232±0.61	339.88±82.5	$(4.42\pm142.0)\times10^{-13}$	0.164
HESS J1800-240	$(8.63\pm70.2)\times10^{48}$	2.455±0.21	365.66±130.1	$(3.84\pm30.9)\times10^{-12}$	0.639
HESS J1801-233	$(3.04\pm0.2)\times10^{48}$	2.643±0.02	30.20±18.2	$(2.48\pm1.0)\times10^{-13}$	0.428
HESS J1804-216	$(2.37\pm0.5)\times10^{49}$	2.342±0.16	25.92±60.7	$(3.97\pm4.7)\times10^{-12}$	0.014

Continued on next page

Table 3.1 – continued from previous page

Source Name	**normalisation** $\mathrm{TeV}^{-1}\,\mathrm{s}^{-1}\,\mathrm{cm}^{-2}$	**Spectral Index**	**Cutoff** TeV	**Neutrino flux** $\mathrm{s}^{-1}\,\mathrm{cm}^{-2}$	χ^2 **p-value**
HESS J1808-204	$(1.73\pm4.8)\times10^{47}$	2.091±0.57	410.02±141.2	$(3.61\pm24.7))\times10^{-13}$	0.028
HESS J1809-193	$(7.40\pm2.0)\times10^{48}$	2.107±0.10	128.01±35.2	$(8.27\pm3.9)\times10^{-12}$	0.186
HESS J1813-126	$(2.91\pm0.6)\times10^{47}$	1.737±0.49	318.53±79.9	$(2.72\pm12.9)\times10^{-12}$	0.941
HESS J1813-178	$(2.23\pm0.7)\times10^{47}$	1.178±0.11	45.58±18.3	$(3.44\pm2.7)\times10^{-12}$	0.141
HESS J1826-130	$(2.49\pm1.8)\times10^{47}$	1.579±0.22	155.57±63.1	$(2.85\pm3.9)\times10^{-12}$	0.198
HESS J1826-148	$(9.55\pm3.1)\times10^{47}$	2.066±0.15	146.50±49.5	$(1.35\pm1.0)\times10^{-12}$	0.398
HESS J1828-099	$(3.20\pm55.0)\times10^{47}$	2.018±0.70	201.38±65.8	$(6.58\pm268.1)\times10^{-13}$	0.304
HESS J1832-085	$(2.33\pm1.8)\times10^{47}$	2.017±0.23	163.30±35.1	$(4.27\pm5.6)\times10^{-13}$	0.522
HESS J1832-093	$(2.88\pm21.7)\times10^{47}$	2.028±0.67	36.97±124.4	$(1.71\pm40.2)\times10^{-13}$	0.311
HESS J1833-105	$(4.55\pm80.6)\times10^{47}$	2.175±1.20	132.97±93.4	$(4.01\pm376.3)\times10^{-13}$	0.246
HESS J1834-087	$(5.59\pm0.6)\times10^{48}$	2.145±0.02	46.25±2.7	$(2.76\pm0.2)\times10^{-12}$	0.089
HESS J1841-055	$(1.86\pm0.4\times10^{49}$	2.104±0.14	60.05±46.8	$(1.28\pm1.0)\times10^{-11}$	0.962
HESS J1843-033	$(7.33\pm6.5)\times10^{47}$	1.520±0.27	82.52±79.8	$(5.94\pm11.5)\times10^{-12}$	0.279
HESS J1844-030	$(4.42\pm2.2)\times10^{47}$	2.079±0.19	77.48±29.8	$(4.00\pm3.6)\times10^{-13}$	0.886
HESS J1846-029	$(9.84\pm172.8)\times10^{47}$	2.271±0.56	167.89±58.8	$(6.76\pm197.3)\times10^{-13}$	0.340
HESS J1848-018	$(3.07\pm3.7)\times10^{48}$	2.384±0.34	442.62±155.8	$(1.89\pm4.1)\times10^{-12}$	0.751
HESS J1852-000	$(6.55\pm133.7)\times10^{47}$	1.925±0.92	316.65±62.8	$(2.55\pm159.7)\times10^{-12}$	0.243
HESS J1857+026	$(1.13\pm0.3)\times10^{49}$	2.215±0.11	37.12±7.3	$(3.74\pm1.7)\times10^{-12}$	0.719
HESS J1858+020	$(6.63\pm1.0)\times10^{47}$	2.152±0.06	177.90±67.9	$(7.41\pm2.6)\times10^{-13}$	0.937
HESS J1908+063	$(6.36\pm73.3)\times10^{48}$	2.012±0.39	303.11±24.7	$(1.65\pm26.6)\times10^{-11}$	0.343
HESS J1911+090	$(2.19\pm22.9)\times10^{48}$	2.925±0.64	34.07±123.2	$(9.03\pm198.0)\times10^{-14}$	0.467
HESS J1912+101	$(1.49\pm0.3)\times10^{48}$	1.704±0.06	43.73±9.1	$(3.11\pm1.2)\times10^{-12}$	0.015
HESS J1923+141	$(1.94\pm1.8)\times10^{48}$	2.426±0.34	281.84±53.9	$(8.95\pm18.2)\times10^{-13}$	0.428
HESS J1930+188	$(1.00\pm7.1)\times10^{48}$	2.457±1.13	253.33±153.6	$(4.00\pm136.5)\times10^{-13}$	0.050
HESS J1943+213	$(1.03\pm0.2)\times10^{48}$	1.853±0.07	13.41±3.5	$(3.24\pm1.5)\times10^{-13}$	0.459

4: Conclusion

There are 47 unidentified sources in the HGPS. There is MeerKAT data only for the 1st and 4th quadrant of the Galactic Plane. There are only 8 unidentified H.E.S.S. sources in this region. 5 of these have had counterparts suggested but no confirmed indentification. HESS J1828-099, HESS J1503-582 and HESS J1708-410 have no nearby known objects. In the MeerKAT data there is radio emission nearby to the sources but the source of emission has not been determined yet. If the rest of the Galactic Plane gets observed by MeerKAT the remaining unidentified sources could be looked at in the same way.

For sources that are not excluded as most likely leptonic emitters (the sources that are firmly identified as PWNe) the neutrino flux was predicted assuming a purely hadronic scenario. The prediction is independent of the source class, distance to the source and the ambient density of the target material. This method can be expanded to other VHE sources and even diffuse gamma-ray emission. Further work which could be done is to use the neutrino model to fit to actual neutrino data. The model can be used as a template to be fit for observational data and to test for neutrino emission from gamma-ray sources which if detected would confirm them as hadronic.

None of the unidentified sources were identified in this work and no confirmation as to whether the sources are of hadronic or leptonic origin. However there are some indications that the sources with coincident neutrino emission could be hadronic. This work shows that with more MeerKAT observations some of the unidentified sources could be identified and the prediction of neutrino emission could be expanded to other gamma-ray sources other than the ones in the H.E.S.S. Galactic Plane Survey and tested against neutrino data.

Bibliography

[1] Victor F. Hess. Über Beobachtungen der durchdringenden Strahlung bei sieben Freiballonfahrten. *Phys. Z.*, 13:1084–1091, 1912. URL https://inspirehep.net/literature/1623161.

[2] Bernard Degrange and Gérard Fontaine. Introduction to high-energy gamma-ray astronomy. *Comptes Rendus Physique*, 16(6):587–599, 2015. ISSN 1631-0705. doi: https://doi.org/10.1016/j.crhy.2015.07.003. URL https://www.sciencedirect.com/science/article/pii/S1631070515001292. Gamma-ray astronomy / Astronomie des rayons gamma.

[3] H.E.S.S. Collaboration. The h.e.s.s. galactic plane survey. *Astronomy & Astrophysics*, 612:A1, Apr 2018. ISSN 1432-0746. doi: 10.1051/0004-6361/201732098. URL http://dx.doi.org/10.1051/0004-6361/201732098.

[4] SARAO and SKA South Africa. Meerkat radio telescope. https://www.sarao.ac.za/science/meerkat/about-meerkat/, 2020. Accessed: 2020-07-04.

[5] Mark Thompson, Sharmila Goedhart, S. Goedhart, P. Benaglia, H. Beuther, R. Blomme, A.C. Chrysostomou, J.S. Clark, C. Dickinson, S. Ellingsen, D. Fenech, L. Hindson, H.J. van Langevelde, S.N. Longmore, G. MacLeod, S. Molinari, R. Prinja, C.R. Purcell, I. Stevens, G. Umana, J.S. Urquhart, W. Vlemmings, A.J. Walsh, A.Y. Yang, and A. Zijlstra. MeerGAL: the MeerKAT Galactic Plane Survey. In *Proceedings of MeerKAT Science: On the Pathway to the SKA — PoS(MeerKAT2016)*, volume 277, page 015, 2018. doi: 10.22323/1.277.0015. URL https://pos.sissa.it/277/015/.

[6] S. R. Kelner, F. A. Aharonian, and V. V. Bugayov. Energy spectra of gamma rays, electrons, and neutrinos produced at proton-proton interactions in the very high energy regime. *Phys. Rev. D*, 74:034018, Aug 2006. doi: 10.1103/PhysRevD.74.034018. URL https://link.aps.org/doi/10.1103/PhysRevD.74.034018.

[7] Giulia Illuminati, Julien Aublin, and Sergio Navas. Searches for point-like sources of cosmic neutrinos with 11 years of ANTARES data. *PoS*, ICRC2019:920, 2019. doi: 10.22323/1.358.0920. URL https://pos.sissa.it/358/920/.

[8] Werner Hoffman. The H.E.S.S. Telescopes. https://www.mpi-hd.mpg.de/hfm/HESS/pages/about/telescopes/, 2012. Accessed: 2020-06-12.

[9] M. Ageron, J.A. Aguilar, I. Al Samarai, and A. Albert et al. Antares: The first undersea neutrino telescope. *Nuclear Instruments and Methods in Physics Research Section A: Accelerators, Spectrometers, Detectors and Associated Equipment*, 656(1):11–38, 2011. ISSN 0168-9002. doi: https://doi.org/10.1016/j.nima.2011.06.103. URL https://www.sciencedirect.com/science/article/pii/S0168900211013994.

[10] A. Albert, M. André, M. Anghinolfi, G. Anton, M. Ardid, J.-J. Aubert, J. Aublin, T. Avgitas, B. Baret, J. Barrios-Martí, S. Basa, B. Belhorma, V. Bertin, and et al. The search for neutrinos from txs 0506+056 with the antares telescope. *The Astrophysical Journal*, 863(2):L30, Aug 2018. ISSN 2041-8213. doi: 10.3847/2041-8213/aad8c0. URL http://dx.doi.org/10.3847/2041-8213/aad8c0.

[11] Francis Halzen and Spencer R. Klein. Invited review article: Icecube: An instrument for neutrino astronomy. *Review of Scientific Instruments*, 81(8):081101, 2010. doi: 10.1063/1.3480478. URL https://doi.org/10.1063/1.3480478.

[12] Rémy Le Breton. Km3net: Next-generation neutrino telescope in the mediterranean sea. *Nuclear Instruments and Methods in Physics Research Section A: Accelerators, Spectrometers, Detectors and Associated Equipment*, 936:204 – 207, 2019. ISSN 0168-9002. doi: https://doi.org/10.1016/j.nima.2018.10.103. URL http://www.sciencedirect.com/science/article/pii/S0168900218314189. Frontier Detectors for Frontier Physics: 14th Pisa Meeting on Advanced Detectors.

[13] Annarita Margiotta. The km3net deep-sea neutrino telescope. *Nuclear Instruments and Methods in Physics Research Section A: Accelerators, Spectrometers, Detectors and Associated Equipment*, 766:83–87, Dec 2014. ISSN 0168-9002. doi: 10.1016/j.nima.2014.05.090. URL http://dx.doi.org/10.1016/j.nima.2014.05.090.

[14] W. B. Atwood, A. A. Abdo, M. Ackermann, W. Althouse, B. Anderson, M. Axelsson, L. Baldini, J. Ballet, D. L. Band, G. Barbiellini, and et al. The large area telescope on thefermi gamma-ray space telescopemission. *The Astrophysical Journal*, 697(2):1071–1102, May 2009. ISSN 1538-4357. doi: 10.1088/0004-637x/697/2/1071. URL http://dx.doi.org/10.1088/0004-637X/697/2/1071.

[15] Fermi/LAT Collaboration. The Fourth Catalog of Active Galactic Nuclei Detected by the Fermi Large Area Telescope. *ApJ*, 892(2):105,

April 2020. doi: 10.3847/1538-4357/ab791e. URL https://ui.adsabs.harvard.edu/abs/2020ApJ...892..105A.

[16] D. Khangulyan, F. A. Aharonian, and S. R. Kelner. SIMPLE ANALYTICAL APPROXIMATIONS FOR TREATMENT OF INVERSE COMPTON SCATTERING OF RELATIVISTIC ELECTRONS IN THE BLACKBODY RADIATION FIELD. *The Astrophysical Journal*, 783(2):100, feb 2014. doi: 10.1088/0004-637x/783/2/100. URL https://doi.org/10.1088%2F0004-637x%2F783%2F2%2F100.

[17] V. Zabalza. naima: a python package for inference of relativistic particle energy distributions from observed nonthermal spectra. *Proc. of International Cosmic Ray Conference 2015*, page 922, 2015. URL http://adsabs.harvard.edu/abs/2015arXiv150903319Z.

[18] Ervin Kafexhiu, Felix Aharonian, Andrew M. Taylor, and Gabriela S. Vila. Parametrization of gamma-ray production cross sections for *pp* interactions in a broad proton energy range from the kinematic threshold to pev energies. *Phys. Rev. D*, 90:123014, Dec 2014. doi: 10.1103/PhysRevD.90.123014. URL https://link.aps.org/doi/10.1103/PhysRevD.90.123014.

[19] F. A. Aharonian, S. R. Kelner, and A. Yu. Prosekin. Angular, spectral, and time distributions of highest energy protons and associated secondary gamma rays and neutrinos propagating through extragalactic magnetic and radiation fields. *Phys. Rev. D*, 82(4):043002, August 2010. doi: 10.1103/PhysRevD.82.043002. URL https://ui.adsabs.harvard.edu/abs/2010PhRvD..82d3002A.

[20] A. D. P. Hands, R. S. Warwick, M. G. Watson, and D. J. Helfand. X-ray source populations in the Galactic plane. *MNRAS*, 351(1):31–56, June 2004. doi: 10.1111/j.1365-2966.2004.07777.x. URL https://ui.adsabs.harvard.edu/abs/2004MNRAS.351...31H.

[21] Nigel I. Maxted, M. D. Filipović, N. Hurley-Walker, I. Bojičić, G. P. Rowell, F. Haberl, A. J. Ruiter, I. R. Seitenzahl, F. Panther, G. F. Wong, C. Braiding, M. Burton, G. Pühlhofer, H. Sano, Y. Fukui, M. Sasaki, W. Tian, H. Su, X. Cui, D. Leahy, and P. J. Hancock. A Supernova Remnant Counterpart for HESS J1832-085. *ApJ*, 885(2):129, November 2019. doi: 10.3847/1538-4357/ab3e3f. URL https://ui.adsabs.harvard.edu/abs/2019ApJ...885..129M.

[22] Cui, Y., Xin, Y., Liu, S., Tam, P. H. T., Pühlhofer, G., and Zhu, H. Hess j1858+020: A gev-tev source possibly powered by cosmic rays from snr g35.6-0.4. *A&A*, 646:A114, 2021. doi: 10.1051/0004-6361/202039041. URL https://doi.org/10.1051/0004-6361/202039041.

[23] P. Hofverberg, R. C. G. Chaves, A. Fiasson, K. Kosack, J. Méhault, E. de Onã Wilhelmi, and H. E. S. S. Collaboration. Discovery of VHE gamma-rays from the vicinity of the shell-type SNR G318.2+0.1 with H.E.S.S. In Frank M. Rieger, Christopher van Eldik, and Werner Hofmann, editors, *25th Texas Symposium on Relativistic Astrophysics*, page 196, January 2010. URL https://ui.adsabs.harvard.edu/abs/2010tsra.confE.196H.

[24] J. Eagle, S. Marchesi, D. Castro, M. Ajello, and A. Vendrasco. Gamma-ray emission revealed at the western edge of snr g344.7–0.1. *The Astrophysical Journal*, 904(2):123, Nov 2020. ISSN 1538-4357. doi: 10.3847/1538-4357/abbe08. URL http://dx.doi.org/10.3847/1538-4357/abbe08.

[25] M. Capasso, B. Condon, M. Coffaro, Y. Cui, D. Gottschall, D. Klochkov, V. Marandon, N. Maxted, G. Pühlhofer, G. Rowell, and H. E. S. S. Collaboration. The TeV supernova remnant shell HESS J1731-347 and its surroundings. In *6th International Symposium on High Energy Gamma-Ray Astronomy*, volume 1792 of *American Institute of Physics Conference Series*, page 040026, January 2017. doi: 10.1063/1.4968930. URL https://ui.adsabs.harvard.edu/abs/2017AIPC.1792d0026C.

[26] G. Castelletti, L. Supan, A. Petriella, E. Giacani, and B. C. Joshi. Radio and X-ray properties of the source G29.37+0.1 linked to HESS J1844-030. *A&A*, 602:A31, June 2017. doi: 10.1051/0004-6361/201630093. URL https://ui.adsabs.harvard.edu/abs/2017A&A...602A..31C.

[27] A. Petriella. New composite supernova remnant toward HESS J1844-030? *A&A*, 626:A65, June 2019. doi: 10.1051/0004-6361/201834734. URL https://ui.adsabs.harvard.edu/abs/2019A&A...626A..65P.

[28] Ivan Yu. Zolotukhin, Matteo Bachetti, Nicola Sartore, Igor V. Chilingarian, and Natalie A. Webb. The Slowest Spinning X-Ray Pulsar in an Extragalactic Globular Cluster. *ApJ*, 839(2):125, April 2017. doi: 10.3847/1538-4357/aa689d.

[29] S. Safi-Harb, I. M. Harrus, R. Petre, G. G. Pavlov, A. B. Koptsevich, and D. Sanwal. X-Ray Observations of the Supernova Remnant G21.5-

0.9. *ApJ*, 561(1):308–320, November 2001. doi: 10.1086/322978. URL https://ui.adsabs.harvard.edu/abs/2001ApJ...561..308S.

[30] F. Bocchino, E. van der Swaluw, R. Chevalier, and R. Bandiera. The nature of the X-ray halo of the plerion G21.5-0.9 unveiled by XMM-Newton and Chandra. *A&A*, 442(2):539–548, November 2005. doi: 10.1051/0004-6361:20052870. URL https://ui.adsabs.harvard.edu/abs/2005A&A...442..539B.

[31] Martocchia, A., Motch, C., and Negueruela, I. The low x-ray state of ls 503926.2-1450. *A&A*, 430(1):245–253, 2005. doi: 10.1051/0004-6361:20041390. URL https://doi.org/10.1051/0004-6361:20041390.

[32] Deil, C. et al. Gammapy - A prototype for the CTA science tools. In *35th International Cosmic Ray Conference (ICRC2017)*, volume 301 of *International Cosmic Ray Conference*, page 766, January 2017. URL https://ui.adsabs.harvard.edu/abs/2017ICRC...35..766D.

[33] Nigro, C. et al. Towards open and reproducible multi-instrument analysis in gamma-ray astronomy. *A&A*, 625:A10, May 2019. doi: 10.1051/0004-6361/201834938. URL https://ui.adsabs.harvard.edu/abs/2019A&A...625A..10N.

[34] H.E.S.S. Collaboration. Diffuse galactic gamma-ray emission with h.e.s.s. *Phys. Rev. D*, 90:122007, Dec 2014. doi: 10.1103/PhysRevD.90.122007. URL https://0-link-aps-org.innopac.wits.ac.za/doi/10.1103/PhysRevD.90.122007.

[35] Amenomori, M. et al. First detection of sub-pev diffuse gamma rays from the galactic disk: Evidence for ubiquitous galactic cosmic rays beyond pev energies. *Phys. Rev. Lett.*, 126:141101, Apr 2021. doi: 10.1103/PhysRevLett.126.141101. URL https://link.aps.org/doi/10.1103/PhysRevLett.126.141101.

Appendices

Appendix A: Sampler fits

Here you can see the sampler fits for each of the HGPS sources made using naima[17]. The thick black line shows the line with maximum log likelihood while the gray bands are the 3 sigma and 1 sigma confidence bands. The H.E.S.S. data is in green and the Fermi data is in blue. To see the parameters of the fit see Table 3.1

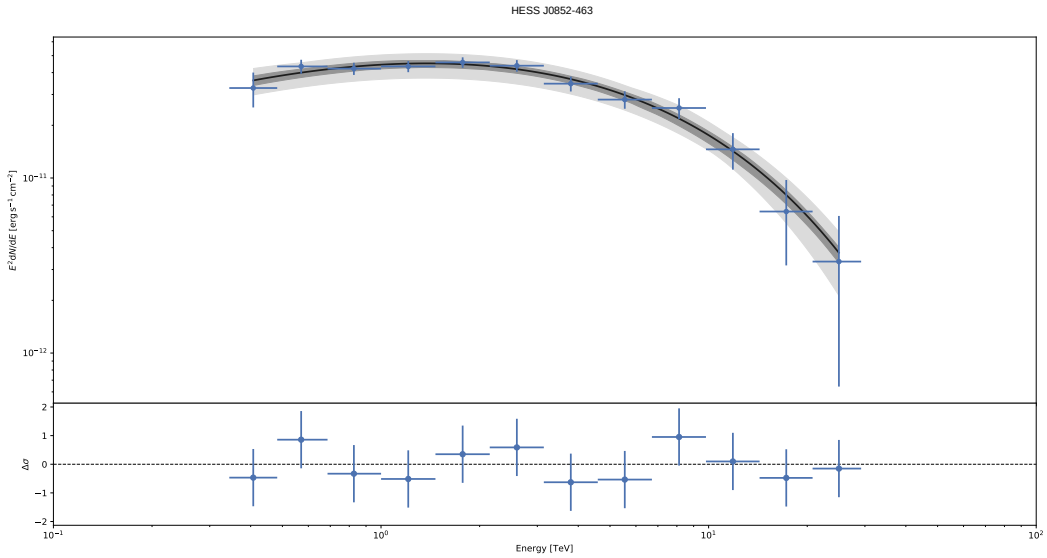
HESS J0852-463
E^2dN/dE [erg s^{-1} cm^{-2}]
10^{-11}
10^{-12}
$\Delta\sigma$
2
1
0
−1
−2
10^{-1}
10^{0}
10^{1}
10^{2}
Energy [TeV]

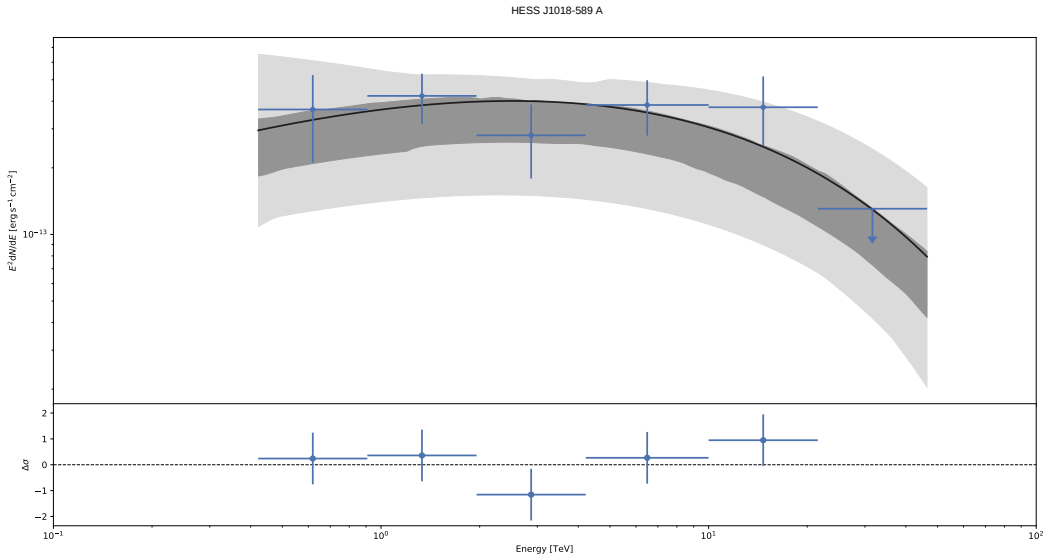
HESS J1018-589 A
E^2dN/dE [erg s^{-1} cm^{-2}]
10^{-13}
$\Delta\sigma$
2
1
0
−1
−2
10^{-1}
10^{0}
10^{1}
10^{2}
Energy [TeV]

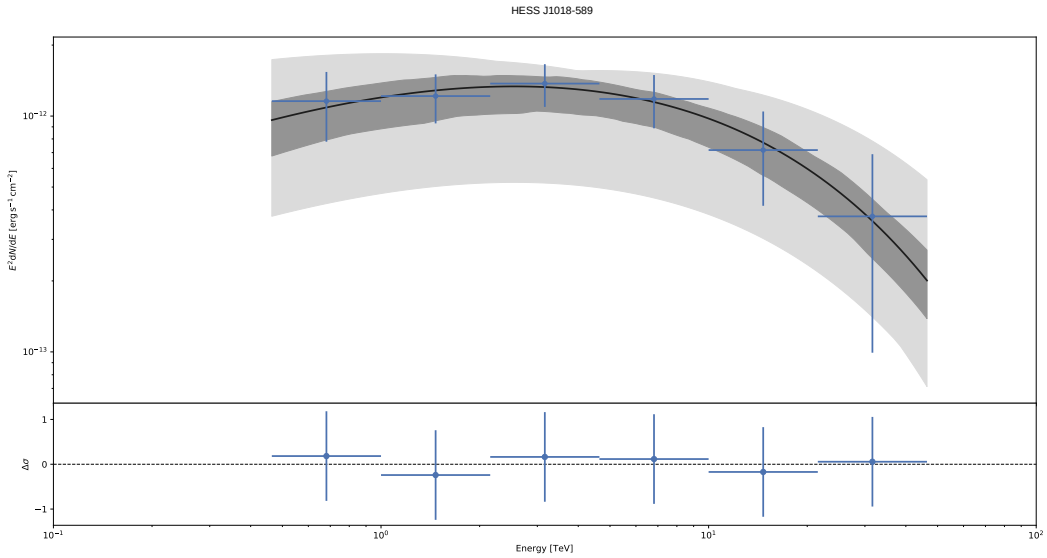
HESS J1018-589
E^2dN/dE [erg s^{-1} cm^{-2}]
10^{-12}
10^{-13}
$\Delta\sigma$
1
0
−1
10^{-1}
10^{0}
10^{1}
10^{2}
Energy [TeV]

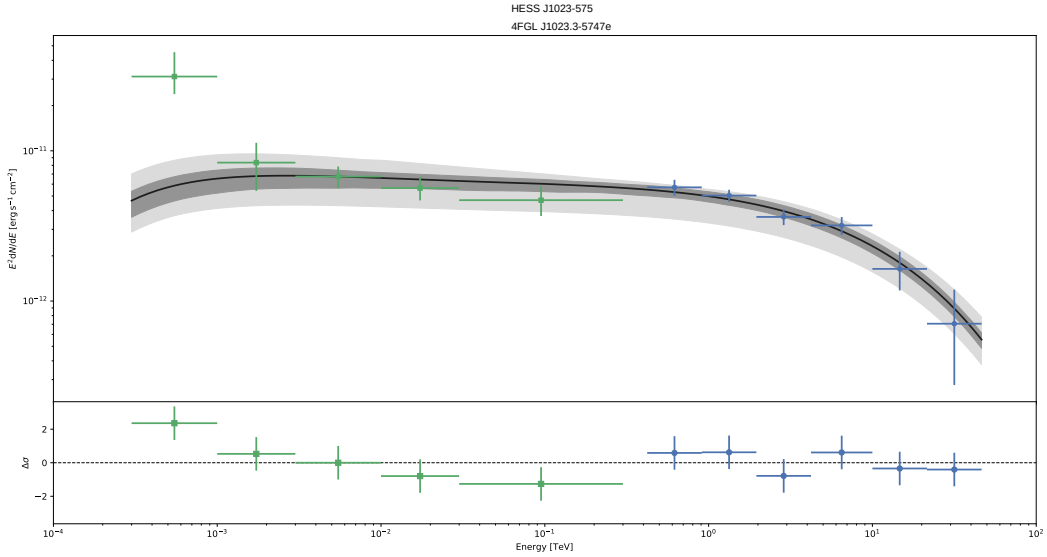
HESS J1023-575
4FGL J1023.3-5747e
E^2dN/dE [erg s^{-1} cm^{-2}]
10^{-11}
10^{-12}
$\Delta\sigma$
2
0
−2
10^{-4}
10^{-3}
10^{-2}
10^{-1}
10^{0}
10^{1}
10^{2}
Energy [TeV]

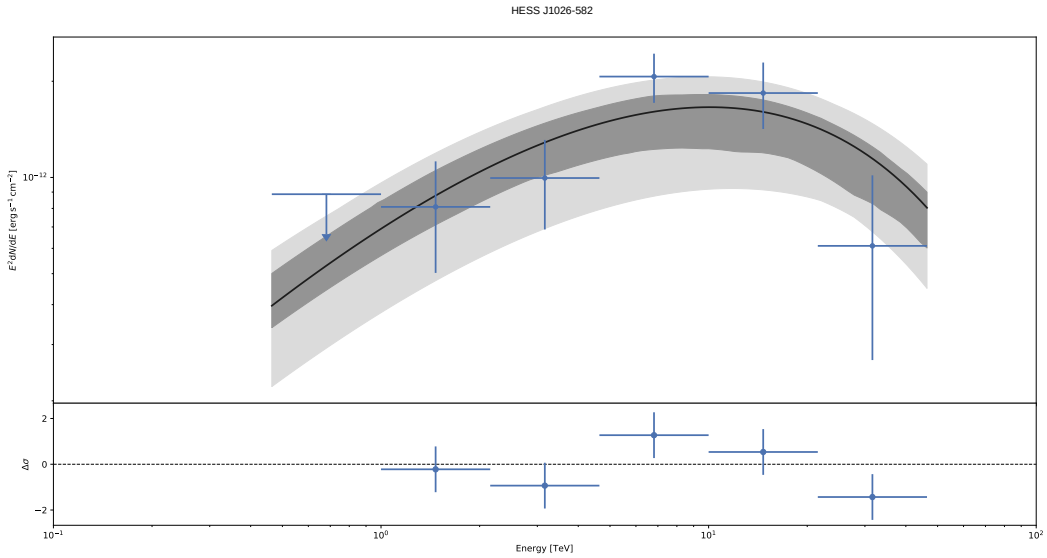
HESS J1026-582
E^2dN/dE [erg s^{-1} cm^{-2}]
10^{-12}
$\Delta\sigma$
2
0
−2
10^{-1}
10^{0}
10^{1}
10^{2}
Energy [TeV]

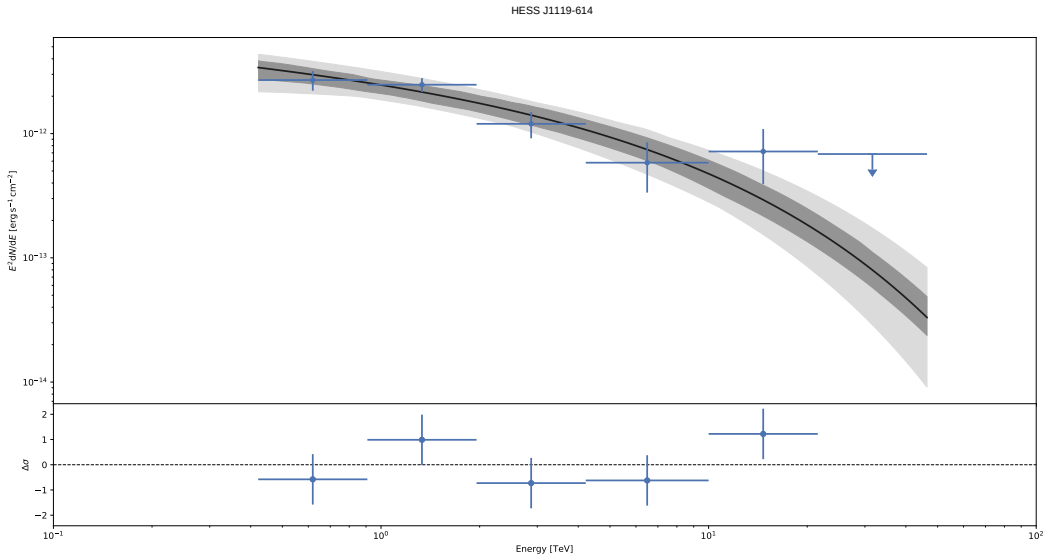
HESS J1119-614
E^2dN/dE [erg s^{-1} cm^{-2}]
10^{-12}
10^{-13}
10^{-14}
$\Delta\sigma$
2
1
0
−1
−2
10^{-1}
10^{0}
10^{1}
10^{2}
Energy [TeV]

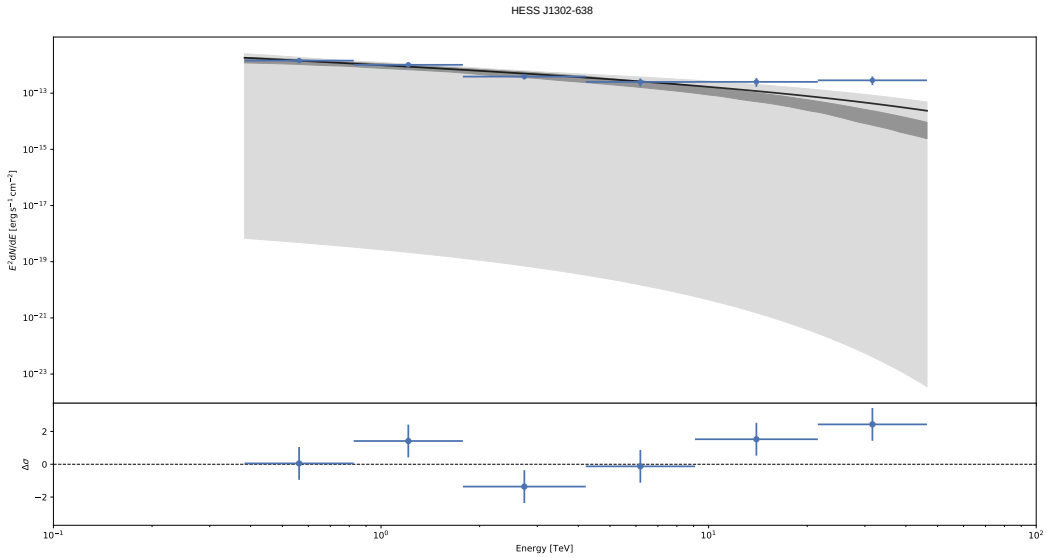
HESS J1302-638
E^2dN/dE [erg s^{-1} cm^{-2}]
10^{-13}
10^{-15}
10^{-17}
10^{-19}
10^{-21}
10^{-23}
$\Delta\sigma$
2
0
−2
10^{-1}
10^{0}
10^{1}
10^{2}
Energy [TeV]

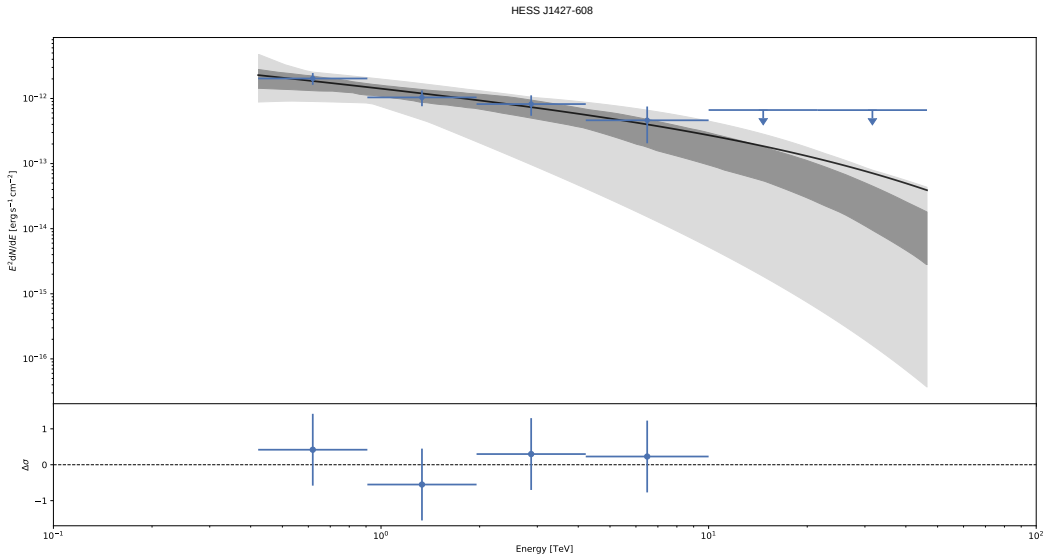
HESS J1427-608
E^2dN/dE [erg s^{-1} cm^{-2}]
10^{-12}
10^{-13}
10^{-14}
10^{-15}
10^{-16}
$\Delta\sigma$
1
0
−1
10^{-1}
10^{0}
10^{1}
10^{2}
Energy [TeV]

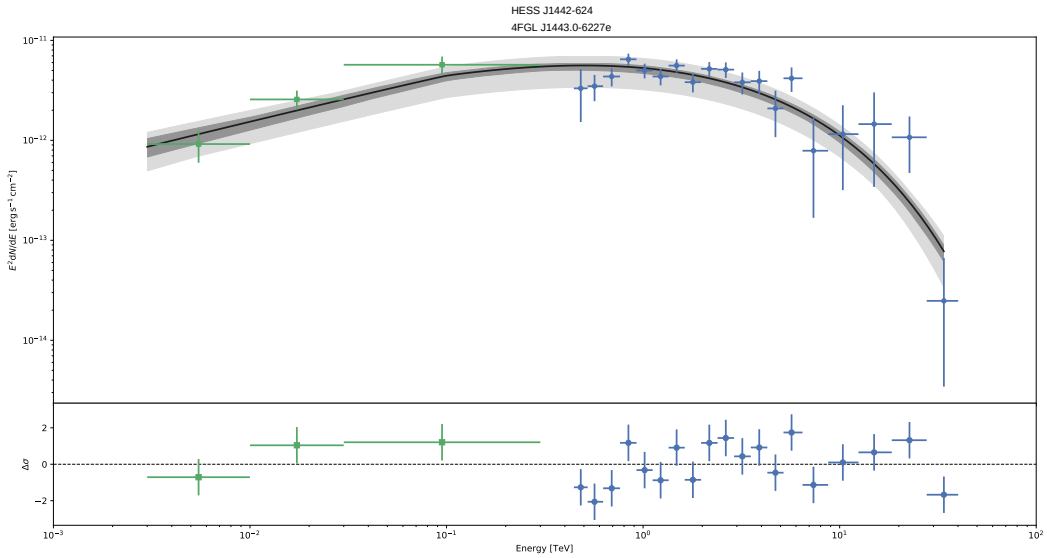
HESS J1442-624
4FGL J1443.0-6227e
E^2dN/dE [erg s^{-1} cm^{-2}]
$\Delta\sigma$
Energy [TeV]

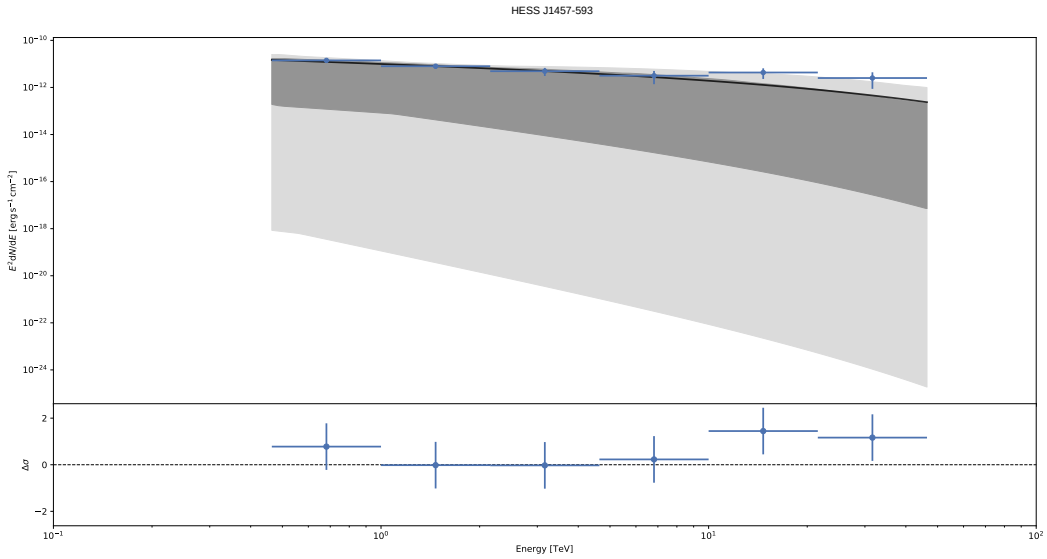
HESS J1457-593
E^2dN/dE [erg s^{-1} cm^{-2}]
$\Delta\sigma$
Energy [TeV]

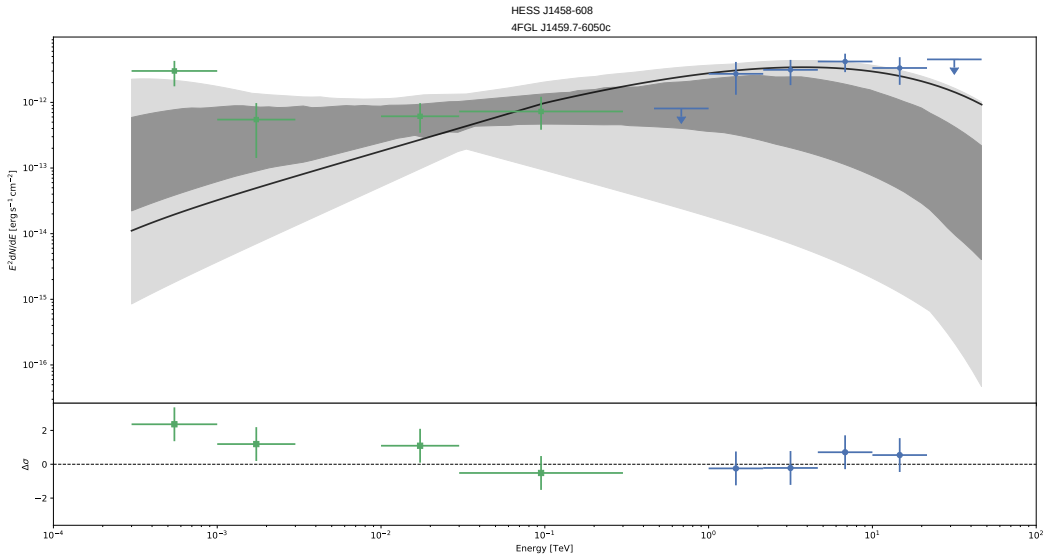
HESS J1458-608
4FGL J1459.7-6050c
E^2dN/dE [erg s^{-1} cm^{-2}]
$\Delta\sigma$
Energy [TeV]

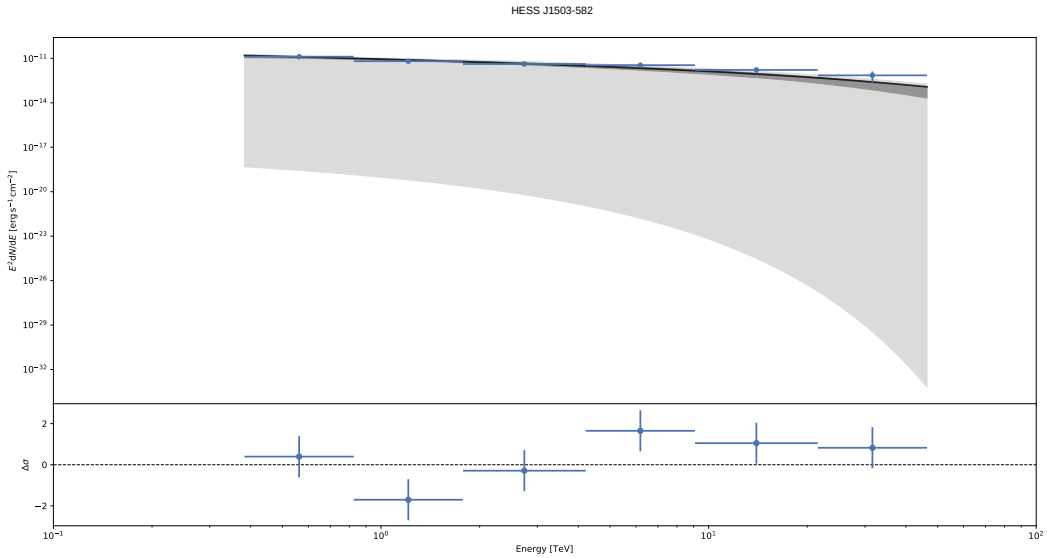
HESS J1503-582
E^2dN/dE [erg s^{-1} cm^{-2}]
$\Delta\sigma$
Energy [TeV]

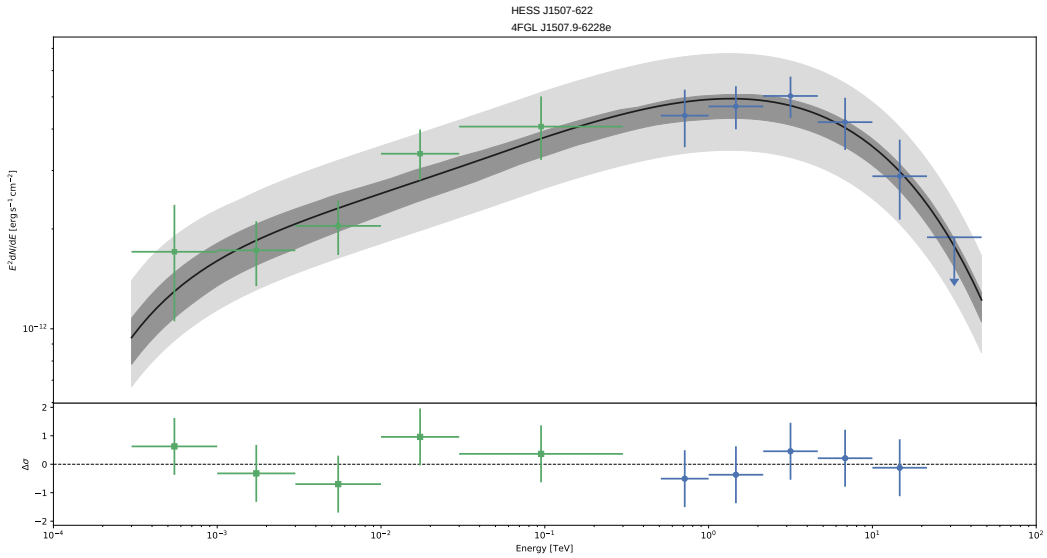
HESS J1507-622
4FGL J1507.9-6228e
E^2dN/dE [erg s^{-1} cm^{-2}]
10^{-12}
$\Delta\sigma$
Energy [TeV]

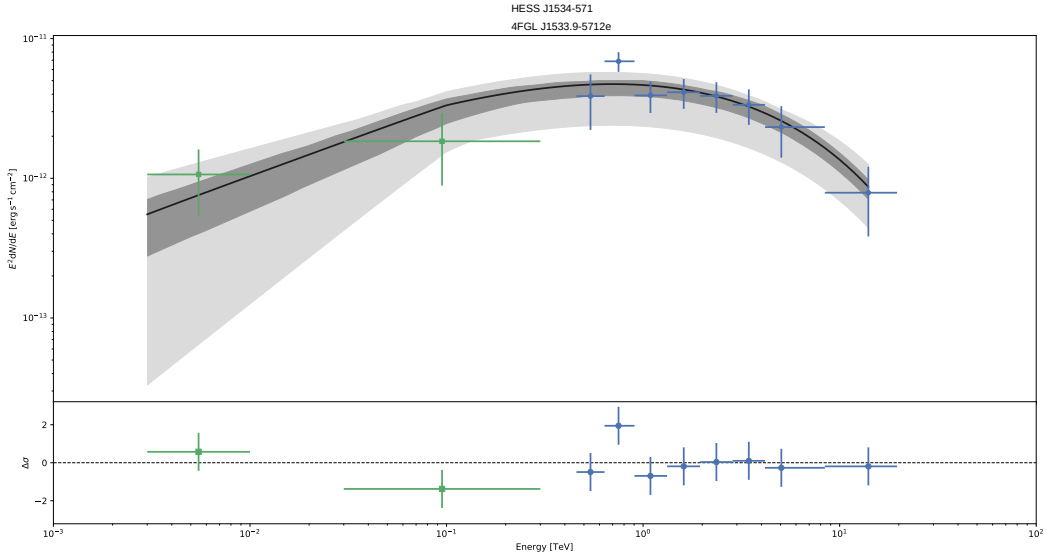
HESS J1534-571
4FGL J1533.9-5712e
E^2dN/dE [erg s^{-1} cm^{-2}]
10^{-11}
10^{-12}
10^{-13}
$\Delta\sigma$
Energy [TeV]

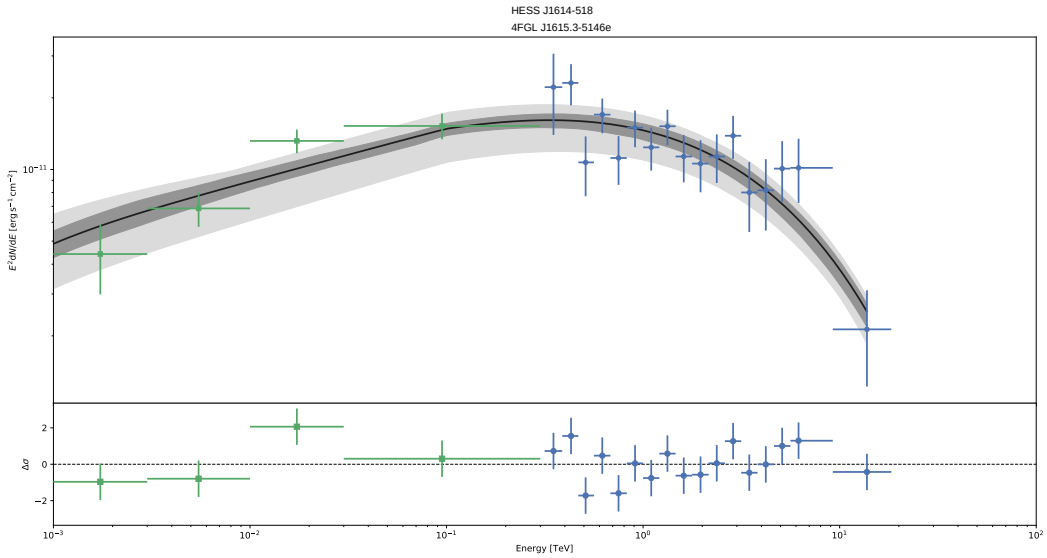
HESS J1614-518
4FGL J1615.3-5146e
E^2dN/dE [erg s^{-1} cm^{-2}]
10^{-11}
$\Delta\sigma$
2
0
−2
10^{-3}
10^{-2}
10^{-1}
10^{0}
10^{1}
10^{2}
Energy [TeV]

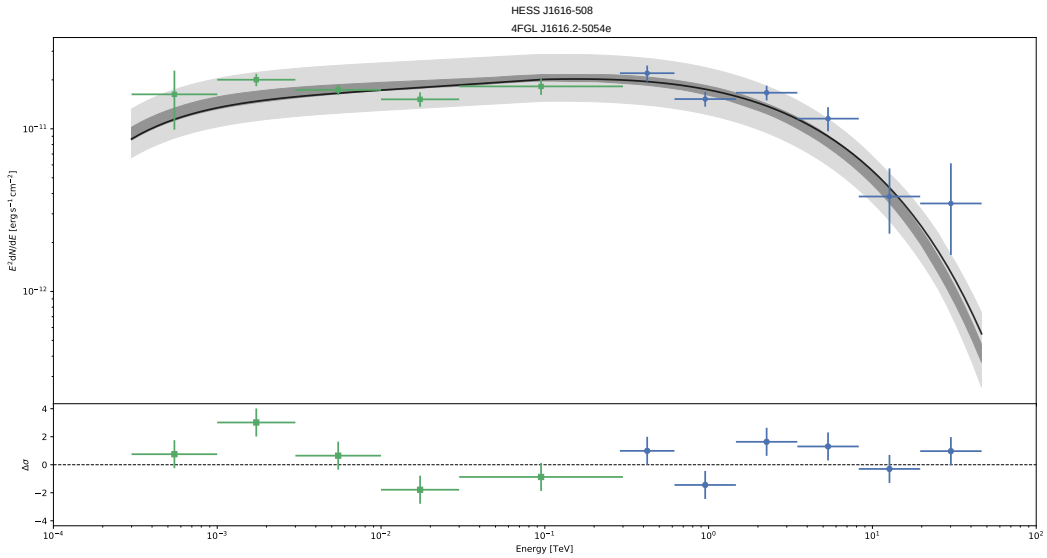
HESS J1616-508
4FGL J1616.2-5054e
E^2dN/dE [erg s^{-1} cm^{-2}]
10^{-11}
10^{-12}
$\Delta\sigma$
4
2
0
−2
−4
10^{-4}
10^{-3}
10^{-2}
10^{-1}
10^{0}
10^{1}
10^{2}
Energy [TeV]

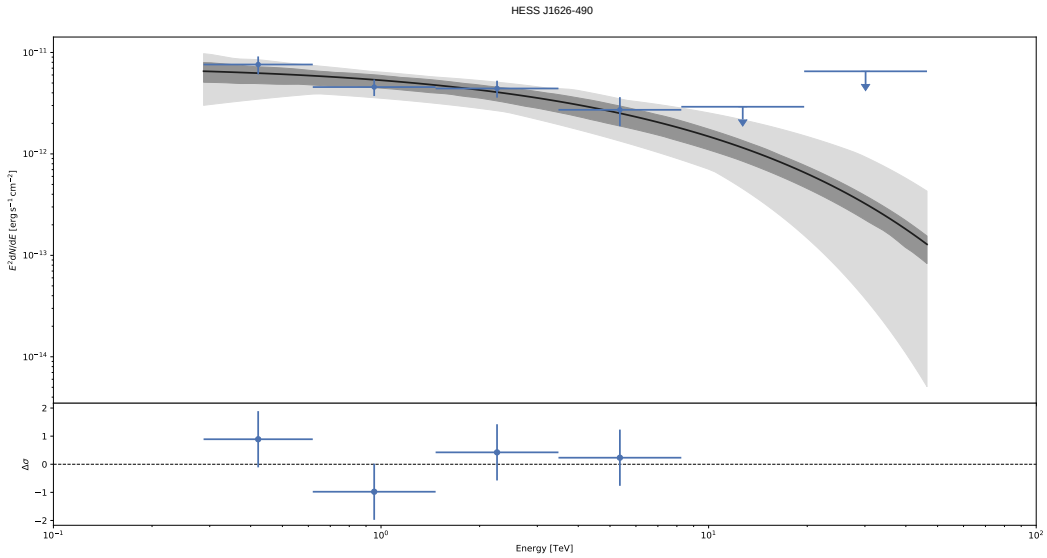
HESS J1626-490
E^2dN/dE [erg s^{-1} cm^{-2}]
$\Delta\sigma$
Energy [TeV]

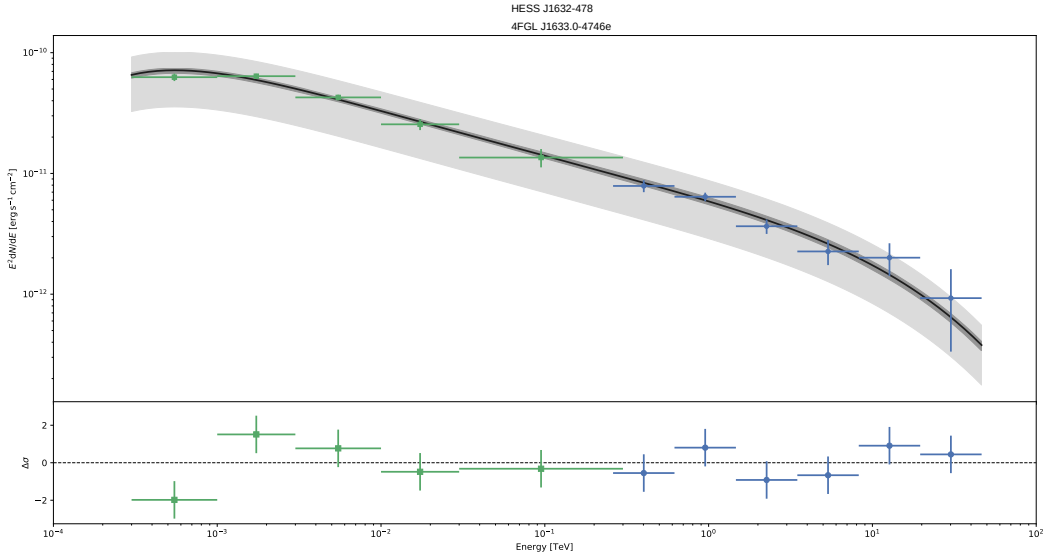
HESS J1632-478
4FGL J1633.0-4746e
E^2dN/dE [erg s^{-1} cm^{-2}]
$\Delta\sigma$
Energy [TeV]

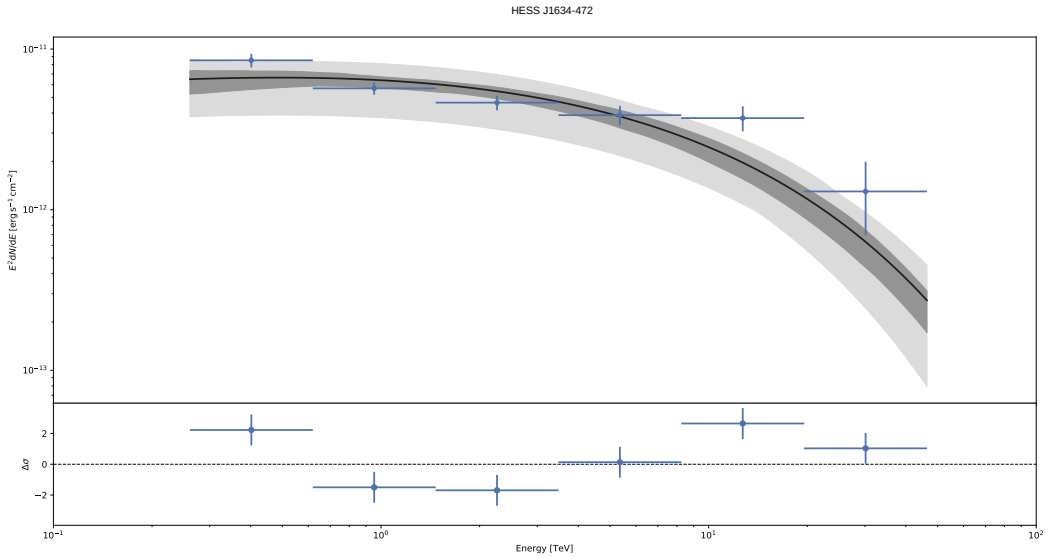
HESS J1634-472
E^2dN/dE [erg s^{-1} cm^{-2}]
$\Delta\sigma$
Energy [TeV]

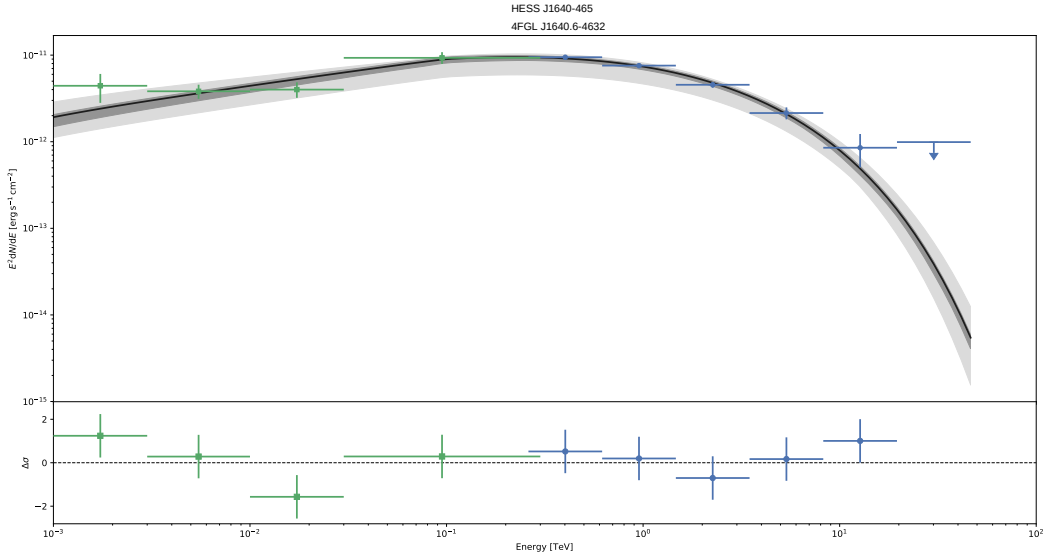
HESS J1640-465
4FGL J1640.6-4632
E^2dN/dE [erg s^{-1} cm^{-2}]
$\Delta\sigma$
Energy [TeV]

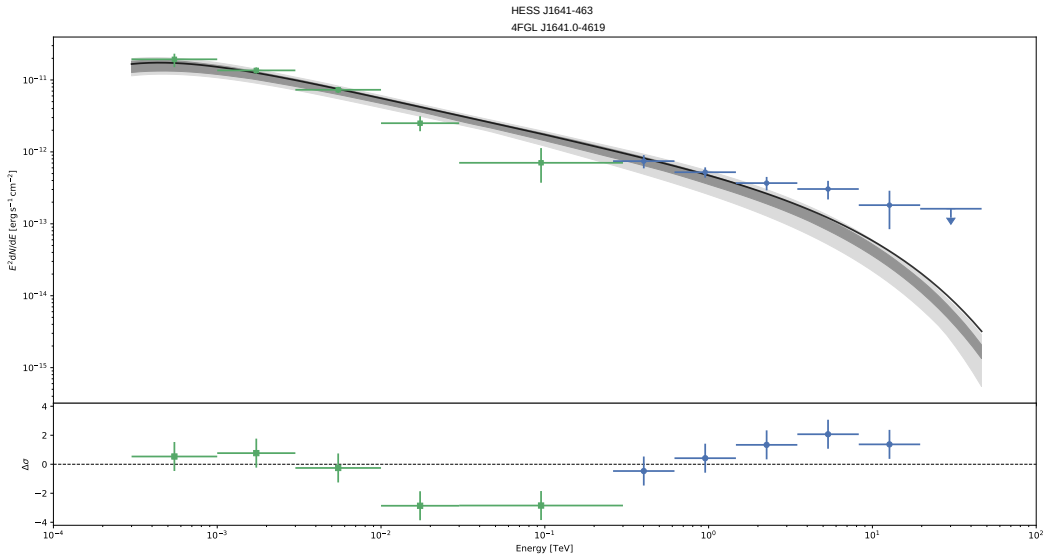
HESS J1641-463
4FGL J1641.0-4619
E^2dN/dE [erg s^{-1} cm^{-2}]
$\Delta\sigma$
Energy [TeV]

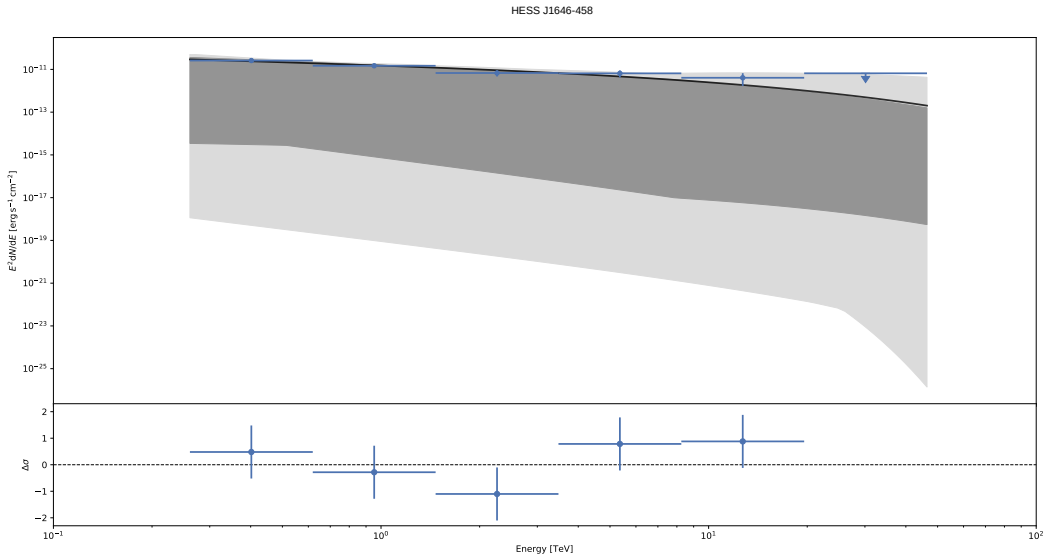
HESS J1646-458
E^2dN/dE [erg s^{-1} cm^{-2}]
$\Delta\sigma$
Energy [TeV]

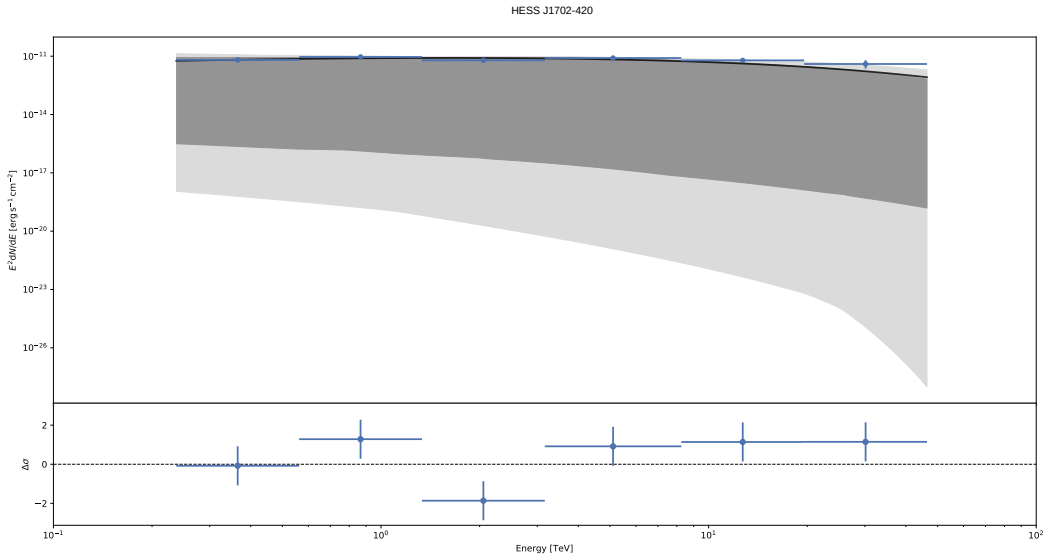
HESS J1702-420
E^2dN/dE [erg s^{-1} cm^{-2}]
10^{-11}
10^{-14}
10^{-17}
10^{-20}
10^{-23}
10^{-26}
$\Delta\sigma$
2
0
−2
10^{-1}
10^{0}
10^{1}
10^{2}
Energy [TeV]

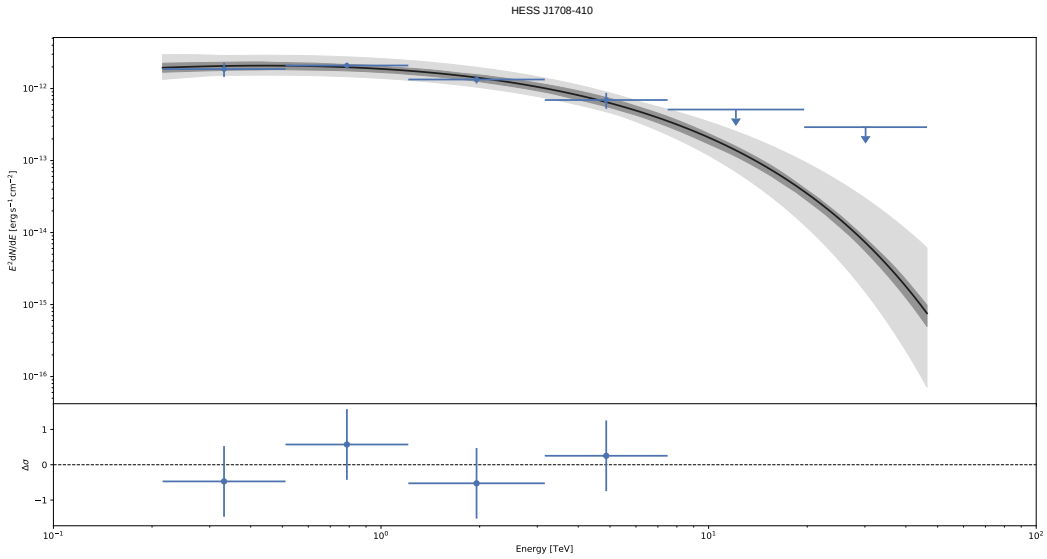
HESS J1708-410
E^2dN/dE [erg s^{-1} cm^{-2}]
10^{-12}
10^{-13}
10^{-14}
10^{-15}
10^{-16}
$\Delta\sigma$
1
0
−1
10^{-1}
10^{0}
10^{1}
10^{2}
Energy [TeV]

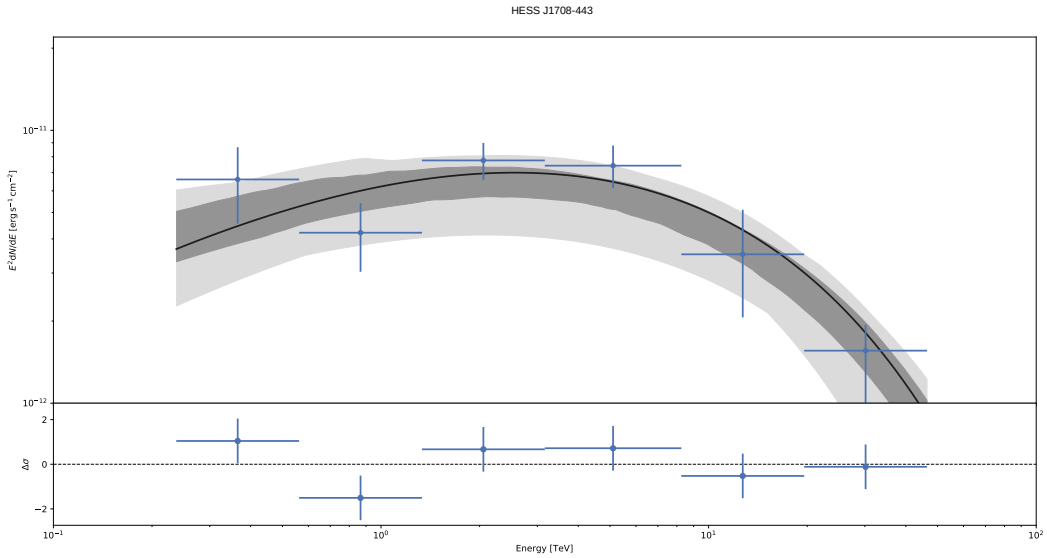
HESS J1708-443
E^2dN/dE [erg s^{-1} cm^{-2}]
10^{-11}
10^{-12}
$\Delta\sigma$
2
0
−2
10^{-1}
10^{0}
10^{1}
10^{2}
Energy [TeV]

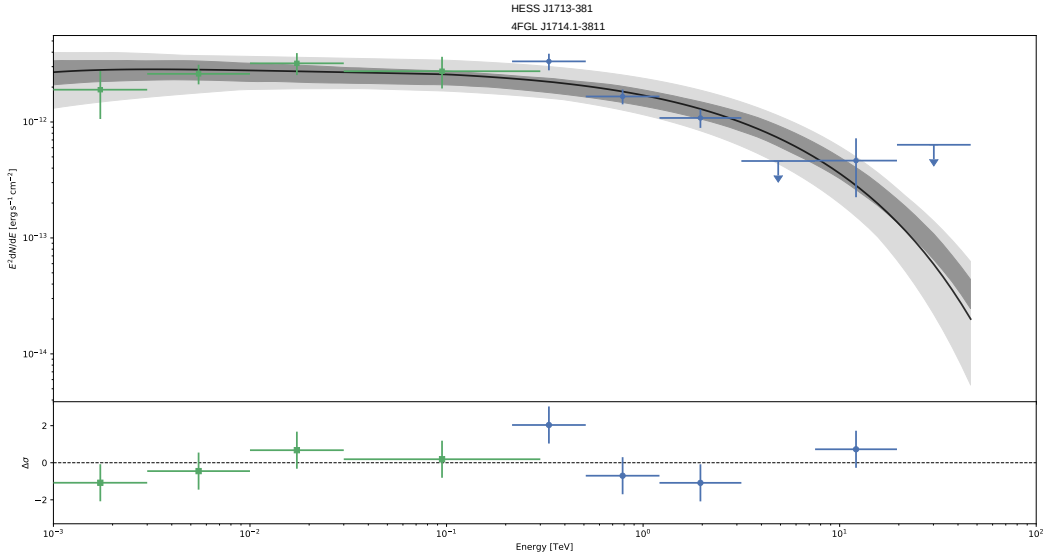
HESS J1713-381
4FGL J1714.1-3811
E^2dN/dE [erg s^{-1} cm^{-2}]
10^{-12}
10^{-13}
10^{-14}
$\Delta\sigma$
2
0
−2
10^{-3}
10^{-2}
10^{-1}
10^{0}
10^{1}
10^{2}
Energy [TeV]

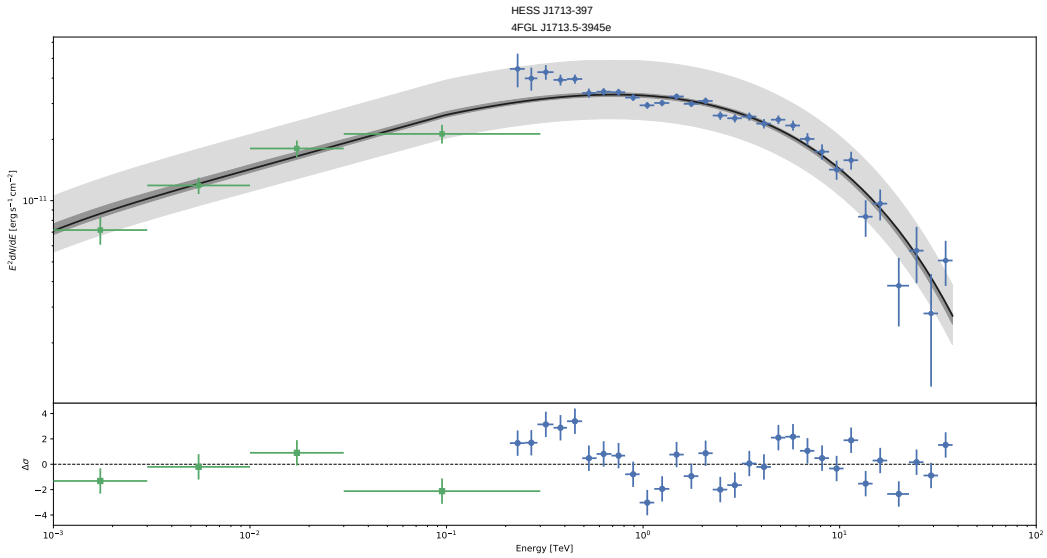
HESS J1713-397
4FGL J1713.5-3945e
E^2dN/dE [erg s^{-1} cm^{-2}]
10^{-11}
$\Delta\sigma$
Energy [TeV]

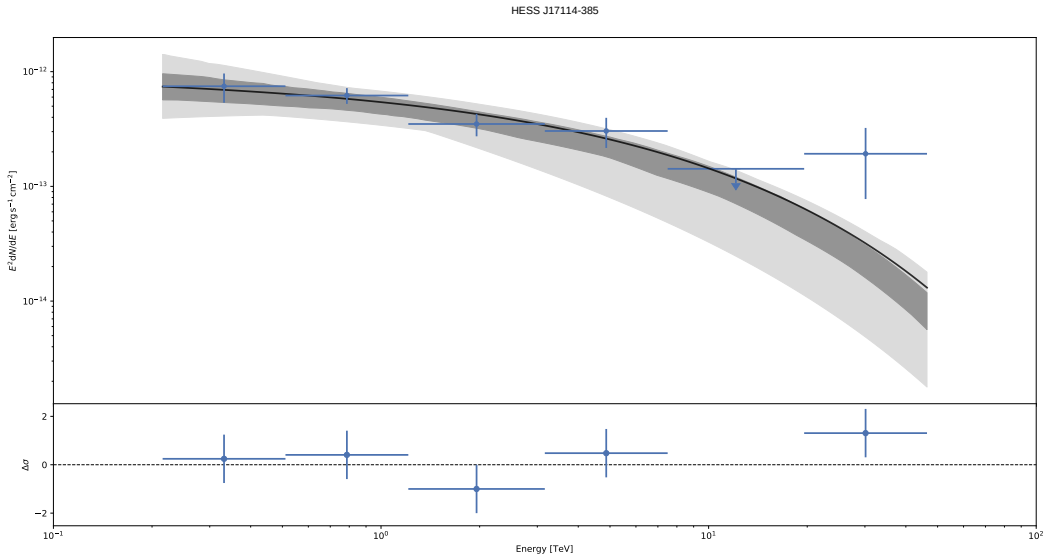
HESS J17114-385
E^2dN/dE [erg s^{-1} cm^{-2}]
10^{-12}
10^{-13}
10^{-14}
$\Delta\sigma$
Energy [TeV]

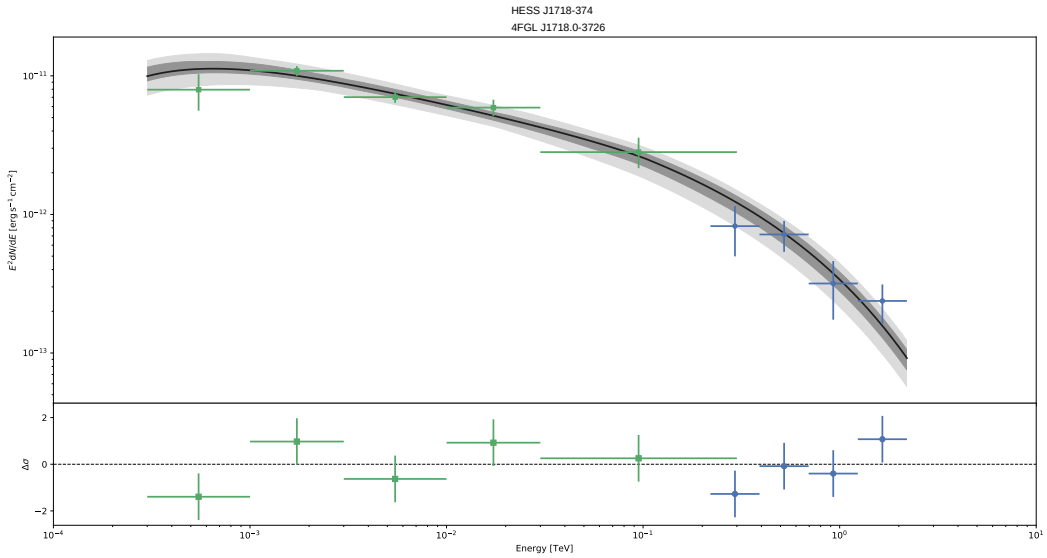
HESS J1718-374
4FGL J1718.0-3726
E^2dN/dE [erg s^{-1} cm^{-2}]
$\Delta\sigma$
Energy [TeV]

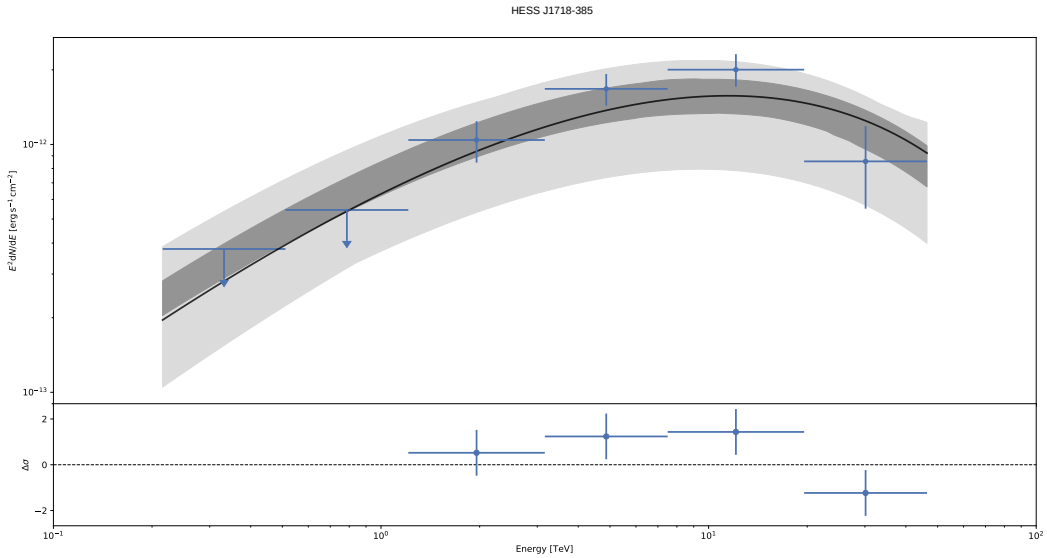
HESS J1718-385
E^2dN/dE [erg s^{-1} cm^{-2}]
$\Delta\sigma$
Energy [TeV]

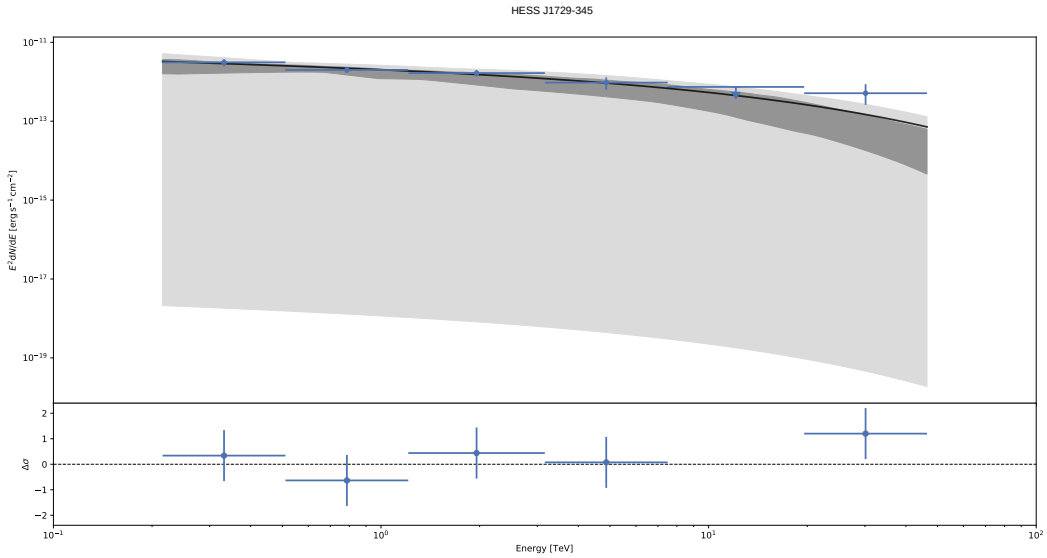
HESS J1729-345
E^2dN/dE [erg s^{-1} cm^{-2}]
$\Delta\sigma$
Energy [TeV]

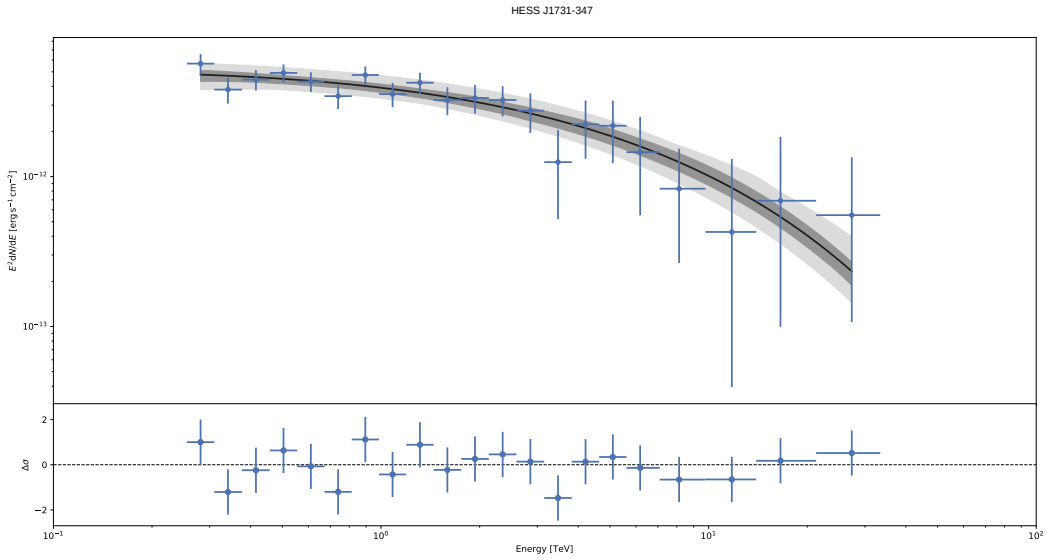
HESS J1731-347
E^2dN/dE [erg s^{-1} cm^{-2}]
$\Delta\sigma$
Energy [TeV]

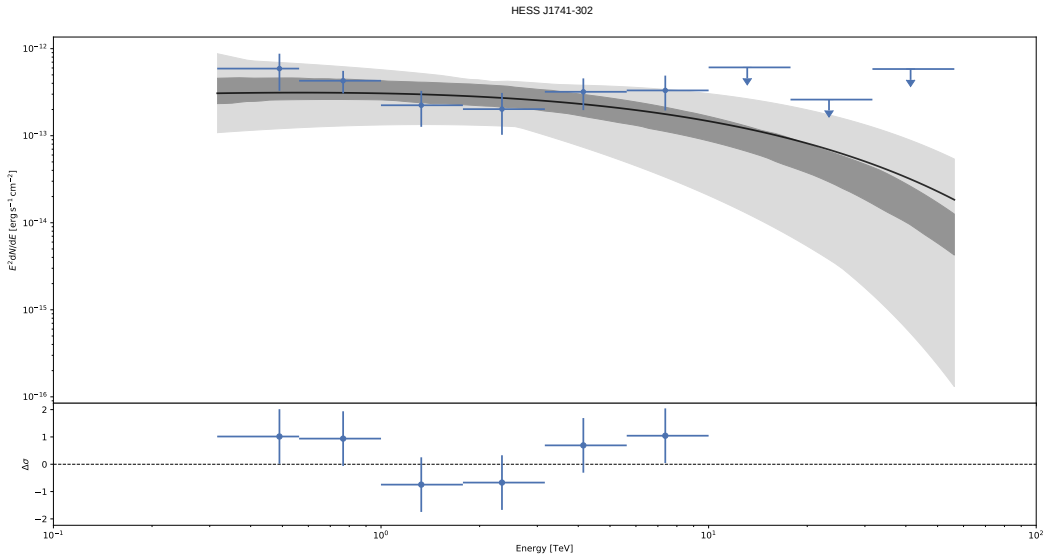
HESS J1741-302
E^2dN/dE [erg s^{-1} cm^{-2}]
$\Delta\sigma$
Energy [TeV]

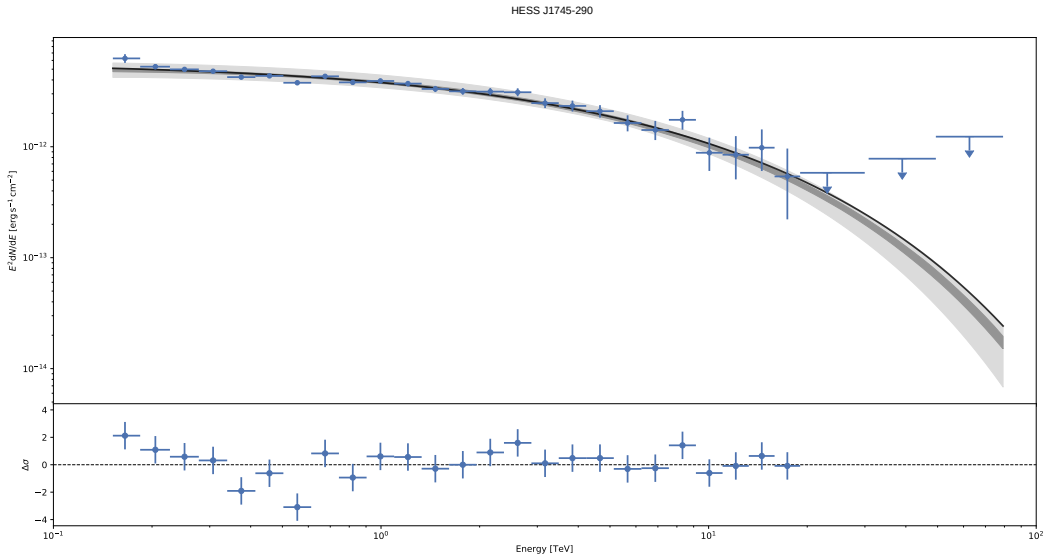
HESS J1745-290
E^2dN/dE [erg s^{-1} cm^{-2}]
$\Delta\sigma$
Energy [TeV]

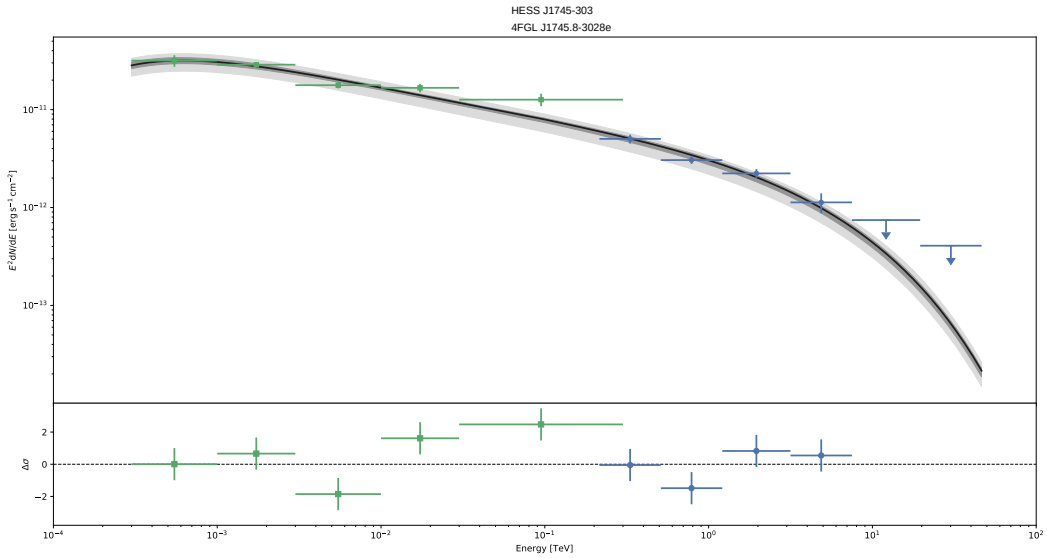
HESS J1745-303
4FGL J1745.8-3028e
E^2dN/dE [erg s^{-1} cm^{-2}]
$\Delta\sigma$
Energy [TeV]

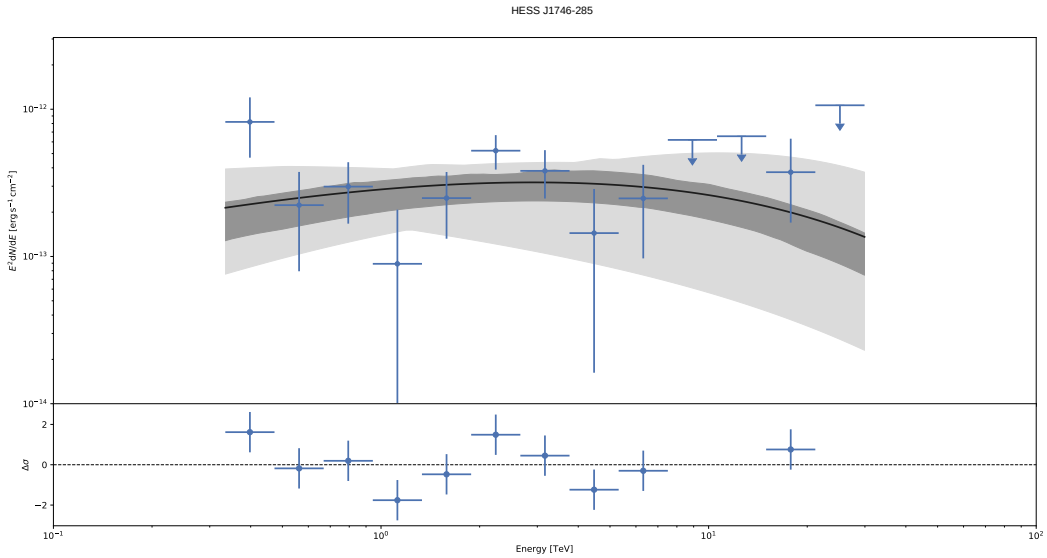
HESS J1746-285
E^2dN/dE [erg s^{-1} cm^{-2}]
$\Delta\sigma$
Energy [TeV]

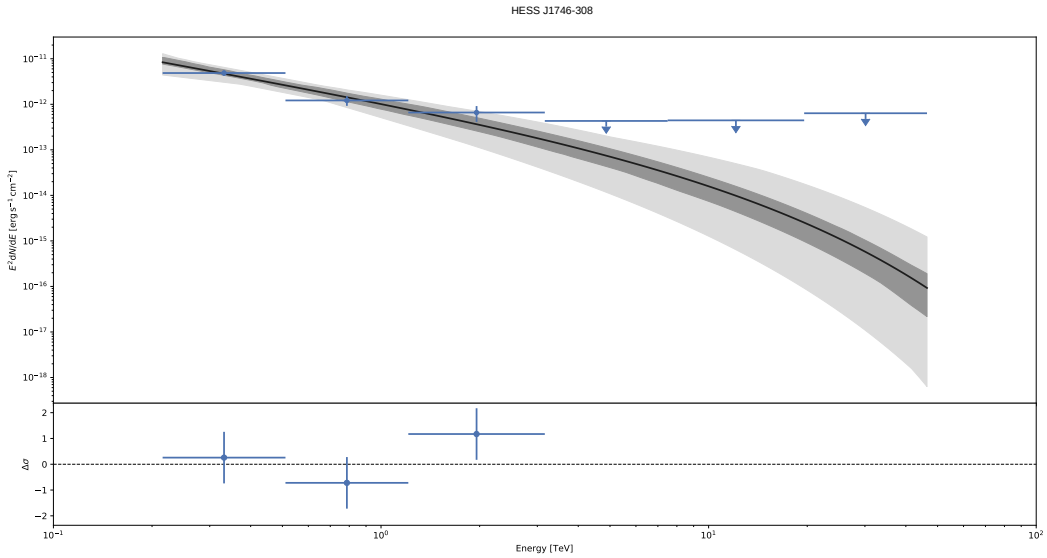
HESS J1746-308
E^2dN/dE [erg s^{-1} cm^{-2}]
$\Delta\sigma$
Energy [TeV]

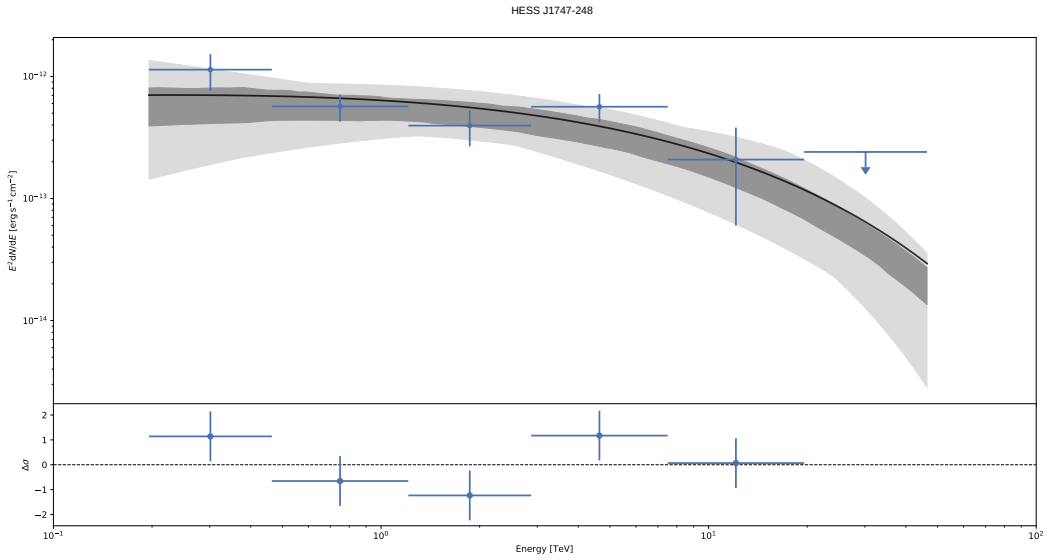
HESS J1747-248
E^2dN/dE [erg s^{-1} cm^{-2}]
$\Delta\sigma$
Energy [TeV]

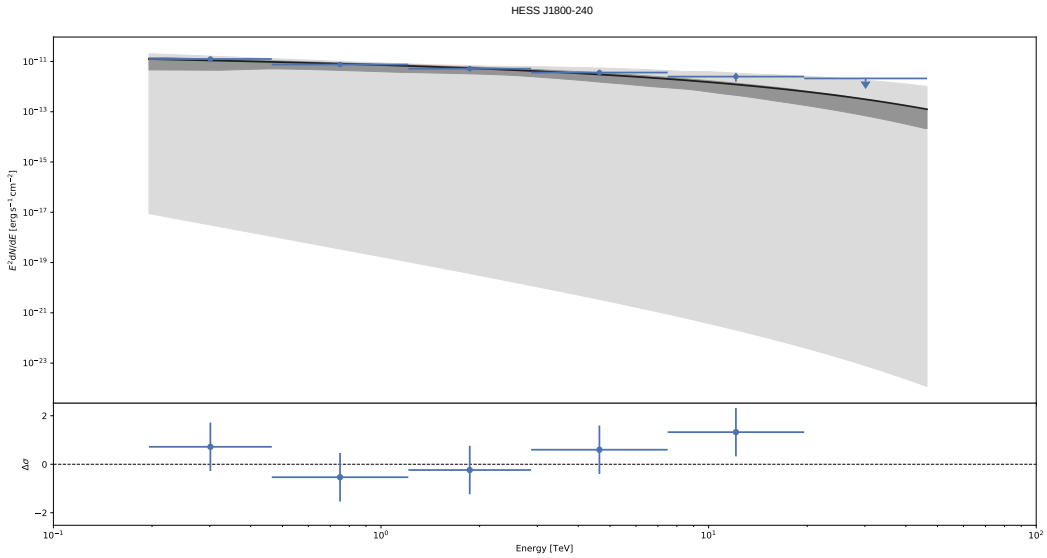
HESS J1800-240
E^2dN/dE [erg s^{-1} cm^{-2}]
$\Delta\sigma$
Energy [TeV]

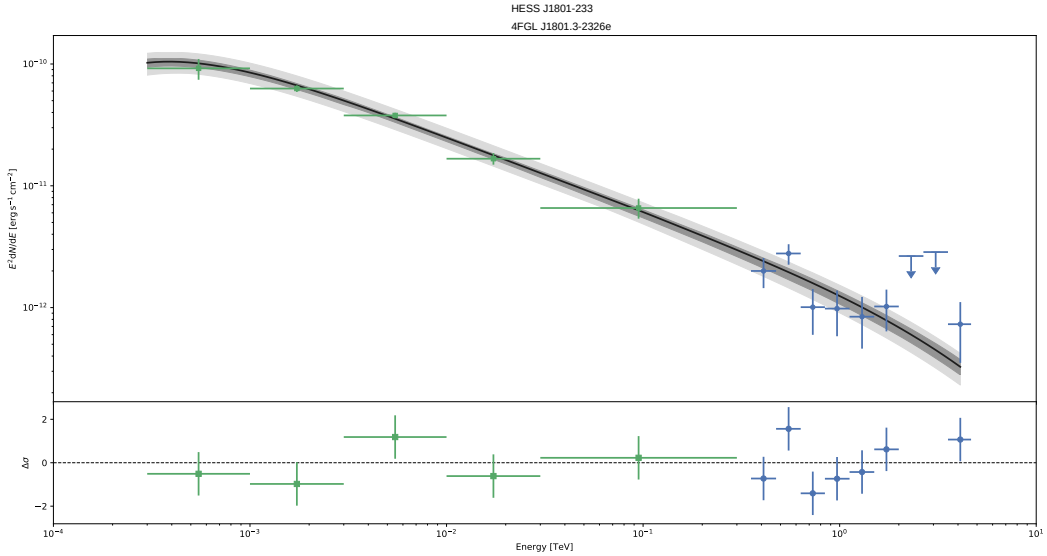
HESS J1801-233
4FGL J1801.3-2326e
E^2dN/dE [erg s^{-1} cm^{-2}]
$\Delta\sigma$
Energy [TeV]

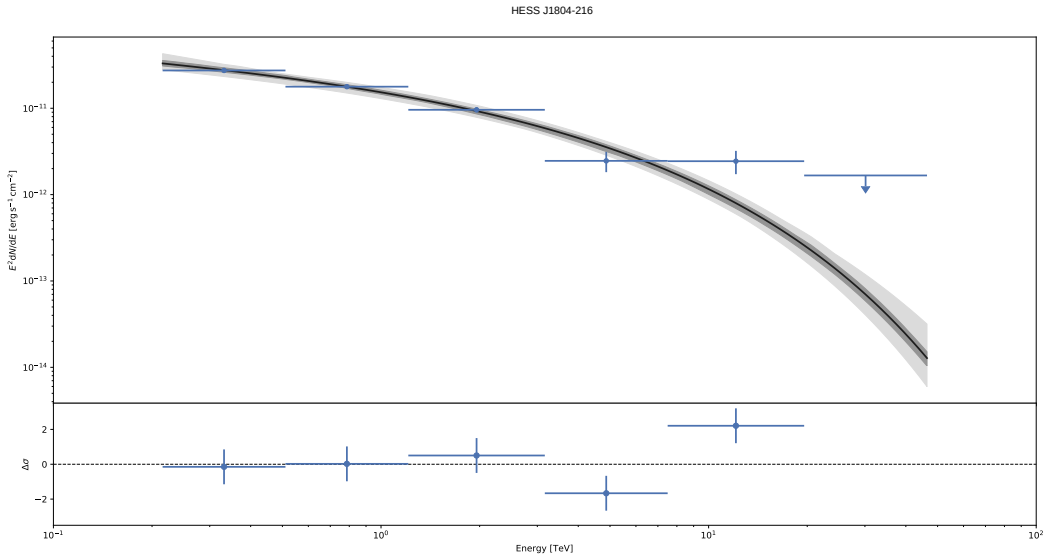
HESS J1804-216
E^2dN/dE [erg s^{-1} cm^{-2}]
$\Delta\sigma$
Energy [TeV]

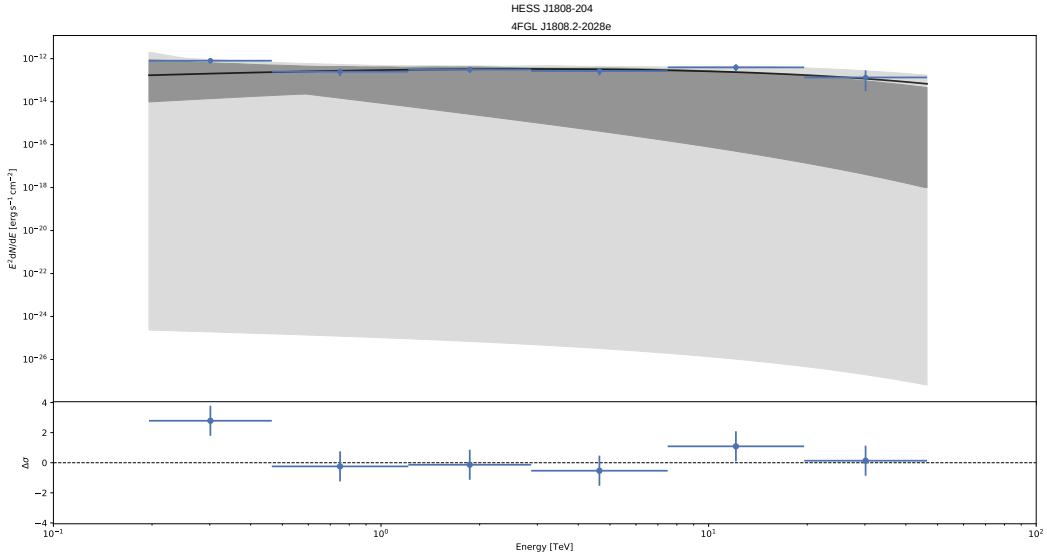
HESS J1808-204
4FGL J1808.2-2028e
E^2dN/dE [erg s^{-1} cm^{-2}]
$\Delta\sigma$
Energy [TeV]

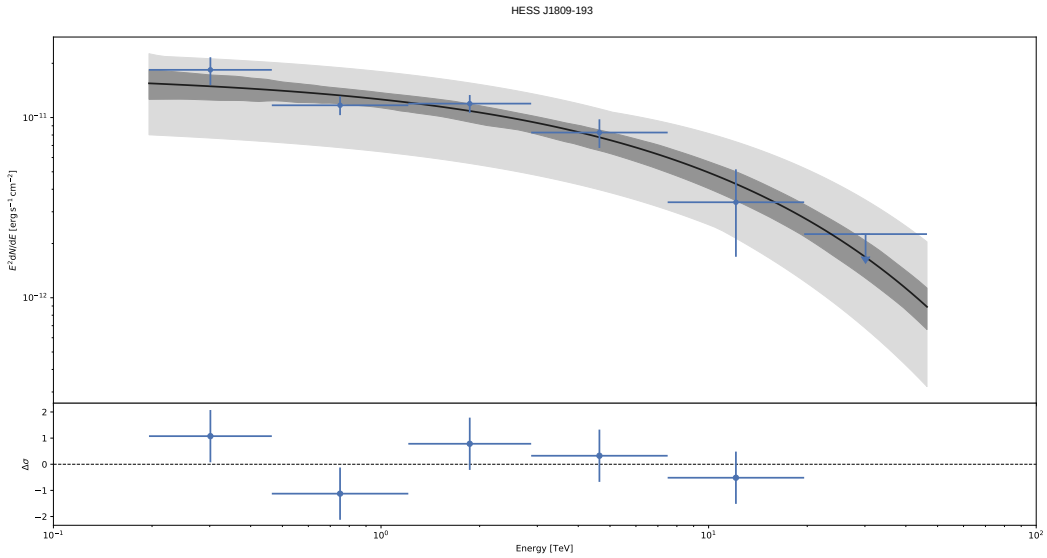
HESS J1809-193
E^2dN/dE [erg s^{-1} cm^{-2}]
10^{-11}
10^{-12}
$\Delta\sigma$
2
1
0
−1
−2
10^{-1}
10^{0}
10^{1}
10^{2}
Energy [TeV]

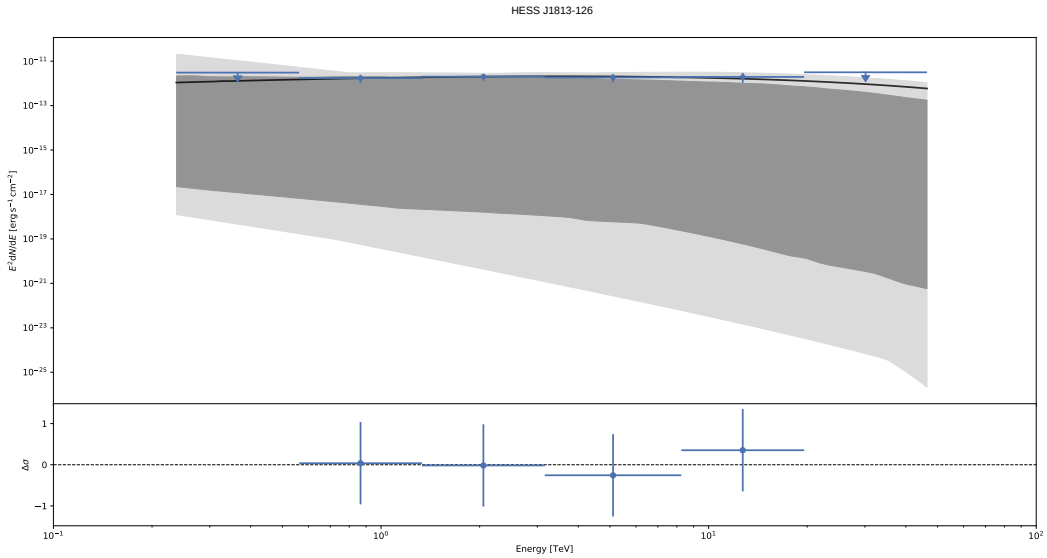
HESS J1813-126
E^2dN/dE [erg s^{-1} cm^{-2}]
10^{-11}
10^{-13}
10^{-15}
10^{-17}
10^{-19}
10^{-21}
10^{-23}
10^{-25}
$\Delta\sigma$
1
0
−1
10^{-1}
10^{0}
10^{1}
10^{2}
Energy [TeV]

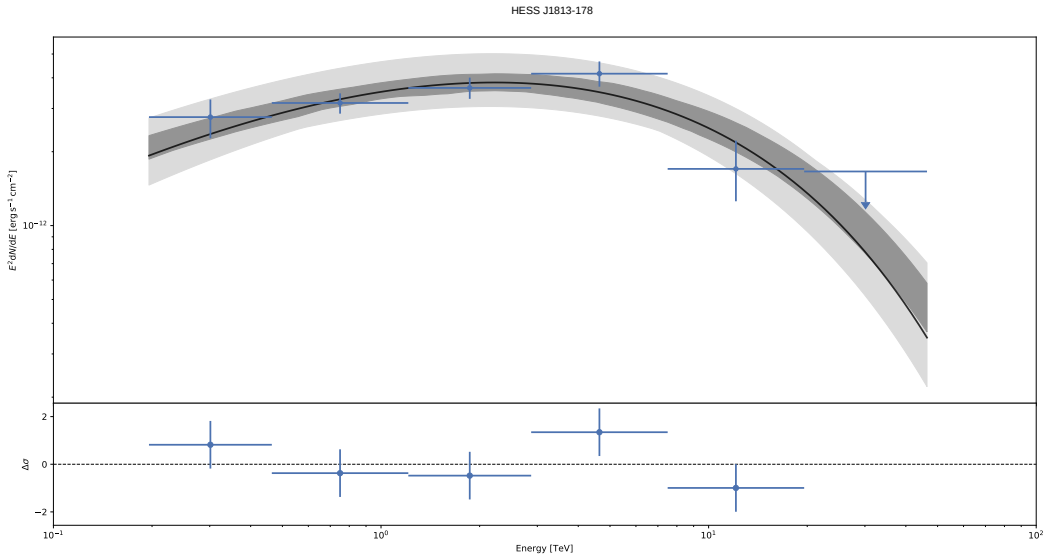
HESS J1813-178
E^2dN/dE [erg s^{-1} cm^{-2}]
10^{-12}
$\Delta\sigma$
2
0
−2
10^{-1}
10^{0}
10^{1}
10^{2}
Energy [TeV]

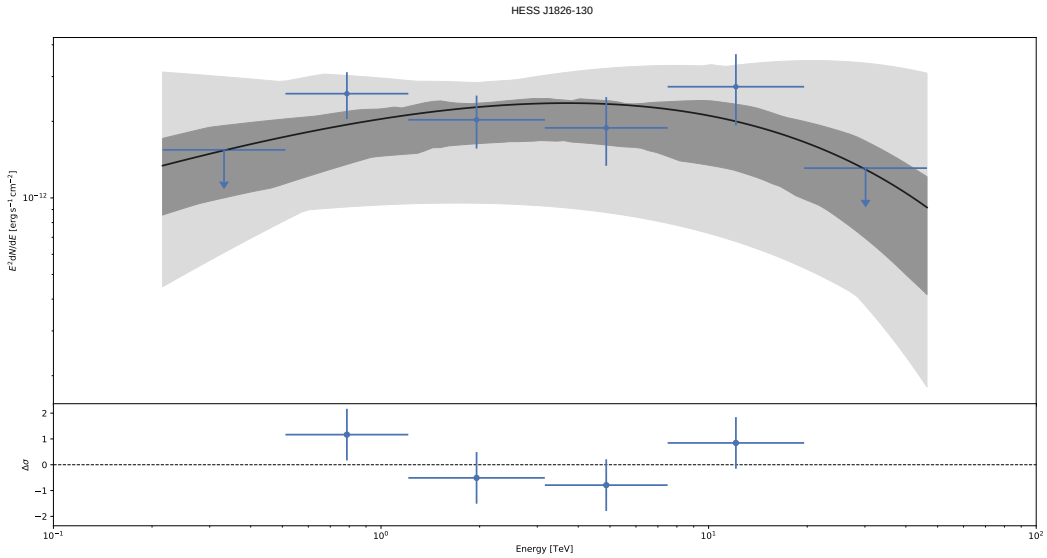
HESS J1826-130
E^2dN/dE [erg s^{-1} cm^{-2}]
10^{-12}
$\Delta\sigma$
2
1
0
−1
−2
10^{-1}
10^{0}
10^{1}
10^{2}
Energy [TeV]

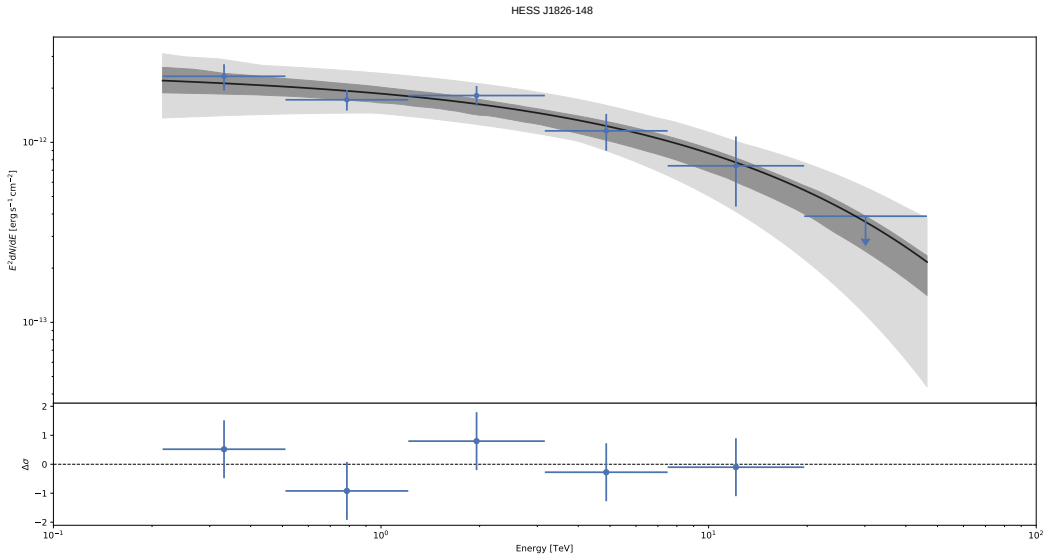
HESS J1826-148
$E^2 dN/dE$ [erg s^{-1} cm^{-2}]
10^{-12}
10^{-13}
$\Delta\sigma$
2
1
0
−1
−2
10^{-1}
10^{0}
10^{1}
10^{2}
Energy [TeV]

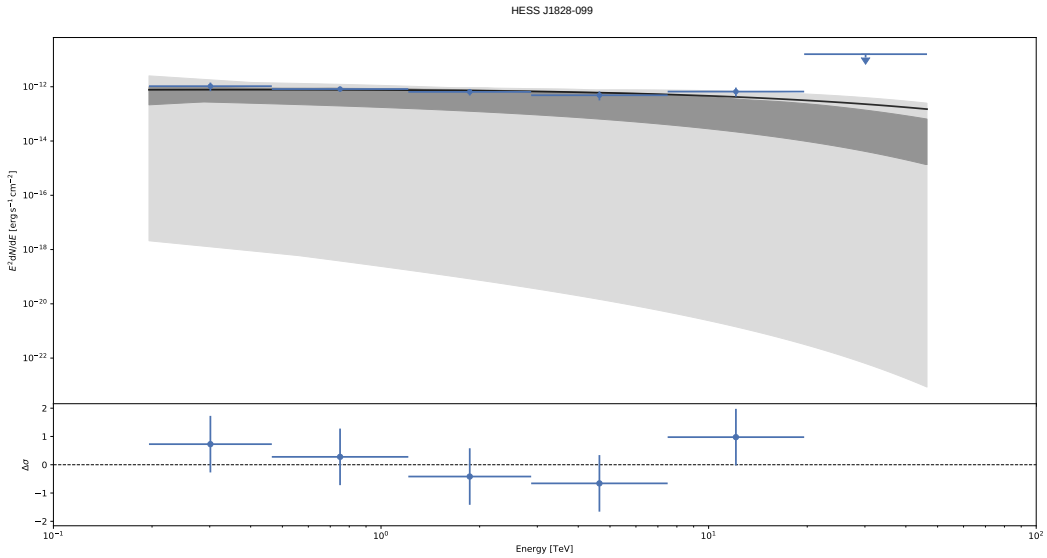
HESS J1828-099
$E^2 dN/dE$ [erg s^{-1} cm^{-2}]
10^{-12}
10^{-14}
10^{-16}
10^{-18}
10^{-20}
10^{-22}
$\Delta\sigma$
2
1
0
−1
−2
10^{-1}
10^{0}
10^{1}
10^{2}
Energy [TeV]

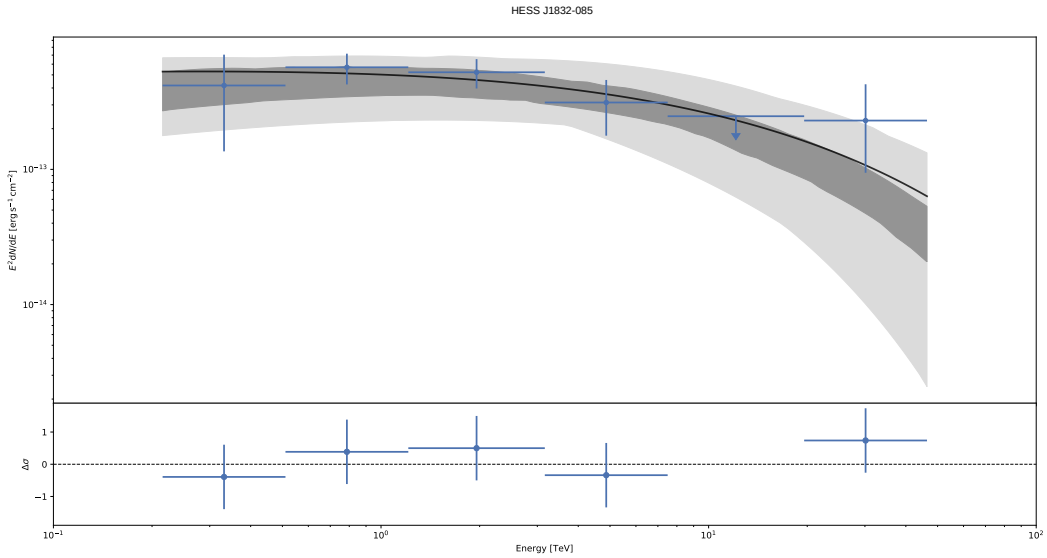
HESS J1832-085
E^2dN/dE [erg s^{-1} cm^{-2}]
10^{-13}
10^{-14}
$\Delta\sigma$
1
0
−1
10^{-1}
10^{0}
10^{1}
10^{2}
Energy [TeV]

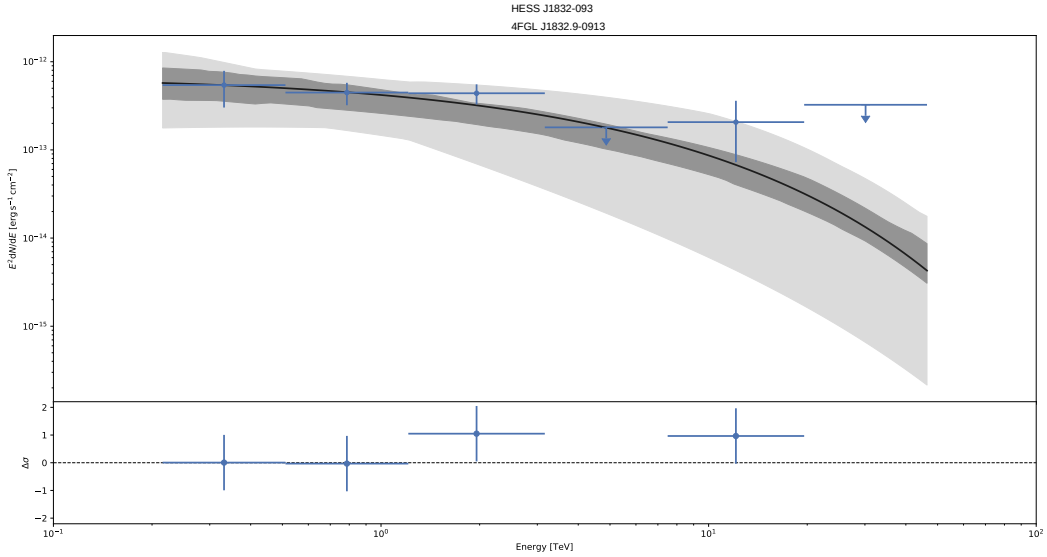
HESS J1832-093
4FGL J1832.9-0913
E^2dN/dE [erg s^{-1} cm^{-2}]
10^{-12}
10^{-13}
10^{-14}
10^{-15}
$\Delta\sigma$
2
1
0
−1
−2
10^{-1}
10^{0}
10^{1}
10^{2}
Energy [TeV]

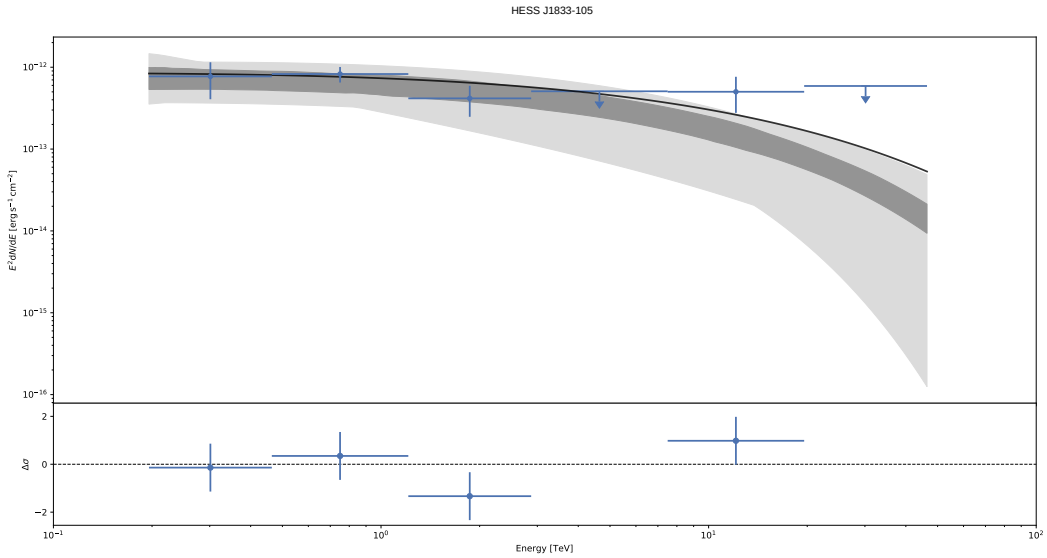
HESS J1833-105
E^2dN/dE [erg s^{-1} cm^{-2}]
$\Delta\sigma$
Energy [TeV]

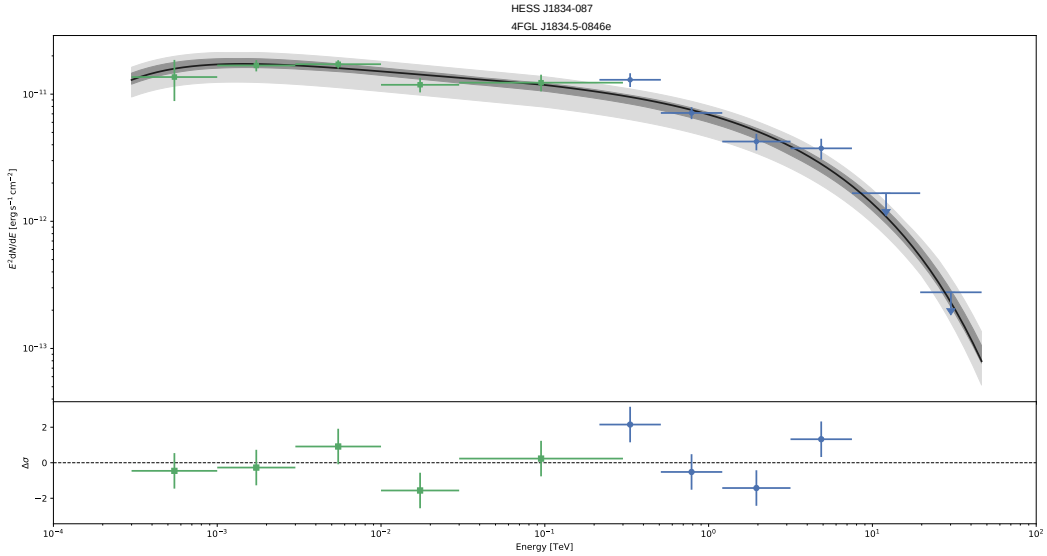
HESS J1834-087
4FGL J1834.5-0846e
E^2dN/dE [erg s^{-1} cm^{-2}]
$\Delta\sigma$
Energy [TeV]

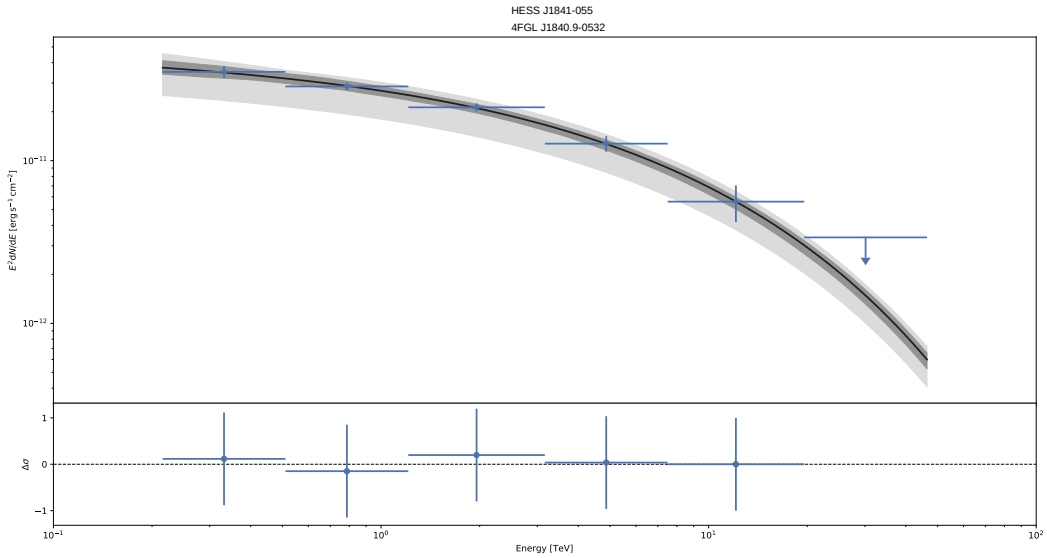
HESS J1841-055
4FGL J1840.9-0532
E^2dN/dE [erg s^{-1} cm^{-2}]
10^{-11}
10^{-12}
$\Delta\sigma$
1
0
−1
10^{-1}
10^{0}
10^{1}
10^{2}
Energy [TeV]

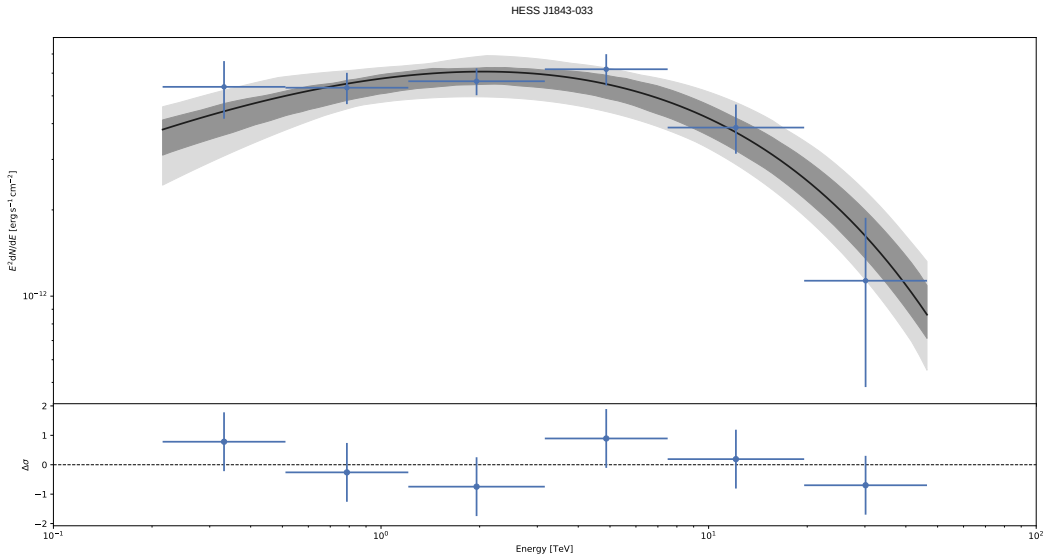
HESS J1843-033
E^2dN/dE [erg s^{-1} cm^{-2}]
10^{-12}
$\Delta\sigma$
2
1
0
−1
−2
10^{-1}
10^{0}
10^{1}
10^{2}
Energy [TeV]

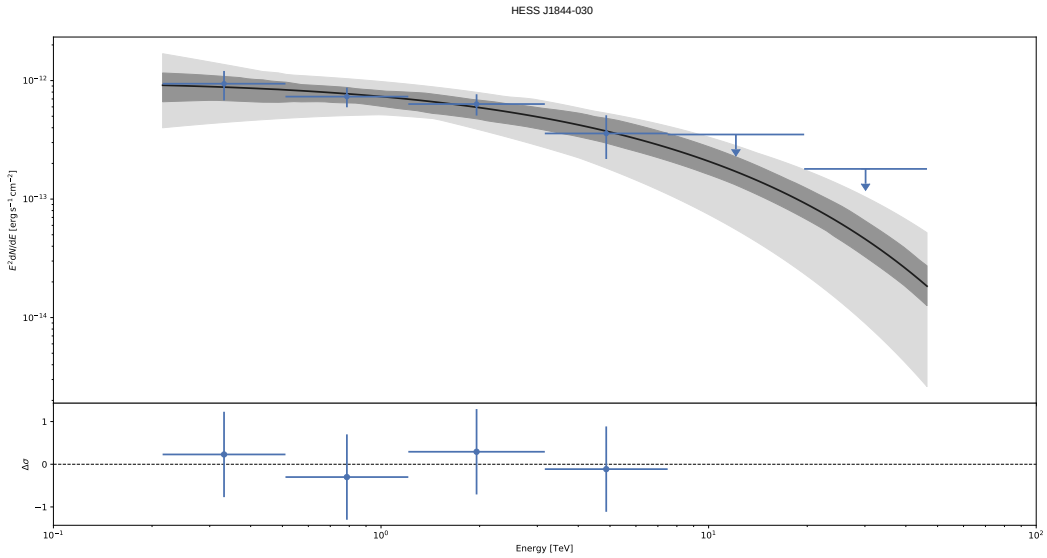
HESS J1844-030
$E^2 dN/dE$ [erg s^{-1} cm^{-2}]
10^{-12}
10^{-13}
10^{-14}
$\Delta\sigma$
1
0
−1
10^{-1}
10^{0}
10^{1}
10^{2}
Energy [TeV]

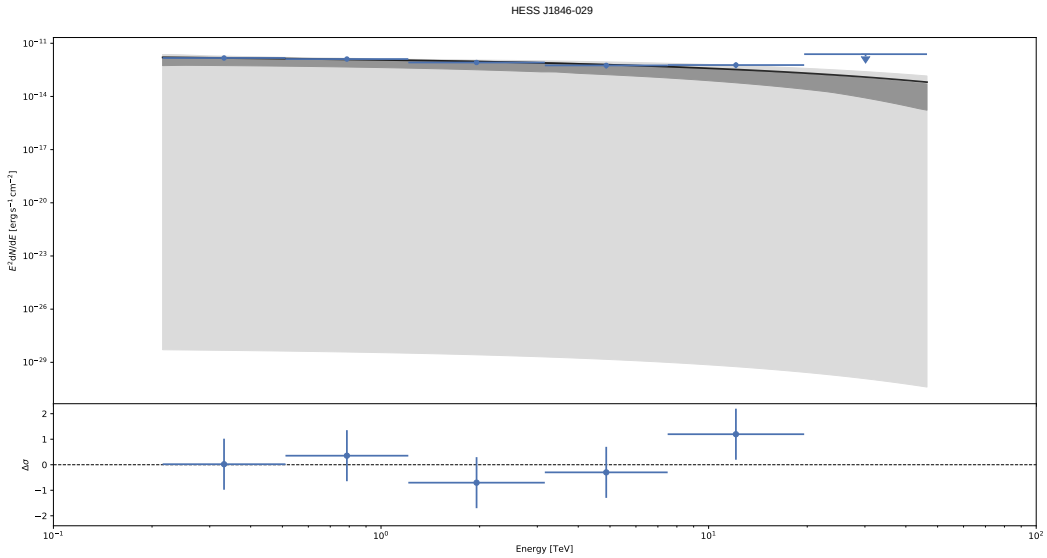
HESS J1846-029
$E^2 dN/dE$ [erg s^{-1} cm^{-2}]
10^{-11}
10^{-14}
10^{-17}
10^{-20}
10^{-23}
10^{-26}
10^{-29}
$\Delta\sigma$
2
1
0
−1
−2
10^{-1}
10^{0}
10^{1}
10^{2}
Energy [TeV]

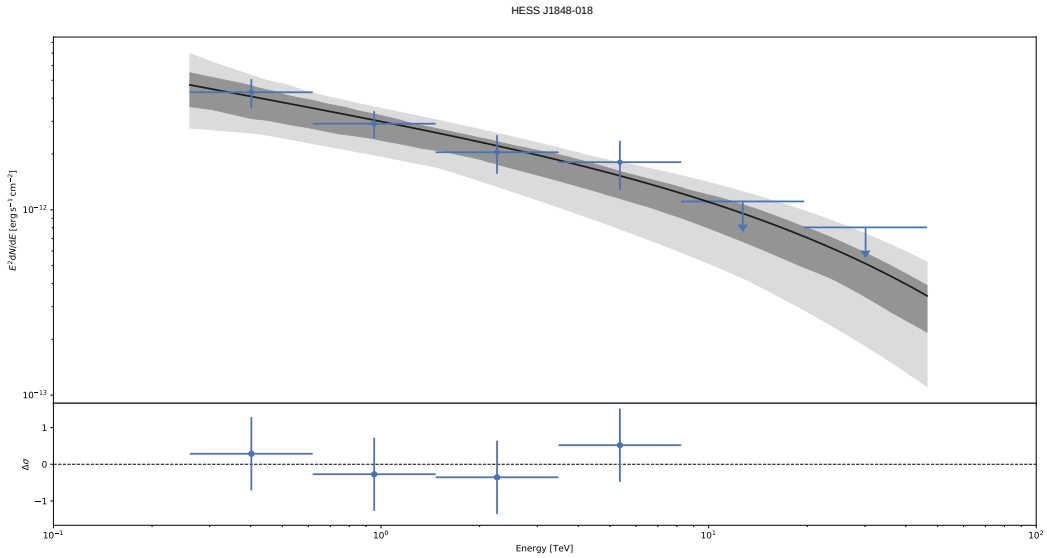
HESS J1848-018
$E^2 dN/dE$ [erg s^{-1} cm^{-2}]
10^{-12}
10^{-13}
$\Delta\sigma$
1
0
−1
10^{-1}
10^{0}
10^{1}
10^{2}
Energy [TeV]

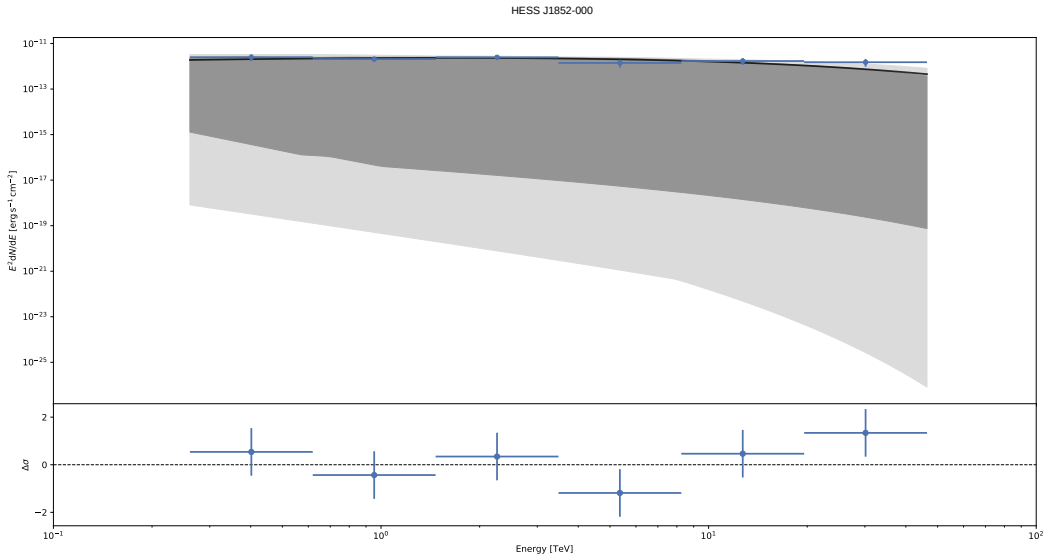
HESS J1852-000
$E^2 dN/dE$ [erg s^{-1} cm^{-2}]
10^{-11}
10^{-13}
10^{-15}
10^{-17}
10^{-19}
10^{-21}
10^{-23}
10^{-25}
$\Delta\sigma$
2
0
−2
10^{-1}
10^{0}
10^{1}
10^{2}
Energy [TeV]

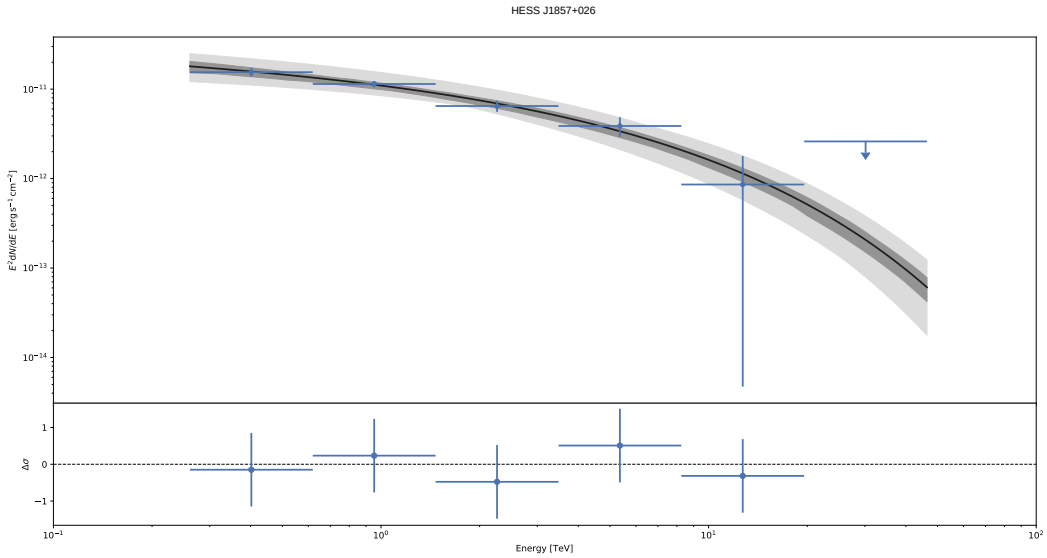
HESS J1857+026
E^2dN/dE [erg s^{-1} cm^{-2}]
10^{-11}
10^{-12}
10^{-13}
10^{-14}
$\Delta\sigma$
1
0
−1
10^{-1}
10^{0}
10^{1}
10^{2}
Energy [TeV]

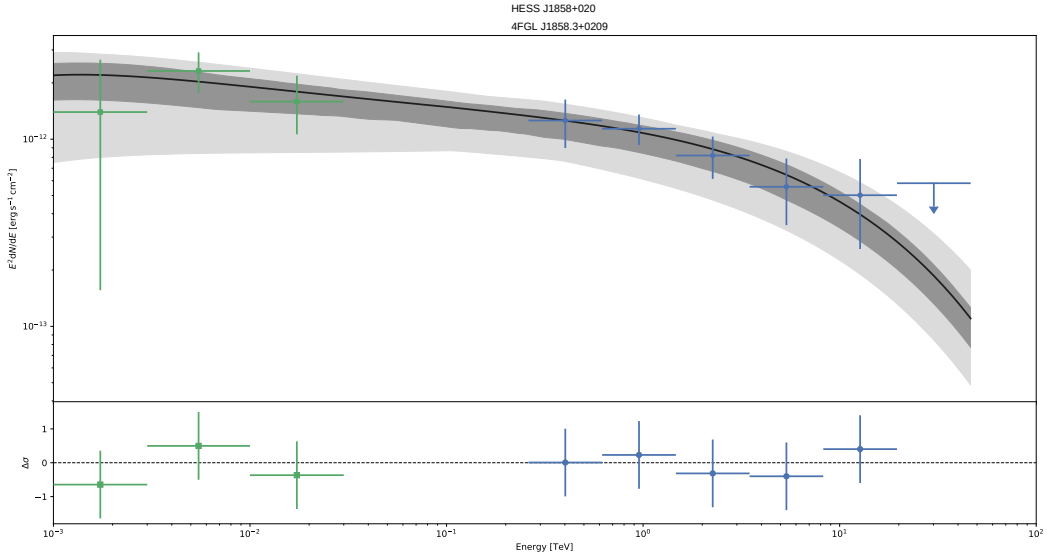
HESS J1858+020
4FGL J1858.3+0209
E^2dN/dE [erg s^{-1} cm^{-2}]
10^{-12}
10^{-13}
$\Delta\sigma$
1
0
−1
10^{-3}
10^{-2}
10^{-1}
10^{0}
10^{1}
10^{2}
Energy [TeV]

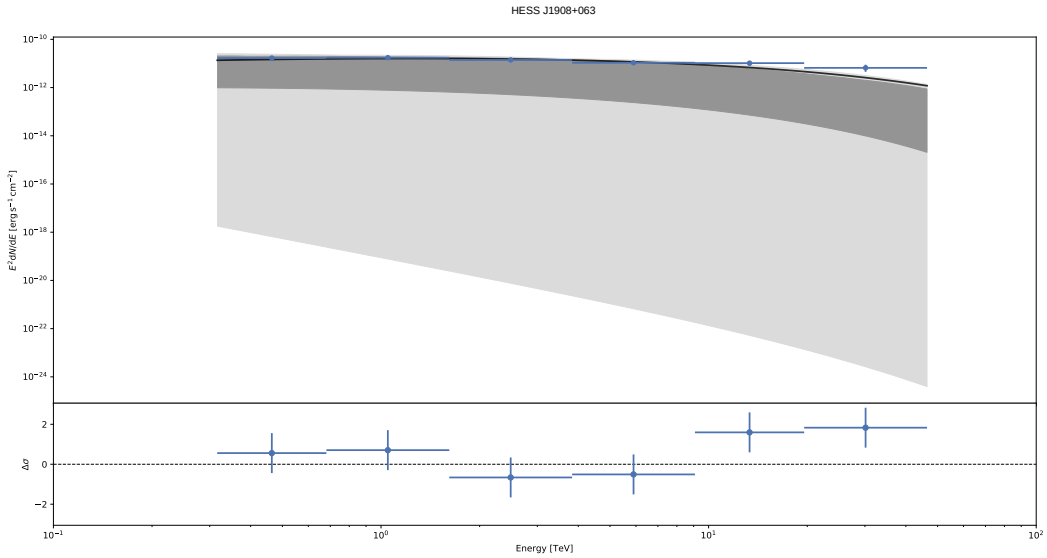
HESS J1908+063
E^2dN/dE [erg s^{-1} cm^{-2}]
$\Delta\sigma$
Energy [TeV]

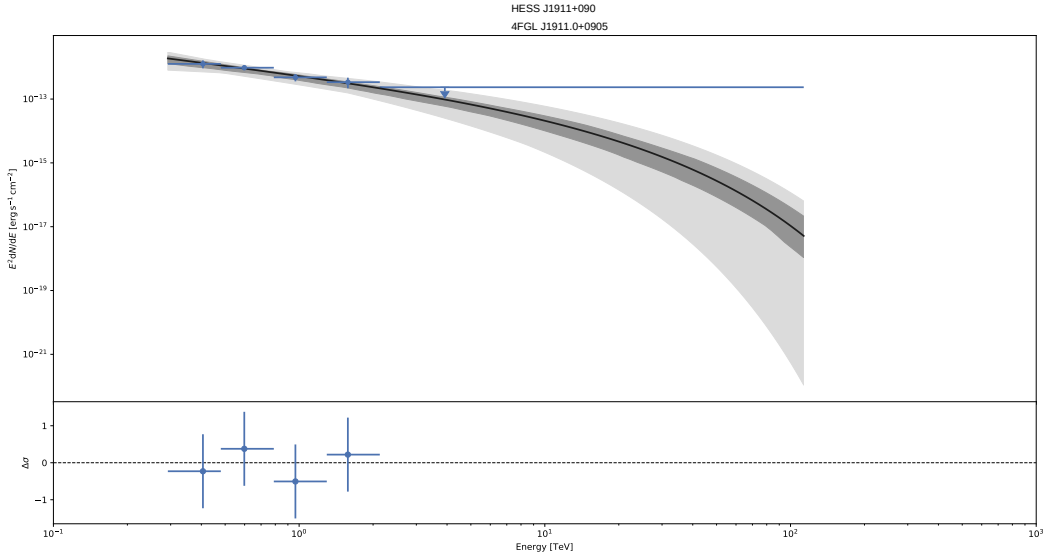
HESS J1911+090
4FGL J1911.0+0905
E^2dN/dE [erg s^{-1} cm^{-2}]
$\Delta\sigma$
Energy [TeV]

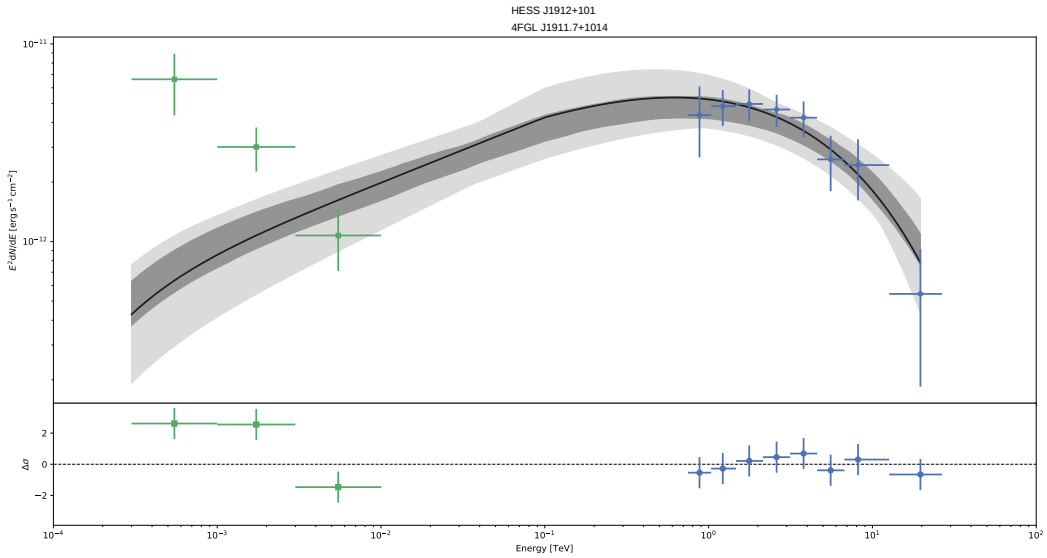
HESS J1912+101
4FGL J1911.7+1014
E^2dN/dE [erg s^{-1} cm^{-2}]
$\Delta\sigma$
Energy [TeV]

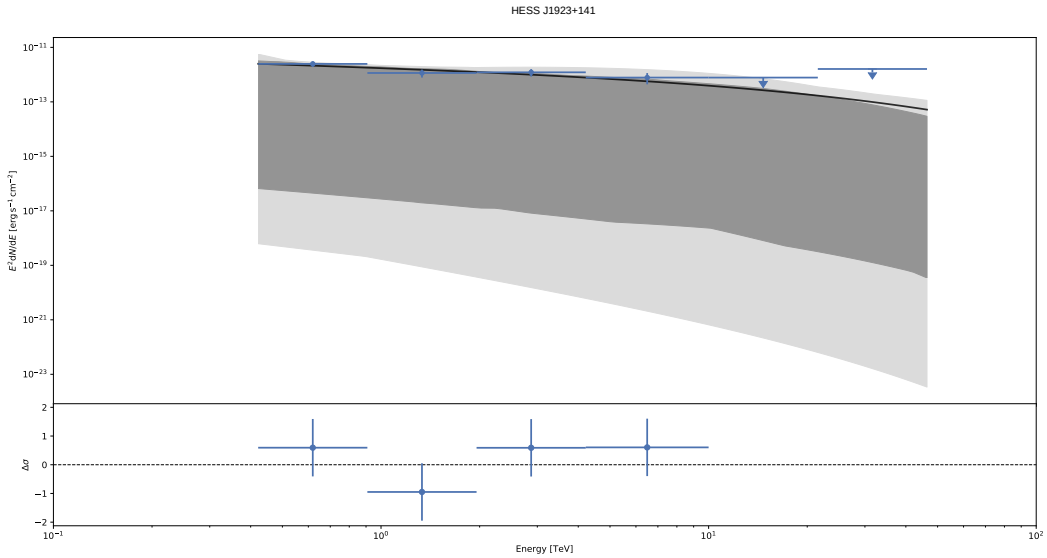
HESS J1923+141
E^2dN/dE [erg s^{-1} cm^{-2}]
$\Delta\sigma$
Energy [TeV]

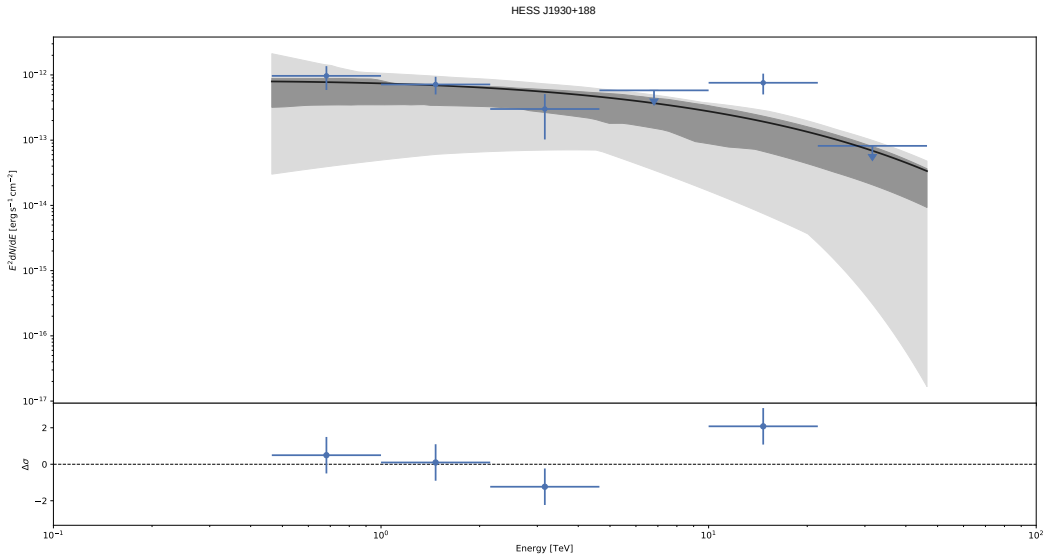
HESS J1930+188
E^2dN/dE [erg s^{-1} cm^{-2}]
$\Delta\sigma$
Energy [TeV]

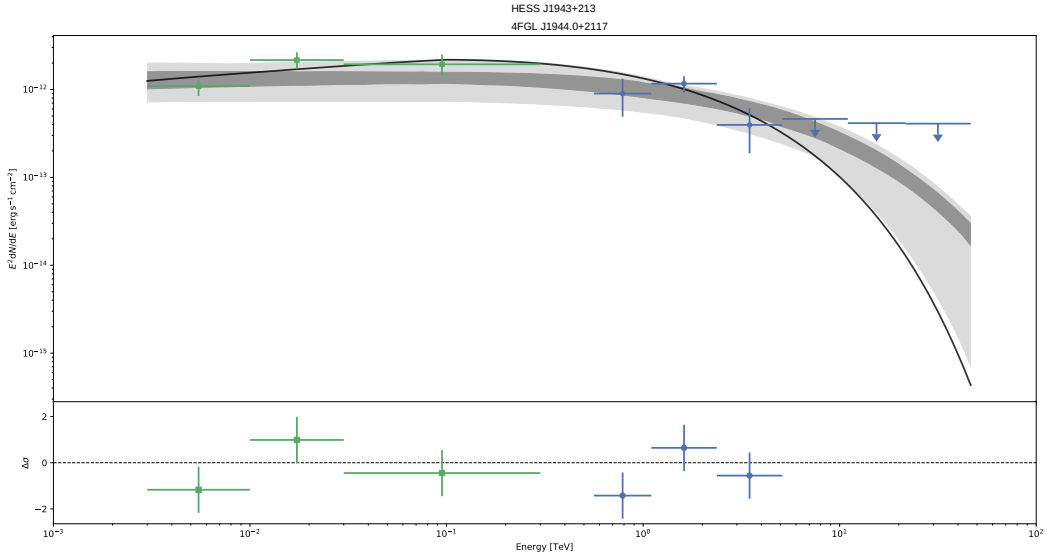
HESS J1943+213
4FGL J1944.0+2117
E^2dN/dE [erg s^{-1} cm^{-2}]
$\Delta\sigma$
Energy [TeV]

Appendix B: Kelner model python code

The Kelner model python code can be foud here: `https://github.com/RBatzofin/Kelner_model`

```
import astropy.constants as const
import astropy.units as u
import numpy as np
from scipy.integrate import quad

class Kelner_Model:
    r"""Secondary particle (pion mesons, gamma rays, electrons and neutrinos)
    emission from a proton population based on the work by Kelner et al.
    doi: 10.1103/PhysRevD.74.034018.
    URL https://link.aps.org/doi/10.1103/PhysRevD.74.034018

    Parameters
    ----------
    alpha : float
        The spectral index of the proton spectra

    beta : float
        The reference energy for normalisation

    E_0 : ‘~astropy.units.Quantity‘ float
        The cutoff energy of the proton spectra

    particle_type : str
        Select the secondary particle spectrum you want:
        gamma rays = ’gamma’
        electrons = ’electron’
        muonic neutrinos from direct decay = ’muon1’
        muonic neutrinos total spectrum = ’muon’
        for muonic neutrinos from the decay of the muon use ’electron’
        since these are approximately equal.

    nH : ‘~astropy.units.Quantity‘ float
        Number density of the target protons. Default is :math:‘1
        \mathrm{cm}^{-3}‘.

    amplitude : ‘~astropy.units.Quantity‘ float
```

```
    Give the normalisation of the model.
"""

def __init__(
    self,
    alpha = 2,
    beta = 1,
    E_0 = 1000*u.TeV,
    particle_type = 'muon' ,
    nH = 1.0*u.cm**-3,
    amplitude = None
    ):

    self.nH = nH
    self.beta = beta
    self.K_pi = 0.17
    self.m_p = (const.m_p*const.c**2).to(u.TeV)
    self.m_pi = 1.3497664e-4 *u.TeV
    self.alpha = alpha
    self.E0 = E_0
    self.A = self.get_A()
    self.amplitude = amplitude

    if particle_type == 'gamma':
        self.particle_function = self.F_gamma
    elif particle_type == 'electron':
        self.particle_function = self.F_electron
    elif particle_type == 'muon':
        self.particle_function = self.F_muon_neutrino
    elif particle_type == 'muon1':
        self.particle_function = self.F_muon_neutrino1

    self.nhat = (self.high_energy_spec(0.1*u.TeV)
                /self._low_energy_spec(0.1*u.TeV))

def F_gamma(self,x, Ep):
    """
    Total spectrum of gamma rays Kelner Eq. 58

    Parameters
    ----------
```

```
        x : float
            Energy of the gamma ray divided by energy of the proton

        Ep : float
            Incident proton energy

        Returns
        -------
        F_gamma : float
            Total spectrum of gamma rays.
        """
        L = np.log(Ep/u.TeV)
        B_gamma = 1.3 +0.14*L + 0.011*L**2
        beta_gamma = (1.79 +0.11*L + 0.008*L**2)**-1
        k_gamma = (0.801 +0.049*L + 0.014*L**2)**-1

        One = B_gamma * np.log(x) / x
        Two = (1-x**beta_gamma)/(1 + k_gamma*x**beta_gamma *(1-x**beta_gamma))

        Three = (
            1/np.log(x) - (4*beta_gamma*x**beta_gamma)/(1-x**beta_gamma)
            - (4 * k_gamma * beta_gamma * x**beta_gamma*(1-2*x**beta_gamma))
            /(1 + k_gamma*x**beta_gamma * (1-x**beta_gamma))
            )

        return One * Two**4 * Three

    def F_electron(self,x, Ep):
        """
        Total spectrum of electrons Kelner Eq. 62

        Parameters
        ----------
        x : float
            Energy of the electron divided by energy of the proton

        Ep : float
            Incident proton energy

        Returns
        -------
```

```
        F_electron : float
            Total spectrum of electrons.
        """
        L = np.log(Ep/u.TeV)
        Be = (69.5 + 2.65*L + 0.3*L**2)**-1
        beta_e = (0.201 +0.062*L + 0.00042*L**2)**-(1/4)
        k_e = (0.279 + 0.141*L + 0.0172*L**2)/(0.3 + (2.3+L)**2)

        numerator = 1 + k_e*(np.log(x))**2
        denominator = x*(1+ (0.3/x**beta_e))

        return Be * (numerator**3)/denominator *(-np.log(x))**5

    def F_muon_neutrino1(self,x,Ep):
        """
        Spectrum of muonic neutrinos from direct decay Kelner Eq. 66

        Parameters
        ----------
        x : float
            Energy of the muon divided by energy of the proton

        Ep : float
            Incident proton energy

        Returns
        -------
        F_muon_neutrino1 : float
            Spectrum of muonic neutrinos.
        """
        if x >= 0.427:
            return 0
        y = x/0.427
        L = np.log(Ep/u.TeV)
        B = 1.75 + 0.204*L + 0.01*L**2
        b = (1.67 + 0.111*L + 0.0038*L**2)**-1
        k = 1.07 - 0.086*L + 0.002*L**2

        One = B*(np.log(y)/y)
        Two = (1-y**b)/(1 + k*y**b *(1-y**b))
        Three = (
```

```
            1/np.log(y) - (4*b*y**b)/(1-y**b)
            - (4*k*b*y**b *(1-2*y**b))/(1+k*y**b *(1-y**b))
        )

        return One * Two**4 * Three

    def F_muon_neutrino(self,x,Ep):
        """
        Total spectrum of muonic neutrinos

        Parameters
        ----------
        x : float
            Energy of the muon divided by energy of the proton

        Ep : float
            Incident proton energy

        Returns
        -------
        F_muon_neutrino : float
            Total spectrum of muonic neutrinos.
        """
        return self.F_electron(x,Ep) + self.F_muon_neutrino1(x,Ep)


    def sigma_inel(self,Ep):
        """
        Inelastic cross-section for p-p interaction. Kelner eq 73

        Parameters
        ----------
        Ep : float
            Incident proton energy

        Returns
        -------
        sigma_inel : float
            Inelastic cross-section

        """
```

```
        try:
            L = np.log(Ep/u.TeV)
        except:
            Ep *= u.TeV
            L = np.log(Ep/u.TeV)
        E_th = 1.22 *10**-3 *u.TeV
        sigma_approx =  (34.3 +1.88*L + 0.25*L**2)
        factor = 1-(E_th/Ep)**4

        if Ep <= E_th:
            factor = 0.0

        return sigma_approx * factor**2 *10**-27 *u.cm**2

    def get_A(self):
        """
        Constant determined from the condition in Kelner eq 80
        """
        integration = quad(lambda Ep: Ep/(Ep**self.alpha)
        * np.exp(-((Ep*u.TeV)/self.E0)**self.beta),
        1, np.inf, epsabs=0)

        A = (1*u.erg *u.cm**-3)/(integration[0])

        return A.to(u.TeV /u.cm**3)

    def Jp(self,E):
        """
        Particle distribution Kelner eq 74

        Parameters
        ----------
        E : Incident proton energy

        Returns
        -------
        Jp : float
            Particle distribution
        """
        return (self.A/(E**self.alpha))*np.exp(-(E/self.E0)**self.beta)
```

```
def int_for_high_energy(self,x,E):
    """
    Function to integrate in Kelner eq 71
    """
    try:

        return (self.sigma_inel(E/x)*self.Jp(E/x)
        *self.particle_function(x,E/x)/x).value
    except:

        E *= u.TeV

        return (self.sigma_inel(E/x)*self.Jp(E/x)
        *self.particle_function(x,E/x)/x).value

def high_energy_spec(self, E):
    """
    Spectrum for energies > 0.1 TeV
    """
    spec =  quad(self.int_for_high_energy
    ,0.0,1.0,args=E,epsrel = 10**-13, epsabs=0)
    return const.c.cgs.value*spec[0] *u.cm**-3 /u.s /u.TeV


def int_for_delta(self,E):
    """
    Function to integrate in Kelner eq 78
    """
    E *= u.TeV
    if E.unit != u.TeV:
        E /= u.TeV
    q_pi = ((const.c * self.nH /self.K_pi)
        *self.sigma_inel(self.m_p+E/self.K_pi)
        *self.Jp(self.m_p+E/self.K_pi))

    return ((q_pi/(np.sqrt(E**2 - self.m_pi**2)))
    .to(u.cm**-3 *u.TeV**-self.alpha /u.s)).value

def _low_energy_spec(self,E):
    E_min = E + (self.m_pi**2)/(4*E)
```

```
        spec = quad(self.int_for_delta,E_min.value,np.inf, epsrel = 1e-13, epsab
        return 2*spec[0] *u.cm**-3 /u.TeV /u.s

    def low_energy_spec(self,E):
        """
        Spectrum for energies < 0.1 TeV
        """
        return self.nhat*self._low_energy_spec(E)

    def energy_spec_function(self, E):
        """
        Energy spectrum from p-p interactions
        Parameters
        ----------
        E : `~astropy.units.qunatity` float or array
        Energy range to calculate the spectrum

        Returns
        -------
        energy_spec_function : `~astropy.units.quantity` float or array
        """
        flux = []
        unit = u.TeV**-1 /u.s /u.cm**3
        try:
            for e in E:
                if e >= 0.1*u.TeV:
                    _flux = self.high_energy_spec(e)
                elif e < 0.1*u.TeV:
                    _flux = self.low_energy_spec(e)
                if self.amplitude:
                    unit = u.TeV**-1 /u.s /u.cm**2
                    _flux = (_flux/(4*np.pi*u.kpc**2)
                            /self.A *self.amplitude.value
                            *u.TeV *u.TeV/u.erg)

                    _flux = _flux.to(u.TeV**-1 /u.s /u.cm**2)
                flux.append(_flux.value)
        except:
            if E >= 0.1*u.TeV:
                _flux = self.high_energy_spec(E)
            elif E < 0.1*u.TeV:
```

```
            _flux = self.low_energy_spec(E)
        if self.amplitude:
            unit = u.TeV**-1 /u.s /u.cm**2
            _flux = (_flux/(4*np.pi*u.kpc**2)
                    /self.A *self.amplitude.value
                    *u.TeV *u.TeV/u.erg)

            _flux = _flux.to(u.TeV**-1 /u.s /u.cm**2)
        flux = _flux.value


    return flux * unit
```